Bismuth and Germanium Nanoscale Cluster Devices

A thesis submitted in partial fulfilment of the
requirement for the Degree of

Doctor of Philosophy in Physics

at the
University of Canterbury

by

David Mackenzie

Department of Physics and Astronomy

2010

Abstract

Transistors are the fundamental components of computer processors. The dimensions of transistors used in microprocessors are decreasing every year and the challenge of maintaining this trend now requires nanoscale dimensions. A potential method of achieving nanoscale dimensions is using atomic clusters as building blocks. It is therefore desirable to investigate transistor-like behaviour in cluster devices.

Traditionally, transistor devices are made from semiconducting materials. It was therefore proposed that gated behaviour would be observable in devices that are fabricated from germanium clusters. A germanium cluster source was designed and built. Field effects were successfully observed in films of germanium clusters. Immediately after deposition, the gate effect of germanium cluster films was insignificant. As the films slowly oxidized in vacuum, a decrease in the overall carrier concentration was observed which lead to an increase in the gate effect, with a maximum change in resistance observed of 12%.

When films of germanium clusters were exposed to air, a resistance decrease was observed, attributed to water vapour adsorbing on the surface. The phenomenon was further investigated and the proposed resistance change mechanism involves water vapour creating surface defects which act as donors and cause the electron concentration in the film to increase.

Films of germanium clusters were sensitive to hydrogen concentrations above 1% in air, with up to a factor of 25 decrease in resistance observed at room temperature for 5% hydrogen concentration. Thin films were found to be most sensitive. The higher sensitivity was attributed to the larger surface-to-volume ratio. The proposed mechanism for sensing is that defects are created on the surface of the film, which in turn act as donors which cause the electron concentration in the film to increase.

Bismuth is a semimetal and gate effects have previously been observed in bismuth nanowires. Parallel bismuth nanowires of 300 nm diameter were successfully deposited at a distance of 200 nm apart allowing one of the wires to be used as a gate. The gate effects observed in bismuth cluster structures were weak and inconclusive, with a small gate effect (change in resistance of 0.1%) observed at 11 K in some devices.

Contents

List of Figures

List of Tables

Chapter 1

Introduction

Traditionally, the physical sciences have been concerned with distinct studies of atoms/molecules and bulk crystals. On both bulk and atomic scales, the properties of many materials are comprehensively researched and well understood. Although bulk material is made up of the same type of individual atoms that are studied in atomic science, the bulk and atoms have different properties. As the size of the materials decreases from the bulk, there must be some transition which occurs such that the properties eventually match those of the atomic scale. The intermediate size range where properties change, usually takes place when the material concerned is of order nanometres in size. The investigation of these intermediate properties of matter between atomic and bulk is nanoscience. And the application of this nanoscience is nanotechnology.

The concept of nanotechnology was first suggested in 1959 by Richard Feynman [1], but it has only been seriously studied in the last fifteen years. However, low-dimensional systems (such as ultra-thin films and nanosized particles) have been studied since the early 1900s. Advancements in vacuum and microscope technology,

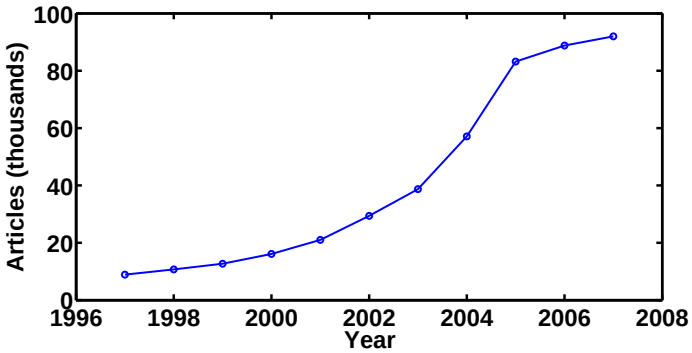

Figure 1.1: Number of publications per year with nano* in article title, from *Google Scholar*.

as well as small-scale manipulation and computer simulations have resulted in the steady increase in the output of nanotechnology papers. This is demonstrated by Figure 1.1 which shows the recent increase in publications with a nanotechnology related title.

The endeavour of nanotechnology is the rapid and precise large-scale manipulation of atoms. If this goal is realized, the potential applications are almost endless. The ultimate template for nanotechnology is a biological system, such as an organism, a cell or even an organelle. Biological processes select raw materials and accurately self-assemble them on a near atomic-scale with remarkable precision. These systems have been naturally selected for over billions of years and it is the challenge of the nanotechnologist to intelligently design processing techniques which too can select, assemble and exploit atoms and molecules for a practical purpose.

One of the major investors in nanotechnology research is the microprocessor industry. The challenge of maintaining Moore's Law [3] now requires the gate length of field effect transistors to be nanoscale. A potential method of achieving nanoscale dimensions for transistors is to use atomic clusters as building blocks. This method provides motivation for one of the goals of this thesis: to make cluster-assembled Field Effect Transistors.

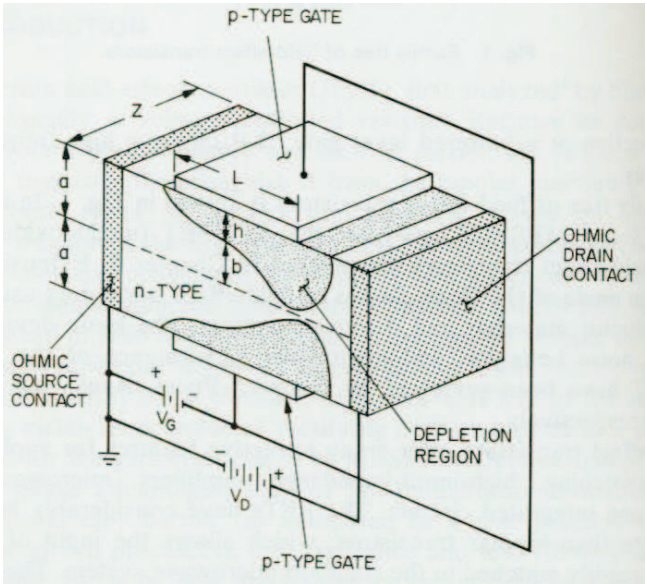

Figure 1.2: Basic form of a field effect transistor. A voltage applied to the gates creates an electric field which increases or decreases the size of the depletion zones and hence affects the conductance of the channel [2].

1.1 Field Effect Transistors

The origins of the Field-Effect Transistor (FET) were in the 1950s [4] and today they are the fundamental components of computer processors [5]. All FETs work via the same principle, which is now described.

FETs have four common components: the source and drain, gate, and channel, which are all shown in Figure 1.2. The channel is a current path with switchable conductance; it can be turned *on* or *off* by the gate. The source and drain provide the electrical contacts to the *source-drain voltage* which contributes electrons to flow in the channel. The gate controls the conductance of the device by applying a voltage to create or eliminate charge carriers in the channel. The source-drain current is the part of the signal to be amplified (or be decreased by) the gate voltage. By controlling whether the transistor is on or off, a FET can be used as a binary 1 or 0 in a microprocessor or electronic memory. FETs are defined as off when the source-drain current is very low. There are four major types of FETs. Channels can be n-type or p-type, and furthermore, the channel can work in two modes (enhancement or depletion). The four options are now described.

In the absence of a gate bias, the channel conductance can be either high or low; these are depletion FETs or enhancement FETs respectively. For FETs which run in depletion mode, the charge carriers in the channel must be depleted by the gate bias in order to switch the device off. If the channel is p-type, a positive gate bias can eliminate holes in the channel because the positive voltage depletes holes away from the semiconducting channel. Conversely, if the channel is n-type, a negative gate bias eliminates electrons in the channel because the negative voltage depletes electrons from the channel.

If FETs run in enhancement mode, the gate bias increases channel conductance. If the channel is p-type, a negative gate bias will enhance holes in the channel because the negative voltage attracts holes from the substrate. Conversely, if the channel is n-type, a positive gate bias will enhance electrons in the channel because the positive voltage attracts electrons from the substrate. Additional details of FETs are described elsewhere [2].

1.2 Atomic Clusters

The research in this thesis explores the properties of nanosized particles known as atomic clusters and throughout this text these will be referred to as *clusters*. Clusters are aggregates of atoms (or molecules) sized between individual atoms and crystals large enough to be considered bulk matter [9]. They are bound together

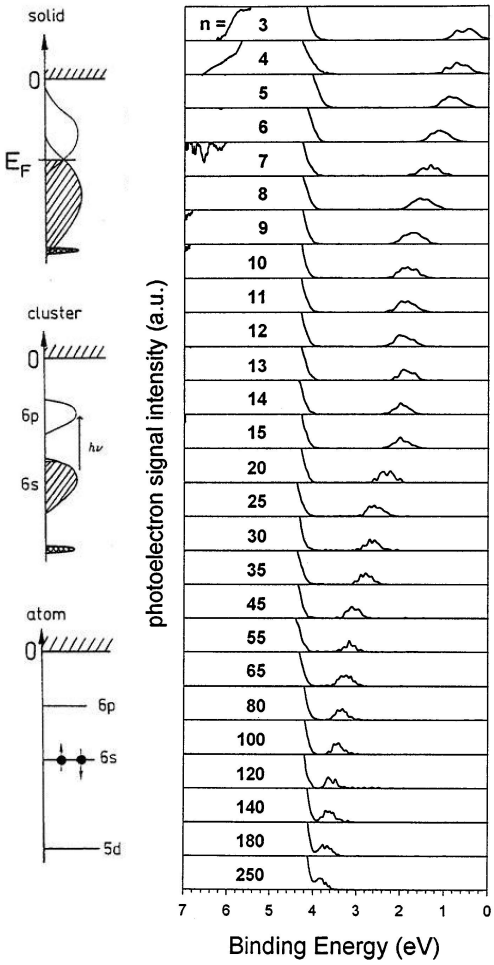

Figure 1.3: Left: Electronic structure of mercury bulk, cluster and atom showing transition to metallic behaviour [6]. Right: Photoelectron spectra of small mercury clusters showing the increase in bandgap for smaller clusters [7].

Number of atoms in cluster	Bandgap
3	3.43 eV
55	1.02 eV
80	0.72 eV
250	0.19 eV

Table 1.1: The variation of bandgap with size for selected mercury clusters [7].

by the same forces as molecules: that may be hydrogen, inter-molecular, metallic or covalent bonds. Clusters range from 2 - 10^{10} atoms with a maximum size of ∼100 nm. Because the nanometre size-range of clusters corresponds to the size range between the atomic and bulk, size dependent effects are expected.

An example of a size effect in clusters is variation in bandgap, and this has been demonstrated by mercury clusters. Mercury clusters that have a small number of atoms (up to 250) had their bandgaps determined by photoelectron spectroscopy [7]. As the number of atoms in each cluster is decreased, a bandgap appears, shown in Figure 1.3. The variation of bandgap with size for selected clusters is shown in Table 1.1. For 3 atom clusters, mercury is a wide-bandgap semiconductor whereas clusters with 250 atoms are near-metallic. Mercury clusters with 55 and 80 atoms have bandgaps corresponding to silicon and germanium respectively.

Another size-dependent effect is that the melting point of clusters can be a function of their size. This is documented for tin clusters [8], gold clusters and silver clusters [12] amongst others. The melting point of tin clusters as a function of size is shown in Figure 1.4. The melting point decreases with cluster radius with approximately a r^{-1} dependence.

When clusters are formed, there are certain sizes which are intrinsically more stable. These so-called magic numbers reflect higher stability of the geometrical

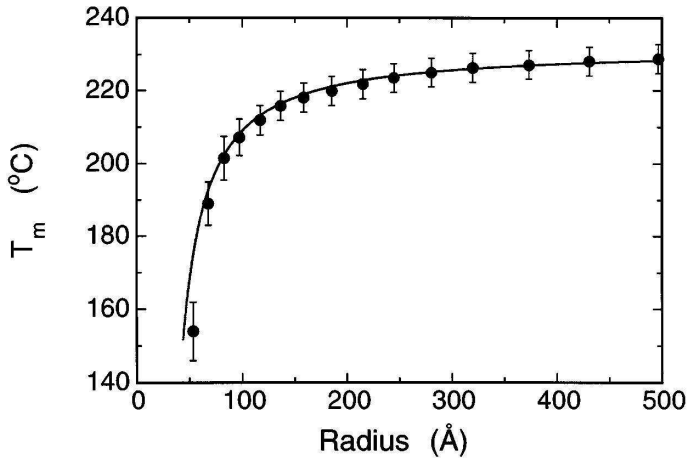

Figure 1.4: Size dependant melting points of tin particles [8].

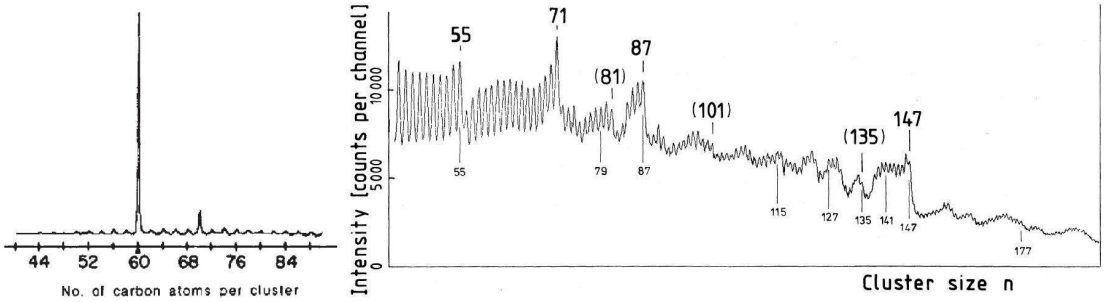

Figure 1.5: Mass spectra of clusters. Left: Clusters of carbon showing largest abundance of C_{60} [10]. Right: Clusters of xenon, magic numbers are shown in bold [11].

configuration of the stable clusters. This is demonstrated for both carbon [10] and xenon [11] clusters in Figure 1.5.

In order for clusters to be used in devices, or as device components, they must be deposited onto a substrate.

1.2.1 Clusters on Surfaces

Clusters on surfaces have also been comprehensively studied. When a cluster is deposited onto a surface [14] it can either become bound to the specific landing location, diffuse on the surface, aggregate with other clusters, or become desorbed.

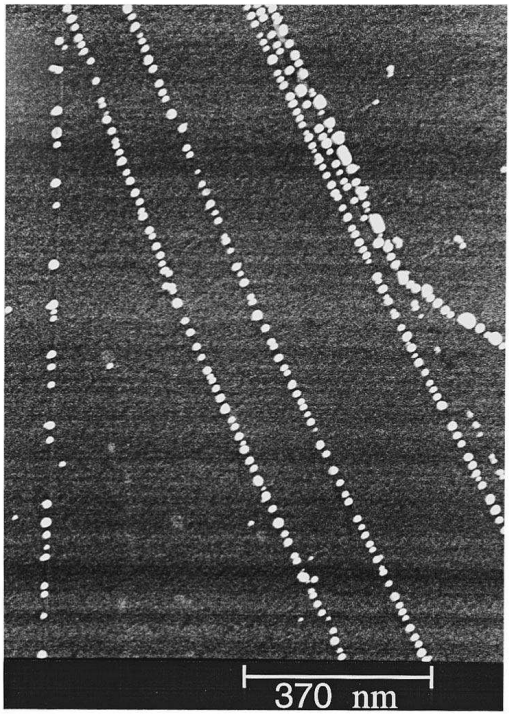

Figure 1.6: Silver clusters aligned at step edges deposited on HOPG [13].

The factors which determine surface behaviour are the material of the cluster, its properties (size, temperature, speed, etc.), and the type and temperature of substrate.

Different substrates have been studied to determine their influence on cluster-film morphology [15, 16]. The diffusion and aggregation of clusters has been studied on highly-ordered pyrolytic graphite (HOPG). HOPG is a smooth graphite surface with natural steps. Due to the weak binding of gold clusters to HOPG, they can be moved with an AFM tip [17]. This method can be used to create any two-dimensional structure of clusters. However, it is not practical for large-scale circuits, as this method is extremely time consuming, requiring assembly of individual clusters. It is more desirable to use a method where clusters are patterned without individual-particle manipulation.

When silver clusters are deposited on HOPG, they diffuse on the surface before aggregating at a step, shown in Figure 1.6 [13]. These chain-like structures resemble nanowires and require no manipulation of clusters. These experiments show the possibility for atomic clusters to be the building blocks of nanodevices, which is the central research theme of the cluster group at Canterbury.

1.3 Previous and Current Canterbury Cluster Research

The cluster group at the University of Canterbury has researched the properties of clusters for a decade. Initial experiments were performed using a high-vacuum (HV) system. The research studied the crystal structure of unsupported clusters and thin films on substrates. Subsequent experiments use a ultra-high-vacuum (UHV) system which has an interchangeable inert-gas-aggregation/sputtering cluster source. The following subsections review the experimental results.

1.3.1 Percolating Films of Clusters

This subsection explains how percolation theory can be applied to cluster films and describes the results of thin films made with the HV and UHV system. When clusters are deposited between electrical contacts on a substrate, there are two possible states for the conductance of the system: clusters can either provide a continuous electrical path between contacts connecting them, or can be part of a non-continuous network. The transition between these two states occurs at the *percolation threshold*, defined as the minimum coverage where a continuous network of clusters is formed. Only

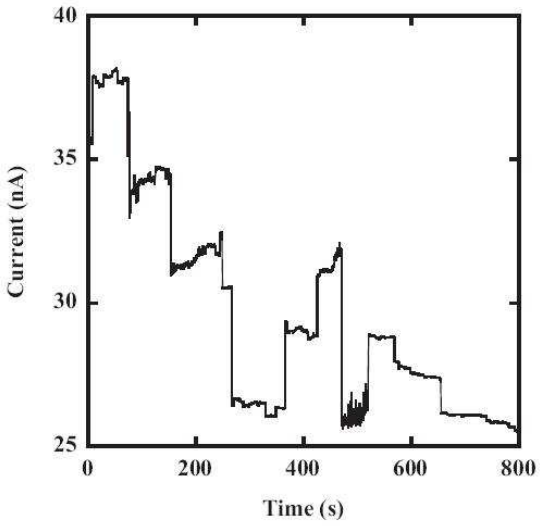

Figure 1.7: Current versus time for a bismuth cluster film produced in the HV system [18].

when the threshold is reached can an onset of conduction be measured. Further explanations of percolation theory can be found in detail elsewhere [19, 20].

The following paragraph describes the main results from the HV system using various substrate types. Percolating films of clusters have been used to make cluster-based devices. Electrical conductivity during the onset of conduction of bismuth, antimony and silver cluster films have been studied using the HV system [22]. Bismuth clusters were deposited onto either HOPG or silicon substrates. The ∼20 nm clusters showed considerable coalescence once deposited on HOPG, an effect not observed on the silicon substrates. The electrical behaviour of the bismuth films typically showed oxidative and stepping resistive effects. An I(t) curve is shown in Figure 1.7.

Problems with the HV system, including cluster-beam inhomogeneity and the relatively poor vacuum, lead to inconsistent sample deposition and oxidation. These

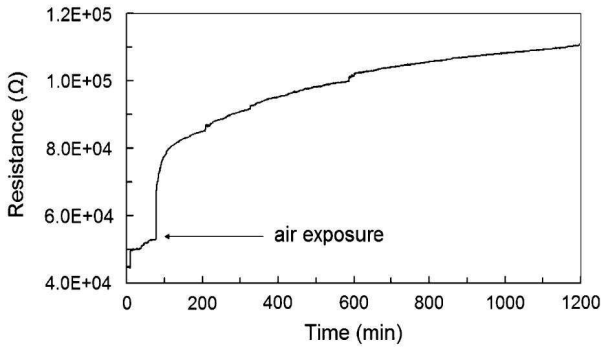

Figure 1.8: Resistance variation of bismuth cluster film with exposure to air at time = 80 seconds [21].

problems motivated the development of the next-generation cluster apparatus: the ultra-high-vacuum (UHV) system [23]. This system is described in detail in §2.1. The remaining parts of this section describe experiments with clusters deposited onto substrates with the UHV system.

Films of clusters have been used to make hydrogen sensors [24] and ammonia sensors [25]. Films of clusters were exposed to controlled amounts of gases and showed a resistance reduction effect for concentrations as low as 100 ppb. Further details of these sensors are discussed in the gas sensor chapter in §5.1.4. The electrical characterization of bismuth, antimony [26], copper [27], palladium [25] and tin [28] clusters has been performed and used to form various devices.

The effects of oxidation on cluster films have been studied. The resistance of bismuth cluster films have been monitored over time [21]. As films were exposed to controlled levels of oxygen, the resistance increased as a function of the oxygen pressure, and an example is shown in Figure 1.8. The behaviour was due to oxidation and all resistance-time curves followed a power law with the same time-exponent.

1.3.2 Nanowires Made from Clusters

This subsection describes the different methods for assembling clusters into nanowires used at Canterbury, including V-grooves [29], lithographic lift-off [30], templates of either photo-resist [31] or electron-beam resist [26, 31] and nanostencils [32]. These methods take advantage of the different interactions of clusters with substrates depending on the substrate type [33], and speed and size of the clusters [34].

V-grooves are a lithographically defined (see §2.3) feature etched into a silicon substrate. An AFM image of a V-groove is shown in Figure 1.9(left). V-grooves are produced by etching silicon with potassium hydroxide. When clusters are deposited

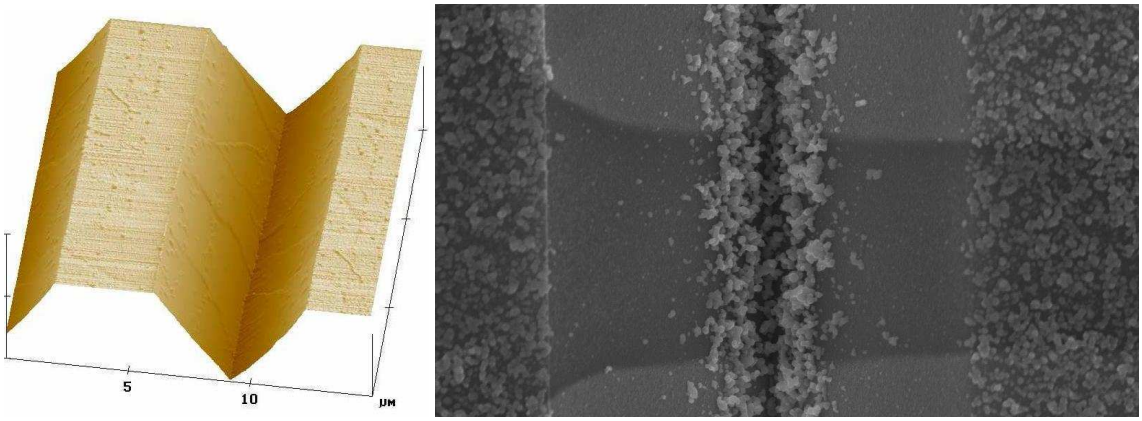

Figure 1.9: Left: AFM image of a V-groove in a silicon wafer, from [26]. Right: SEM image of a V-groove with bismuth clusters accumulated at the apex [29].

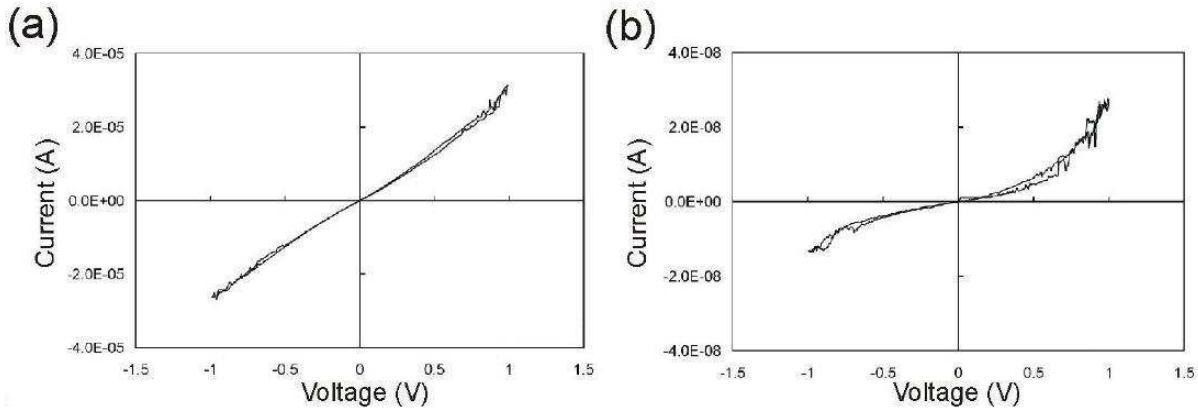

Figure 1.10: V-groove assembled bismuth cluster wire I(V) characteristics [29]. (a) Linear characteristics for low resistance wires. (b) Non-linear characteristics for high resistance wires.

on the grooves, they can bounce or slide to the apex, creating a wire [36, 37], shown in Figure 1.9(right). This process can create nanowires with smaller dimensions than those used in the lithography process. V-grooves of 2 μm width have created bismuth cluster-wires with diameters of 50 nm [29]. The cluster slide/bounce processes are momentum driven, so selecting the size and velocity of the clusters determines how they interact with the V-groove. If the V-groove sample has electrical contacts, then the V-groove wire can be electrically characterized. An example of the I(V) characteristics are shown in Figure 1.10. Low resistance wires ($\sim$25 kΩ) typically show Ohmic behaviour whereas high resistance wires ($\sim$25 MΩ) are non-Ohmic. The observed non-Ohmic behaviour is caused by contact-wire tunnelling.

Another method for creating nanowires is by using a lithographically patterned resist as a template for clusters. As above, the factors which determine the probability of a cluster being deposited onto a substrate are the size and velocity of the clusters and the type of substrate. If the reflection properties of two surfaces are known, then the cluster properties can be tuned so that deposition occurs only onto

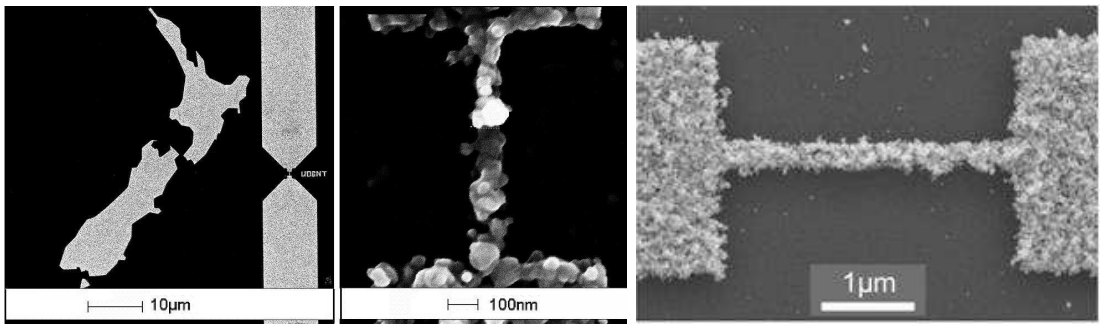

Figure 1.11: Left: SEM image of bismuth clusters deposited on a PMMA templated substrate, showing the arbitrary patterns possible. Middle: SEM image of a bismuth cluster nanowire using a PMMA template [32]. Right: SEM image of a bismuth cluster nanowire using an SU8 template [35].

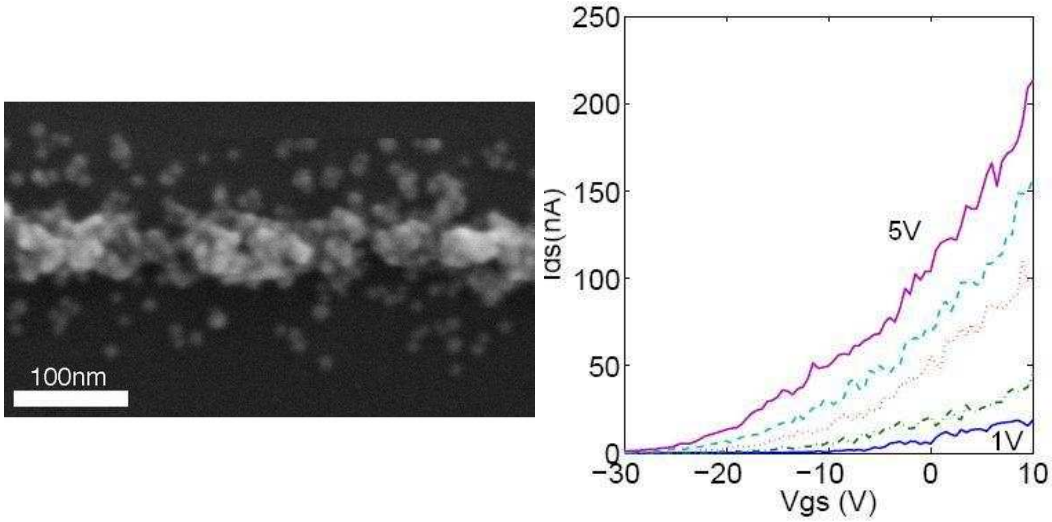

Figure 1.12: Left: Tin oxide nanowire formed using PMMA lift-off. Right: Source-drain current versus gate bias for 58 nm tin oxide clusterwire. Source-drain voltage from 1-5 V [30].

one surface. Using lithographic techniques, part of the substrate is patterned in resist. For certain cluster-beam conditions (typically >20 nm diameter, >100 sccm), the pattern in the resist will become filled with clusters; so the clusters self assemble into the desired pattern. The research relevant to this project is now discussed.

The PMMA aperture method is used in Chapter 3 to create bismuth structures with sidegates. Poly(methyl methacrylate) (PMMA) is an electron-sensitive resist used in electron beam lithography (EBL). PMMA can act as a positive resist and features down to 20 nm are possible (EBL is described in detail in §2.3.2). SU8 is a photosensitive resist, but can also used as a negative electron-beam resist. Both PMMA [32] and SU8 [35] have been used as templates for cluster deposition. Figure 1.11 shows bismuth clusters deposited on both PMMA and SU8 coated substrates. Wire widths of 100 nm have been produced. If cluster conditions are chosen so that clusters are deposited on both PMMA and the underlying substrate, then a lift-off stage is possible. An example of this is shown in Figure 1.12(left).

Cluster nanowires have also shown transistor-like behaviour. Tin clusters with 7 nm diameter have been produced using the magnetron sputtering source [30]. The clusters were deposited on PMMA apertures, but due to the small size of the clusters they were deposited on both the PMMA and the substrate. After deposition, cluster films are removed from vacuum and thermally oxidized to create tin oxide which is a semiconductor. When the PMMA is removed in acetone, a nanowire remains, shown in Figure 1.12(left). The nanowires show a response to a backgate bias, shown in Figure 1.12(right). These results are discussed in more detail in §3.2.

1.4 Research Outline

As previously described (§1.3), the cluster group at Canterbury is well established and has produced many different device types that are assembled from clusters. The tin oxide transistors described in §1.3.2 required removal from vacuum prior to gated measurements being performed[1]. It would be desirable to observe transistor-like behaviour in devices made from clusters in their native state, rather than an oxidized form of the device. With that aim in mind, two materials were investigated. Firstly, bismuth, a semimetallic material was studied. A field effect in bismuth has been observed for evaporated nanowires (see §3.1.3), but not previously for devices assembled from clusters. Secondly, germanium clusters were investigated. Germanium clusters had not previously been studied at Canterbury, so a new source was commissioned and built. Germanium is a semiconducting material and has well established research into its transistor behaviour. The remainder of this section contains an outline of the other chapters in this thesis.

Chapter 2 outlines the experimental methods and equipment. Initially, the inert gas aggregation source, deposition chamber and sample holders are described. The gas rig and modification to allow for humidity measurements are then outlined. The fabrication of samples used in this thesis is then detailed, both optical and electron-beam lithography are explained. Finally, the cluster deposition technique and details of electrical measurements are described.

Chapter 3 investigates the possibility of observing transistor behaviour in bismuth cluster devices. To begin, a review of bismuth is presented. Electric field effects have previously been observed in thermally evaporated bismuth nanowires and the electric-field effect mechanisms of a semimetal are discussed. Next, the evolution of the sample design and the issues involved in fabricating multiple side-by-side nanoscale apertures using electron-beam lithography are investigated. This precedes a discussion of the results of applying a gate bias to the channel of the sidegate devices.

Chapter 4 determines the feasibility of using the IGA deposition apparatus to produce germanium cluster devices. Firstly, the properties of germanium and the relevant literature are reviewed. Germanium clusters had not been produced previously at Canterbury. The next section discusses the redesign of the cluster source and the subsequent source characterization. Once the source was reliable, the electrical characterization of percolating films of germanium clusters was investigated and then both Hall and transistor measurements were performed.

Chapter 5 investigates the hydrogen and humidity sensing properties of films of

[1] tin clusters required oxidation before becoming semiconducting.

germanium clusters. Initially, the behaviour and mechanisms of both gas and humidity sensors are reviewed. Then germanium cluster films are exposed to hydrogen and humid air and are tested as hydrogen sensors and humidity sensors.

Chapter 2

Experimental Methods

This chapter outlines the experimental methods and equipment. Initially, the IGA source, deposition chamber and sample holders are outlined. The gas rig and modification to allow for humidity measurements is then described. The fabrication of samples used in this thesis are then detailed, and both optical and electron-beam lithography are explained. Finally, the cluster deposition technique and details of electrical measurements are outlined.

2.1 Apparatus for Cluster Production

At Canterbury, there are two systems for producing atomic clusters. The two systems use different methods to produce atomic vapour. One system uses a magnetron sputtering source and the other an inert-gas-aggregation (IGA) source. Only the IGA source was used for this thesis.

An existing IGA source for bismuth clusters was used for the experiments of Chapter 3. Modifications were made to the IGA source to produce germanium clusters, which were used in Chapters 4 and 5.

2.1.1 IGA Source of Bismuth Clusters

An IGA source heats a material in vacuum to produce atomic vapour. The vapour is cooled and aggregated by an inert gas to form clusters and then passed through nozzles to create a supersaturated beam of clusters. Figure 2.1 shows a schematic and photograph of the IGA cluster deposition apparatus which is located in room 117 of the Physics and Astronomy Department. The operation of the bismuth IGA system is now described.

A schematic of the IGA source for bismuth is shown in Figure 2.2. A boron nitride crucible containing 99.999% bismuth was heated to approximately 800°C in

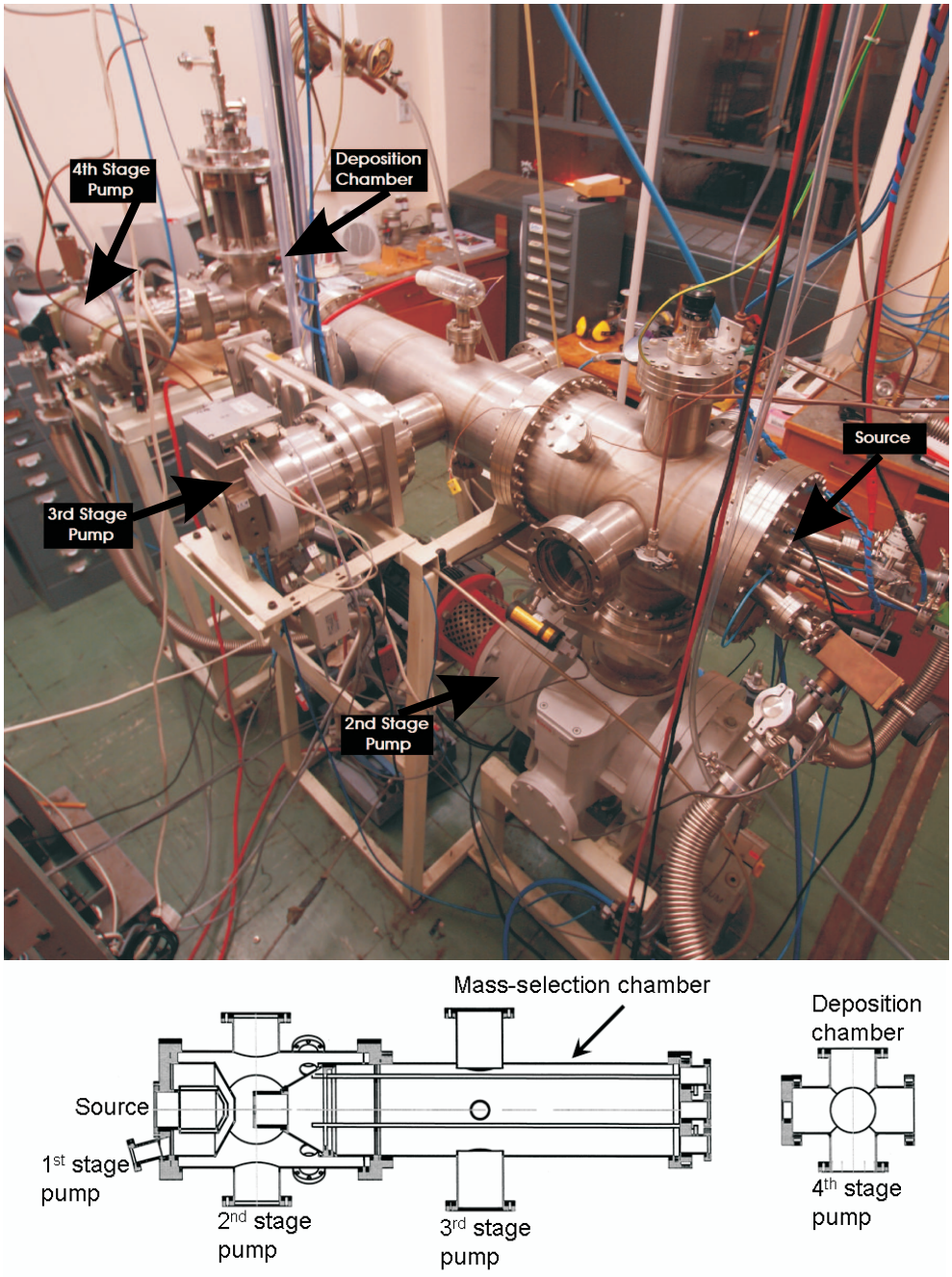

Figure 2.1: Top: Photograph of the IGA cluster source showing various pumping stages. Bottom: Schematic of IGA cluster deposition apparatus, showing various pumping stages [29].

order to provide the necessary amount of atomic vapour (and output cluster flux). Argon of 99.99% purity was introduced into the source chamber through a MKS-1179A flow-meter. The inert gas encourages clusters to form by allowing three-body collisions and condensation due to the room-temperature of the gas (for more details, see [9]). The source inlet argon gas flow-rate and crucible temperature controlled[1] the cluster size, deposition rate and average momentum of the clusters. The cluster

[1]with Omega K-type thermocouple and Omega CN1601 temperature controller.

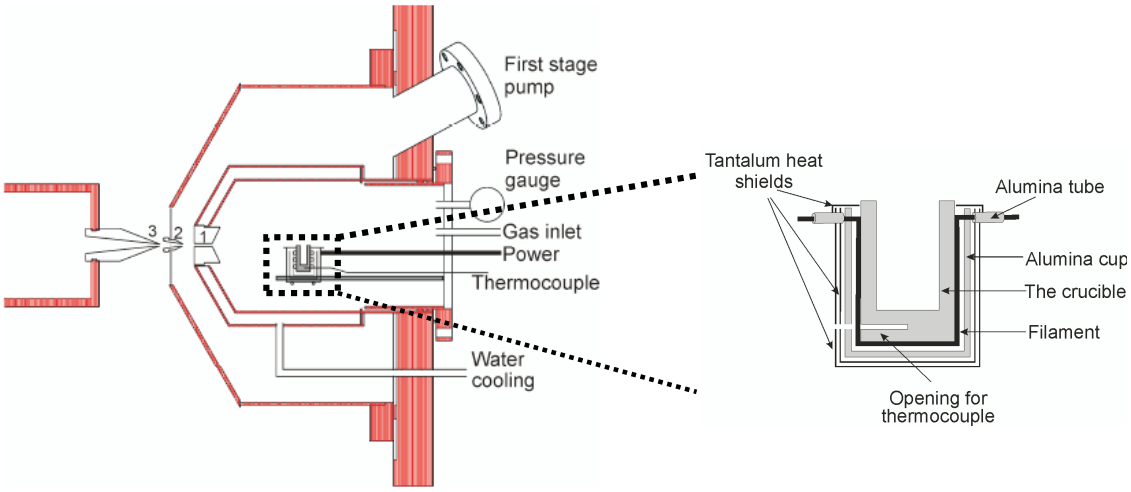

Figure 2.2: Schematic of the bismuth IGA source from [26].

beam was directed through an output nozzle and two further nozzles separating differential pumping stages (at successively lower pressures) then finally into the sample chamber. Details of these nozzles and pumping stages are shown in Tables 2.1 and 2.2. These pumping stages remove argon and drive the clusters towards the deposition chamber. The specially designed nozzles allow clusters to pass into the next pumping stage without disturbing the flow [9]. The mechanism driving the clusters through the nozzles and towards the deposition chamber is the pressure difference between the source chamber and the subsequent pumping stages. Only the argon is removed by these pumping stages due to the far greater comparative mass of the clusters.

In order to maintain a low temperature of the wall of the source chamber, tantalum heatshields were used. In addition, water was used to cool the walls of the source chamber and source backplate at a rate of 5 litre/minute and 1 litre/minute respectively. This cooling water provides a heatsink for the thermal radiation and also protection from the walls of the vacuum chambers from melting/heat deformation.

The cluster beamspot diverges as it travels towards the deposition chamber. In order to limit the size of the beam deposited on the sample holders, a solid copper gasket with a 10 mm hole is positioned close to the deposition chamber. This gasket ensures that the cluster beam is approximately 10 mm in diameter during deposition. Additional details of the bismuth source and IGA process in general can be found in the following documents and references within [9, 26].

2.1.2 Deposition Chamber and Cryostat

This subsection describes the UHV-compatible deposition chamber, sample holders and temperature control using the cryostat. A schematic of the deposition chamber and cryostat is shown in Figure 2.3(left).

The high vacuum chamber contains a retractable sample holder. This holds up to three samples, each with ten electrical contacts and electrical feed-throughs that enable electrical characterization of the devices whilst they remain in high vacuum.

In order to record electrical measurements in situ, three electrically contacted sample holders were attached to a Cryogenic Control Systems Model 32 cryostat. Each PTFE sample holder (Figure 2.3(right)) has ten spring-loaded contact pins and a centralized 3 mm×3 mm window that allows clusters to be deposited onto the

Nozzle	Length	Minimum diameter
1	40 mm	1.5 mm
2	12 mm	2 mm
3	40 mm	2.5 mm

Table 2.1: Dimensions of nozzles used in the bismuth IGA source, shown in Figure 2.1.

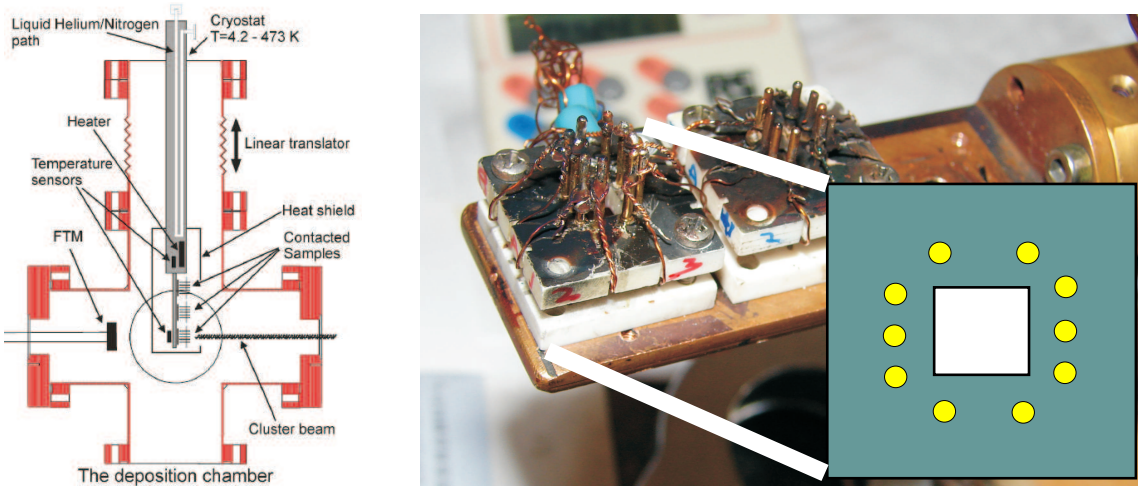

Figure 2.3: Left: Schematic of the deposition chamber showing the chamber, cryostat and location of FTM, temperature sensors and sample holders [26]. Right: Photograph of sample holders. Each sample hold has ten pins which can arbitrarily be used as electrical connections.(Right Inset): Schematic of the sample holder, showing locations of electrical connections (yellow) and deposition window (white).

Stage	Pressure during deposition	Pump Type
1	10^{-2} Torr	Edwards E2M18 rotary pump
2	10^{-3} Torr	Pfeiffer WKP1000 roots pump
3	10^{-6} Torr	Pfeiffer TC600 turbo pump
4	10^{-7} Torr	Pfeiffer TP270 turbo pump

Table 2.2: Pressures and pump types for the IGA source. Stages are from Figure 2.1.

underlying contacted substrates. The cryostat is mounted on a linear translator. This enables the sample holders to be positioned in and out of the cluster beam. At any time, the deposition chamber can be isolated from the first three stages by closing a gate valve.

The deposition rate was monitored with a Sycon STM-100 film thickness monitor (FTM). The FTM is positioned directly behind the sample holder and monitored both before and after cluster deposition.

Temperature Control

The sample holders are attached to a Janis ST-400 cryostat. Both liquid nitrogen and liquid helium have been used to reduce sample temperature. To obtain a sample temperature of 77 K, liquid nitrogen was simply poured into the cryostat. To obtain a sample temperature of 4.2 K, a Dewar and syphon were used. Liquid helium was transferred by a Cryovac valve connected to a rotary pump to control the amount of liquid helium flow from the Dewar to the cryostat. The heater and temperature sensors shown in Figure 2.3 were used to control the temperature with a Cryogenics Control Systems 32 temperature controller. This set up enabled accurate temperature control in the range of 4.2-300 K. The two temperature sensors allowed the temperature of the cryostat and the temperature of the sample arm to be monitored independently.

2.2 Gas Rig for Gas Sensor Testing

Separate to the IGA source is the gas test rig. The gas test rig allows samples to be tested for sensitivity to different gases at a range of different temperatures. §2.2.1 describes the gas rig and then modifications required for humidity sensor measurement are detailed in §2.2.2.

2.2.1 Chamber Design

Figure 2.4 shows the gas rig set up. A controlled flow of two types of gas is exposed to a contacted device and the change in resistance monitored.

Two MKS 117A flow rate regulators with 100 sccm range are controlled by a LabView interfaced PKS PR4000 flow controller. One flow controller is always connected to the inactive gas, synthetic air (79% nitrogen/21% oxygen). By varying the flow rate of the active gas (normally forming gas, 5% hydrogen/95% argon), the concentration can be accurately manipulated. The temperature of the sample can be controlled from room temperature up to 300°C using the temperature controller.

The test chamber consists of two sample holders with four electrical feedthroughs for each sample. The gas inlet is positioned at the center of the sample. The system is kept airtight by an o-ring and wingnuts.

The electrical measurements are recorded using LabView and Keithley voltage sources (6418), ammeters (6487) and voltmeters (2000). More details of data acquisition are described in §2.4.1. As the gas flow rate is varied, the resistance of the samples is monitored by having a fixed source-drain offset voltage and measuring the variation in current. Voltage, current, both flow rates and time are all recorded every three seconds. The gas flow of a typical experiments is shown in Figure 2.5. After one hour of synthetic air flow, thirty minute pulses of hydrogen are introduced to the test chamber.

2.2.2 Modification of Gas Rig for Humidity Measurements

In previous experiments using the gas rig, only dry gases have been used. The humid air became the active gas in from §2.2.1. In order to achieve this, synthetic air was made to bubble through deionized water in a sealed Pyrex flask. Another gas transfer tube then extracted humid air from the top of the flask. The flask and flask lid are shown in Figure 2.4(right). The flow rate of the humid air then was controlled by a flow controller and measurements were made as described above. The humidity was monitored with a HTF3227LF humidity sensor.

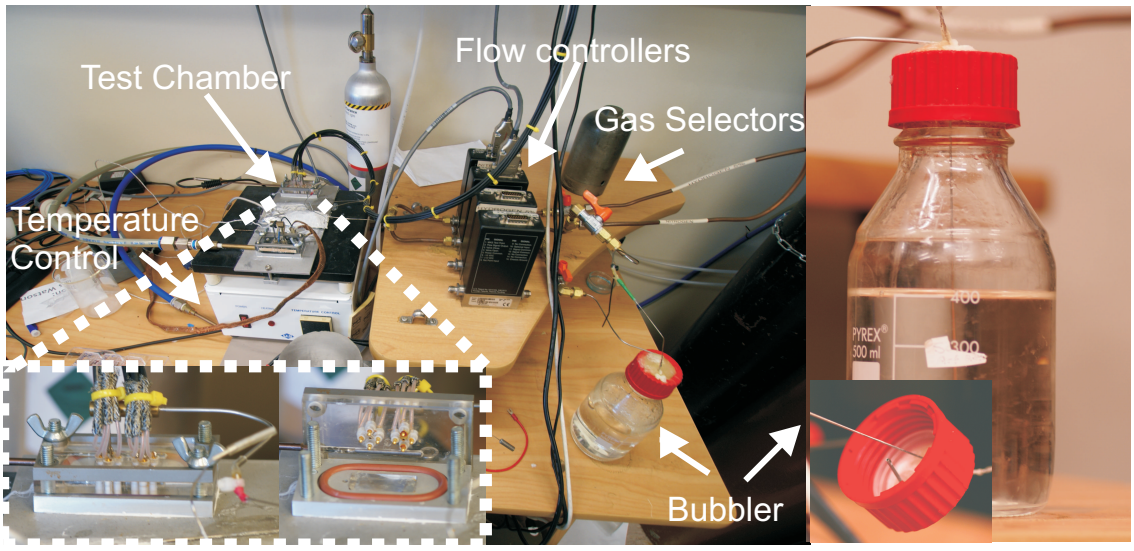

Figure 2.4: The gas test rig, showing sample holders and test chamber, heater, flow controllers, gas selectors and bubbler

.

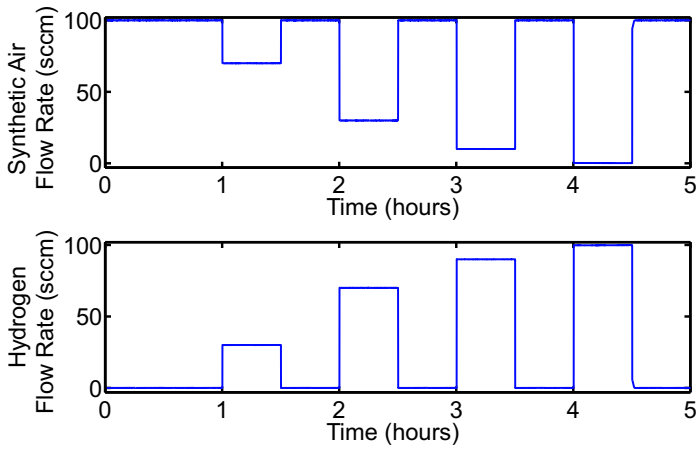

Figure 2.5: Typical flow rates of synthetic air and forming gas during a five hour experiment.

.

2.3 Sample Fabrication

Three techniques were used in the project to produce samples for cluster deposition: shadow mask evaporation, optical lithography and electron beam lithography. These techniques are described, followed by a list of the sample types used in this thesis.

2.3.1 Optical Lithography

Photolithography is the process where bare semiconducting wafers are patterned and electrically contacted in a sequence which relies on one or more layers of photo-sensitive polymer. Photolithography uses a patterned mask (normally commercially purchased chrome-on-glass) and electromagnetic radiation (normally ultraviolet) to expose photo-sensitive polymer layers spun onto semiconducting or insulating surfaces [38, 39]

The basic steps involved in semiconductor photolithography are described by way of an example (see Figure 2.6). All processing steps took place in a clean room laboratory environment to reduce the risk of sample contamination. The cleaning and spinning stages took place within a fume hood. The first step was to ensure the upper surface of the wafer is free from contaminants such as dust and biological matter. The wafers were immersed in analytical grade solvents; acetone and then immediately into isopropyl alcohol (IPA). Once removed from the IPA, the residual liquid was removed by use of a nitrogen gun. The electrical contacts were then defined using optical lithography.

AZ1500 photoresist was spun at 4000 rpm for 45 seconds using a Laurrels 400B

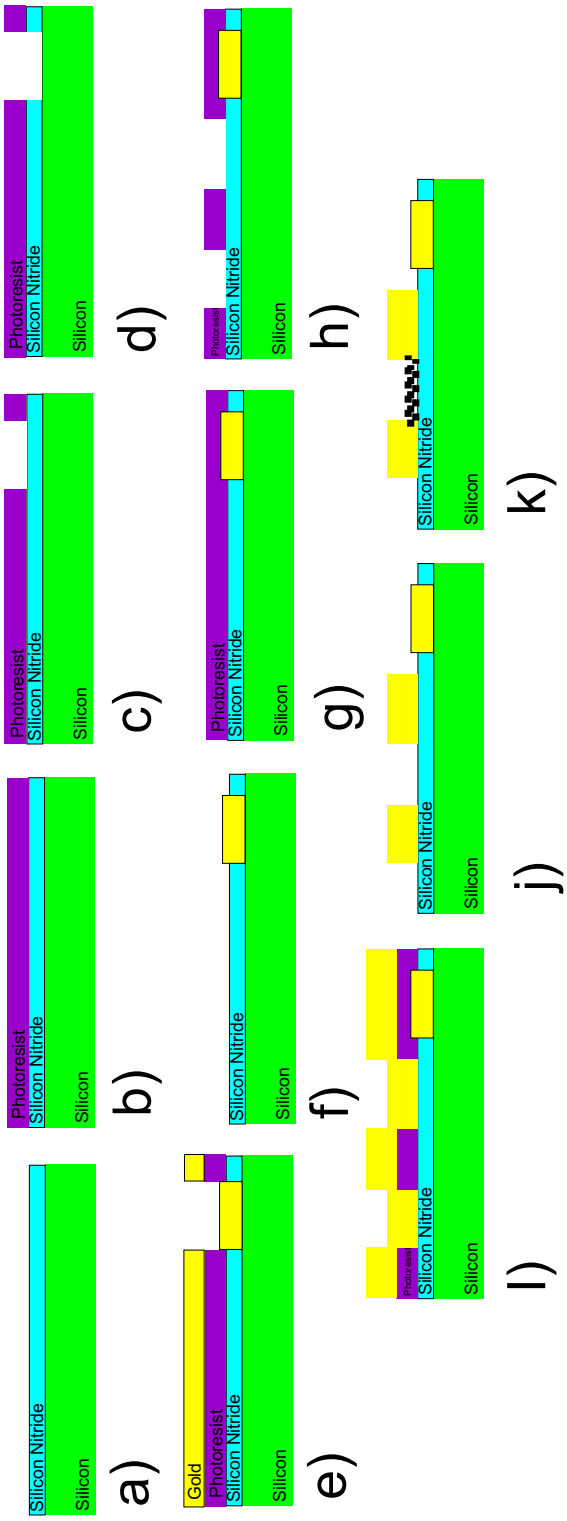

Figure 2.6: Steps of photolithography. a): Silicon/silicon nitride substrate is cleaned. b): Layer of photoresist applied. c): Photoresist is patterned. d): Silicon nitride is dry-etched. e): NiCr/Gold evaporation. f): Removal of photoresist. g): Layer of photoresist applied. h): Patterning of photoresist. i): NiCr/Gold evaporation. j): Removal of photo resist. k): Completed substrate with gated and non-gated electrical contacts.

.

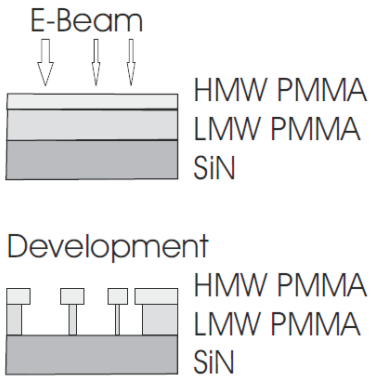

Figure 2.7: Schematic of the bilayer PMMA process leading to an undercut [26].

.

resist spinner. This provided a coating of photoresist[2] of 300 nm ± 10 nm. Wafers were then transferred to a covered Floroware container and baked at 95.0°C for at least 30 minutes. Using a Karl Suss MJB 3 mask aligner, samples were exposed for 12.00 seconds. The chemical development process was then performed. To aid in the later lift-off process, a larger version of the mask pattern is required to be chemically removed and this is known as an undercut. To create an undercut, each sample was dipped in toluene for 30 seconds, and then dried with nitrogen.

The next step was chemical development. Samples were developed using AZ300M for 30 seconds, then rinsed with deionized water and dried with nitrogen.

Metal evaporation followed and was performed using an Edwards 306 thermal vacuum coater. The vacuum chamber was reduced to a pressure of 1×10^{-6} mb. A 5 nm layer of 99.99 % NiCr was evaporated followed by a 45 nm evaporation of 99.99 % gold. Once removed from vacuum, the samples were immersed in acetone for the lift-off stage. After at least 2 hours in acetone, the samples were moved to a low powered Transonic 460/H ultrasonic bath for intervals of 1 minute until lift-off was successful.

Wafers were now ready to be separated into individual samples. A Tempress 602 dicing saw with a Disco S2530 blade was used to cut all but 2 mm of the wafer into a 10 mm×10 mm grid. Individual samples could now be removed from one another with a small force between them. Samples were now checked for current leaks using the equipment in the UHV lab. This is described in §2.4.2.

2.3.2 Electron Beam Lithography

In Electron Beam Lithography (EBL) finely detailed patterns are written into a polymer using a focused beam of high energy (10 - 100 keV) electrons from a modified

[2]Thickness are known from commercially supplied data of spinning speed/resist type

scanning electron microscope (SEM). The electron beam is controlled by a computer, so a software pattern is required instead of a mask. The resolution of an EBL system is greater than using optical lithography and feature sizes as low as 20 nm are feasible. EBL has played an important role in the development of nanotechnology with the ability to create submicron features.

A different type of resist was used compared to photolithography: the polymer PMMA which is sensitive to the electron beam of an SEM. Initially, low molecular weight (LMW) PMMA was dissolved in chlorobenzene to give a solution with 4% LMW PMMA. After substrates were cleaned with acetone and IPA, the LMW PMMA solution was spun at 4000 rpm for 45 seconds which gave a layer thickness of 200 nm. The PMMA was then hardbaked at 185 °C for at least 30 minutes. This LMW layer acts as an undercut in the later lift-off process (Figure 2.7) as it is far more sensitive to the electron beam. The upper PMMA layer used high molecular weight (HMW) 2.5% PMMA in a solution of xylene and was applied using the same technique as with the LMW PMMA. This process[3] gave a total thickness of 240 nm.

The next process was defining the pattern using the Raith 150 field effect scanning electron microscope (FE-SEM). The FE-SEM was used with an accelerating voltage of 10 keV and an aperture size of 30 μm. These settings resulted in a beam current of $\sim$165 pA. The samples were written with beam focused to a spotsize of approximately 50 nm. The samples were developed in a room temperature mixture of 3:1 IPA:methyl isobutyl ketone (MIBK) for 45 seconds and then rinsed with IPA and dried with nitrogen.

Samples were now ready for either metal evaporation and lift-off, or, in the case of the PMMA aperture method, were ready for cluster deposition.

2.3.3 Percolation Samples

The most basic sample used for electrical characterization is the *percolation sample*. Percolation samples consist of a silicon/silicon nitride substrate with two gold contacts separated by a 100 μm, as shown in Figure 2.8(left).

Percolation samples were fabricated in batches of twenty five. A clean silicon/silicon nitride wafer was loaded into the thermal evaporator under a shadow mask. Metal evaporation of 5 nm of NiCr and 45 nm of gold were deposited as described in §2.3.1. The samples were now ready to be separated and were done so using the dicing saw as previously described. After the surface of the samples had been cleaned with acetone and IPA, they were ready for cluster deposition.

[3]For the PMMA aperture technique, no lift-off is required, hence only the HMW PMMA layer is necessary.

2.3.4 Hall Samples

Hall samples were used for the characterization of germanium clusters and have two gated contacts and eight non-gated contacts. The Hall samples are used in §5.2-§5.4.

Figure 2.8(right) shows the contact layout of the Hall samples. The contacts were produced by optical lithography methods as described in §2.3.1. Once the pattern in Figure 2.8(right) was complete, an additional photoresist layer was spun and the mask in Figure 2.8(middle) defined. This layer created a passivation layer to ensure that any conduction measured is attributed to the 200 μm$\times$1000 μm film. For additional details of Hall samples, see §5.2.2.

2.3.5 PMMA Aperture Samples

PMMA aperture samples were used in Chapter 3 to create sidegated structures. An investigation was carried out to determine the lowest width limit possible for cluster depositions using the PMMA aperture method. Further details of the design and results are discussed in §3.2.

2.4 Cluster Device Characterization

2.4.1 Electrical Measurements

When substrates were mounted in the sample holder (Figure 2.3(right)), in situ electrical measurements could be performed both during and after cluster deposition. The two-terminal circuit used to measure onset of conduction is shown in Figure 2.9(left). In order to perform these measurements, a custom-made voltage supply (range 1 mV to 14.5 V) was used. Current and voltage were recorded by LabView interfaced Keithley 6514 electrometers and 2000 multimeters respectively.

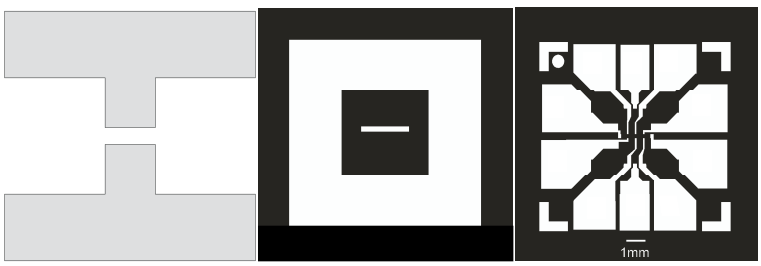

Figure 2.8: Left: Schematic of percolation sample. Gap between electrodes = 100 μm. [26]. Middle/Right: Contact mask design for Hall samples. Middle: Passivation pattern with slot size of 200 μm$\times$1000 μm. Right: Electrical contact layout of Hall samples.

.

Onset of Conduction

To measure an onset of conduction, a fixed source-drain voltage was applied. The applied voltage was 50 mV for bismuth or 5 V for germanium. When the current increased from the leakage levels of 10 pA, this indicated that clusters had formed an electrically conducting device, and the deposition was stopped. The current, voltage, temperature and time were recorded every 200 ms.

Current-Voltage Characteristics

After deposition, the current-voltage characteristics of devices were normally recorded. To do this, the circuit in Figure 2.9(left) was used. The source-drain voltage was ramped in a sawtooth wave, with a ten minute period. For the case of germanium, up to ±10 V was used. However, in the case of bismuth nanowires, an offset of 10 V would produce a current that would destroy the device due to resistive heating. Hence, the maximum I(V) voltage range used for bismuth nanowires was ±100 mV.

Gated Measurements

In the case of back-gate measurements, the gate bias was ramped up to 100 V. Figure 2.9(right) shows a schematic of the circuit. In the case of gated measurements, a different voltage source was used to supply the gate voltage. The LabView controlled Keithley 6487 voltage source was used. Two Keithley 6514 electrometers were also used, one to record source-drain current and the other to record any leakage current between the gate and channel.

Other measurement setups, such as circuits for annealing wires and Hall measurements, are discussed in the relevant chapters.

2.4.2 Pre-Deposition Sample Characteristics

Prior to deposition, the contacts of all samples were tested for current leaks to ensure any behaviour observed after cluster deposition was attributed to the cluster device.

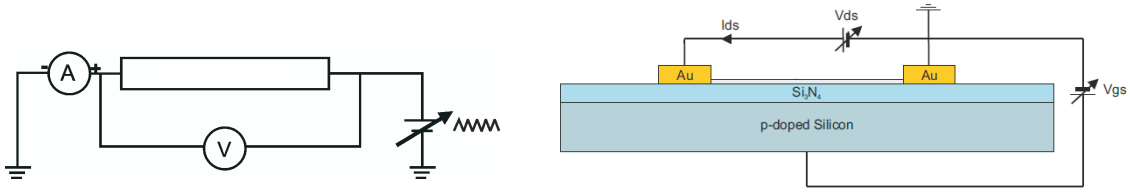

Figure 2.9: Measurement circuits of (left) onset of conduction [29] and (right) back-gated transistor measurements [28].

.

The leakage was tested by performing pre-onset current-voltage characteristics in the $\pm 10\,\mathrm{V}$ range as described in §2.4.1. Figure 2.10 shows three I(V) curves performed on percolation samples prior to cluster deposition. When taking I(V) measurements of high resistivity samples, a hysteresis leakage curve appears. This is caused by the capacitance of the sample and the voltage ramp.

$$q = CV, i = \frac{dq}{dt}, \therefore i = C\frac{dV}{dt} \tag{2.1}$$

The hysteresis current can be changed by increasing or decreasing the speed of the voltage ramp, hence the hysteresis is caused by a capacitance effect. The capacitance could have contributions from the voltage source/ammeter, the coaxial cables, the sample holder or the substrate itself.

If a current above 200 pA was observed during the pre-onset measurements, the sample was rejected and not deposited onto. A comparison of pre-deposition and and post-deposition electrical characteristics can become important if the films are highly resistive, as is the case for several thin film germanium devices. This so-called capacitive charging is also potentially important when ramping a gate bias on a highly resistive device as the effect can cause a measured current in the device due to Equation 2.1, shown in the green curve of Figure 2.10. Figure 2.10 shows three different types of percolation style samples all with different capacitive charging effects. The blue curve shows a quartz substrate with a very small amount of capacitive charging. The red and green curves show silicon substrates with and without a direction connection to the silicon, respectively. All the samples in Figure 2.10 have gold contacts.

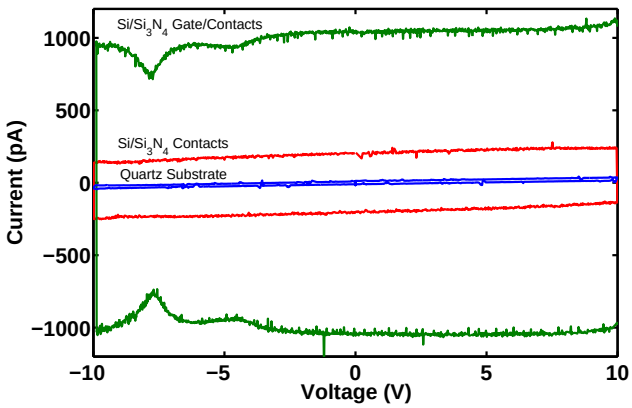

Figure 2.10: Pre-onset I(V) characteristics of percolation samples show substrate-dependent hysteresis showing three different sample types.

.

Chapter 3

Bismuth Cluster Structures with Side Gates

The previous chapters have introduced nanotechnology and atomic clusters (Chapter 1) and discussed the methods of producing clusters using an inert-gas-aggregation source and the fabrication of samples (Chapter 2). This chapter explores the possibility of using the PMMA-aperture method (§1.3.2) to create a bismuth cluster device with a sidegate. A sidegated device enables field effect measurements to be performed.

To begin, a review of bismuth is presented in §3.1. Electric field effects (EFEs) have previously been observed in thermally evaporated bismuth nanowires and the electric field effect mechanisms of a semimetal are discussed. §3.2 then discusses the evolution of the sample design and the issues involved in fabricating multiple side-by-side nanoscale apertures using electron beam lithography and details the limitations of the PMMA aperture method. §3.3 discusses the results of applying a gate bias to the sidegate devices. Results are discussed and then conclusions are drawn in §3.4.

3.1 Bismuth

This section contains a review of the general and electrical properties of bulk bismuth, the properties of bismuth thin films, nanowires and nanoparticles, the electric field effects of bismuth devices and finally discusses the electric field mechanisms of bismuth cluster devices.

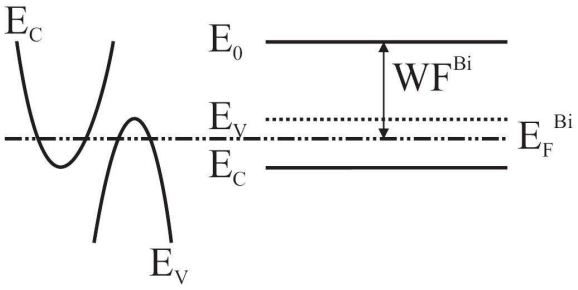

Figure 3.1: Energy band diagrams for bismuth, from [26].

3.1.1 Bismuth: General and Electrical Properties

Bismuth (Bi) is an elemental semimetal with atomic number 83 [40]. Bismuth has a melting point of 271°C, a density of 9.82 g/cm^3 [41], a vapour pressure of 1 Torr at 670°C, and a bulk rhombohedral structure with lattice constant of 4.746 Å [42].

The electrical properties of bismuth are dominated by its semimetallic nature. Semimetals have a small overlap of the valence and conduction bands, so they have intermediate properties between semiconductors and metals. The energy bands of bulk bismuth are shown in Figure 3.1. For the case of bismuth, the carrier concentration is 3×10^{17}cm^{-3} at 300 K [42], which is orders of magnitude higher than a semiconductor ($\sim10^{13}$cm^{-3} for intrinsic germanium at 300 K [43]), but several orders of magnitude lower when compared to 10^{22}cm^{-3}, for a typical metal [44].

Bismuth has interesting size-dependent electrical properties, which motivates much bismuth research. In bismuth, the electron mean-free path is ∼100 nm at room temperature [45] and Fermi wavelength is ∼40 nm [46] which are both much larger than the typical value of 0.1 nm for metals [44]. Some size-dependent properties are influenced by the Fermi wavelength of a material, hence quantum confinement effects are theoretically observable in bismuth at high temperatures and for relatively large structures.

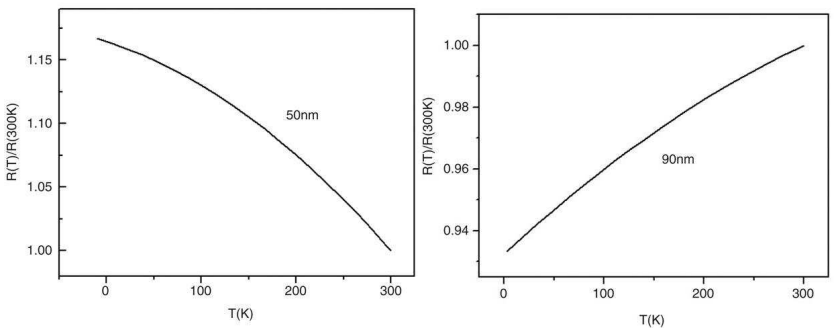

Figure 3.2: Temperature dependent resistance for bismuth nanowires of (Left): 50 nm and (Right): 90 nm [47].

Transition size	Reference	Film/wire
20-30 nm	[48]	Film
25-40 nm	[49]	Film
65 nm	[50]	Wires
75 nm	[51]	Wires
75 nm	[47]	Wires
50 nm	[52]	Wires

Table 3.1: Semimetal to semiconductor transition size for various films and nanowires.

3.1.2 Size Effects in Bismuth Thin Films and Nanowires

Size-dependent effects can be measured in bismuth, for instance via a blueshift in infrared spectra [51, 53], magnetoresistance data [54–56], as well as the resistivity/mobility measurements. Bismuth films [48, 49, 57, 58] and wires [47, 50–52] have shown temperature-dependent resistivity size effects.

The resistivity of metals decreases with temperature and this is the case with bulk bismuth. Bulk metals and semimetals have a positive temperature coefficient of resistance (TCR). For bismuth films or wires, if the dimensions are small enough, the TCR switches sign and becomes negative. The transition temperatures for different films and wires are shown in Table 3.1 and an example of a TCR transition is shown in Figure 3.2. The data from Table 3.1 suggest a smaller transition length for films, compared to wires. The TCR change is consistent with a semimetal to semiconductor transition [44]. For a semimetal-to-semiconductor transition, the small band overlap of bismuth (Figure 3.1) must become a bandgap.

3.1.3 Bismuth: Electric Field Effects

If bismuth is to be used as a gateable material for field effect transistors (FETs are described in §1.1), an electric field must be able to enhance and deplete the charge carriers. It is important to note that the mechanism of an EFE in a doped semiconductor is different to a semimetal. This is due to the small band overlap, since under

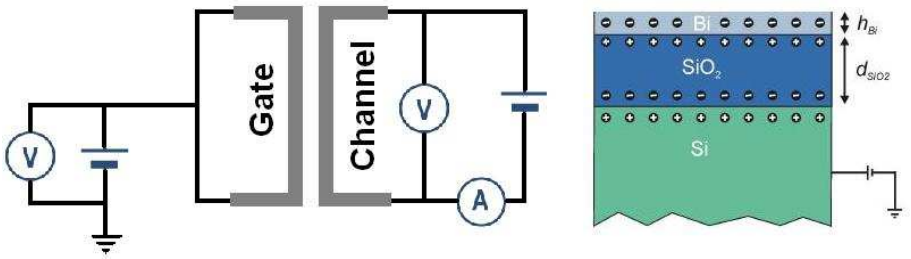

Figure 3.3: Schematic circuit layout of Left: sidegated transistor. Right: Backgated bismuth transistor, from [29].

ΔR	Diameter	Temperature	Electric Field	Reference
0.4%	130 nm	15 K	10^8V/m	[59]
1%	15 nm	2 K	10^7V/m	[60]
10%	60 nm	2 K	10^7V/m	[61]

Table 3.2: Change in resistance of bismuth wires due to applied gate bias.

zero-bias conditions bismuth has an equal number of electrons and holes contributing to conduction. Intrinsic semiconductors also have an equal number of electrons and holes contributing to conduction, but at much lower carrier concentrations.

When a gate bias is applied to a semimetal, it can raise or lower the Fermi level. Because bismuth has a small band overlap (see Figure 3.1), it is possible to lower the Fermi level below the level of the conduction band with a negative gate bias. This means that only holes contribute to conduction. If a positive gate bias is applied, the Fermi level is raised and the conduction becomes dominated by electrons. Hence, the main difference between the EFE of semimetals and doped semiconductors is that for semimetals the gate voltage cannot completely remove the carriers in the channel, so any effect due to current enhancement or depletion is expected to be relatively small.

An electric field effect has been observed in bismuth contacts [62], films [59, 63] and nanowires [60, 61] and results are summarized in Table 3.2. All wires listed in Table 3.2 have been deposited via thermal evaporation. The bismuth field effect has been observed using both a backgate and a sidegate; these circuit schematics are shown in Figure 3.3. Field effects have only been observed at low temperatures and with a change in resistivity of up to 10%.

Figure 3.3(left) shows the structures that will be created and studied in this Chapter and Figure 3.3(right) shows the backgated sample style used in Chapter 4 and Chapter 5. The possible electric field effect mechanisms relevant to gated bismuth cluster devices are now discussed.

3.1.4 Bismuth Cluster EFE Mechanisms

Because the mechanisms of a field effect in bismuth are different from a field effect in a doped semiconductor, a discussion of the potential mechanisms is required. Three field effect models are considered.

The first model assumes that a small amount of carrier concentration depletion/enrichment is possible within a semimetal, behaving as a semiconductor. This model relies on a change in the position of the Fermi level relative to the small band overlap of bismuth (Figure 3.1) to make a measurable change in conductance. The second model explains a change in conductance by a gate dependence of the barrier

height at the metal/semimetal junction. The third model assumes the conduction between cluster boundaries is affected.

Model 1: Electric Field Effect

Provided the electric field screening length of bismuth wires made from clusters is non-zero, then an electric field effect is theoretically possible. If the gate is held at a set voltage, the capacitative charging between the wire and gate can accumulate (or deplete) charges in the channel. This leads to a gate-voltage-dependent effective doping of the channel [2].

$$N_d = \frac{Q_d}{eV} = \frac{CV_g}{eAt} \tag{3.1}$$

where V_g = gate voltage, Q = accumulated charge, t = wire height, A = wire surface area and C = the capacitance between the wires. The capacitance between two parallel conductors (See Figure 3.3(left)) is [64]:

$$C = \frac{\pi\epsilon_0\epsilon_r l}{\ln\frac{\pi d}{w+t}} \tag{3.2}$$

where w = wire diameter, d = distance between the center of wires, l = wire length, t = wire height, and ϵ_r = permittivity of substrate. Substituting Equation 3.2 into Equation 3.1 yields:

$$N_d = \frac{\pi\epsilon V_g}{wet\ln\frac{\pi d}{w+t}} \tag{3.3}$$

A gate voltage of 100 V and the dimensions of the Sidegate Samples from §3.2.6 give a density of accumulated charge carriers of $1\times10^{18}\text{cm}^{-3}$, which is closely matched to the bismuth carrier concentrations at room temperature ($3\times10^{18}\text{cm}^{-3}$) [42] and at 2 K ($5\times10^{17}\text{cm}^{-3}$) [65]. Therefore, if the wire can be fully penetrated by the electric field from the gate voltage, then $1\times10^{18}\text{cm}^{-3}$ electrons will be accumulated for a positive V_g, or depleted if V_g is negative. Doubling the carrier concentration should half the measured resistance from Equation 4.5.

Model 2: Semimetal-Metal Junction Model

When bismuth and gold are brought into contact (as shown in Figure 3.4(b)), thermal equilibrium is established via band bending and a Schottky barrier[1] is created. In the bismuth depletion region, the conduction band is raised above the Fermi level which creates a barrier experienced by electrons, but not holes. If a positive gate voltage is applied, as in Figure 3.4(c), the Fermi level in bismuth is raised. The increased Fermi level is due to the influx of electrons which accumulate in the

[1]Further details on band bending and contact barriers discussed in §4.1.4.

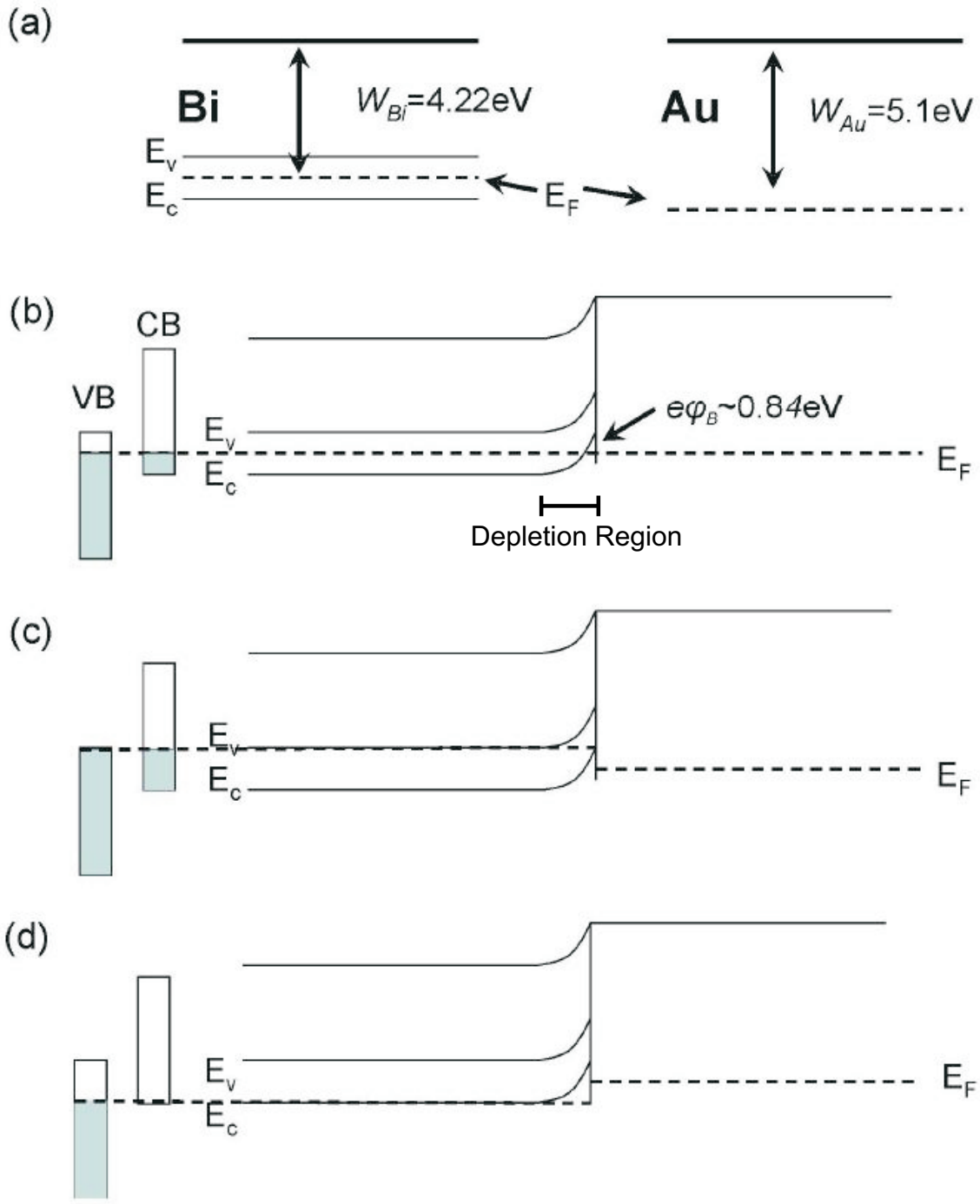

Figure 3.4: Sketch of band diagrams of bismuth junction with gold showing the valence bands and conduction bands. W_{Au} and W_{Bi} are the workfunctions of gold and bismuth, E_F is the Fermi level and the valence and conduction bands are E_V and E_C. a): Before contact b): V_g=0, at thermal equilibrium. Bands bend up causing a barrier for electrons. c): V_g >0, Fermi level in bismuth raised and d): V_g <0, Fermi level in bismuth lowered. From [29].

wire. This accumulation reduces the gold-bismuth junction barrier for electrons. Although (under zero-bias conditions) bismuth has an equal number of electrons and holes contributing to conduction and the number of holes is reduced under positive bias conditions, the mobility of electrons in bismuth is ten times higher than that of holes [42]. With a negative gate bias (Figure 3.4(d)), the number of holes in the bismuth wire increases and the number of electrons decreases. The electron barrier height at the gold-bismuth junction is increased, and if the Fermi level is moved down by 20 meV then the conduction band will be empty, meaning only holes[2] are contributing to conduction. Using this model, it would be expected that a positive gate bias should enhance the conductance of bismuth to a larger magnitude than the same negative gate bias would deplete conductance. The change in the Fermi level in model 2 is the same mechanism as in model 1, however, in model 2 the Schottky barrier has a significant effect on the device resistance and gate effect.

Model 3: Cluster Boundary Effects

The main feature that distinguishes the bismuth field effect devices studied in the literature from samples in this project that the devices are not thermally evaporated; they are constructed from clusters. Cluster devices inherently have boundaries between the clusters which can affect the electrical properties. The boundary between clusters can increase the resistivity of a device in several ways, including:

1. Grain boundary scattering: Clusters are deposited at random crystal orientations and this interface increases device resistivity.

2. Thin oxide layer between clusters, where the oxide acts as an insulator and tunnelling is required for charge carriers to contribute to conduction.

3. Thin oxide layer between clusters, where the oxide acts as an insulator, but for the charge carriers to contribute to conduction, they must overcome a classical barrier.

Consider case 3. Bismuth oxide, Bi_2O_3, has a bandgap of $\sim$2.5 eV [66] and a work function of $\sim$3.4 eV [67, 68]. Using this information and the equivalent bismuth data, the band diagrams and junction barriers can be sketched; Figure 3.5 shows the band diagram for two bismuth clusters with a Bi_2O_3 shell between them. Energies in this Figure are to scale.

Figure 3.5(a) shows the band diagram of two bismuth clusters separated from a region of bismuth oxide. Figure 3.5(b) shows the bands of bismuth slightly bend

[2]Excluding electrons able to conduct through thermal excitation.

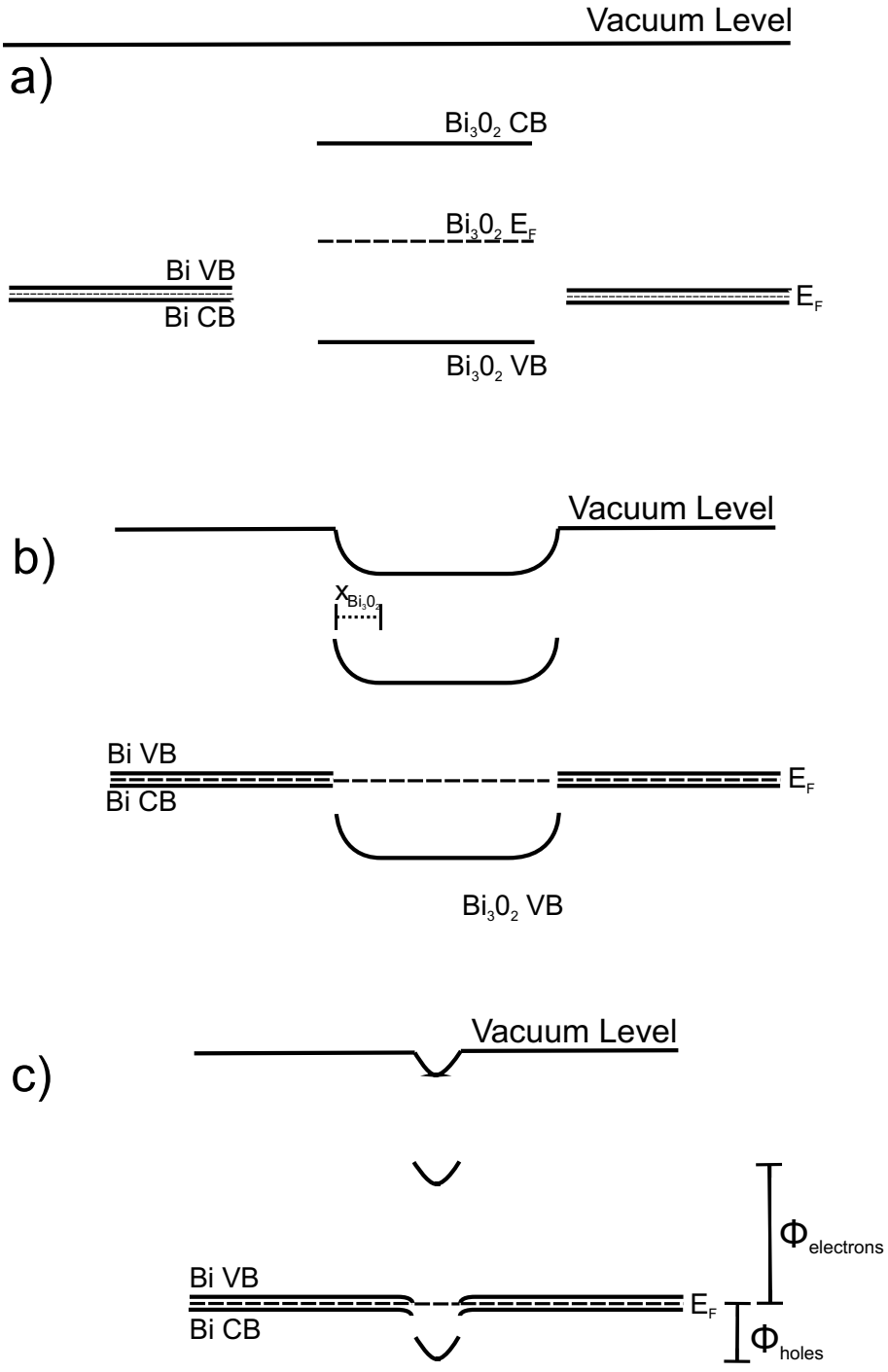

Figure 3.5: Theoretical band diagrams of the bismuth-bismuth oxide junction showing the valence bands and conduction bands. E_F is the Fermi level and the valence and conduction bands are VB and CB, the depletion length of bismuth oxide is $x_{Bi_3O_2}$ and Φ signifies barrier height. a): Before contact b): At thermal equilibrium. Bismuth oxide bands bend up increasing the barrier for electrons. c): Thermal equilibrium for a small oxide thickness.

down because the work function of Bi_2O_3 is less than the work function of bismuth. This means in the depletion region the conduction bands of bismuth and Bi_2O_3 move apart while the valence bands move closer together. The full amount of band bending possible is shown in this diagram and occurs in the depletion region $x_{Bi_2O_3}$.

The distance of a depletion layer depends on the carrier concentration of the material and an evaluation for this system is now attempted. The space-charge distance, d, as a function of the difference in valence band heights ΔE is [69]:

$$d^2 = \frac{2\epsilon\Delta E}{eN_d} \tag{3.4}$$

The space-charge distance for bismuth (in the bismuth/Bi_2O_3 junction) is calculated as 6 nm. The space-charge distance for Bi_2O_3 can not be calculated directly because the carrier density is not known. Even if Bi_2O_3 had the same carrier concentration as bismuth, then the space-charge region would be 6 nm and exceed the length of the oxide. The assumption is made that $N_{bismuth} \gg N_{bismuthoxide}$, therefore can be assumed the entire bismuth oxide layer[3] is considered to be affected by the band bending. A band-bending diagram for a bismuth/Bi_2O_3/bismuth junction for the case where space-charge $\text{distance}_{Bi_2O_3} \gg \text{length}_{Bi_2O_3}$ is shown in Figure 3.5(c). In this model, the barrier for holes is less than the barrier for electrons.

In order to realize the possibility of making field effect measurements in devices made from bismuth clusters, they must be assembled into a device. One method for doing so is the PMMA aperture method which assembles clusters using a PMMA template. The details are discussed in the following section.

[3]Bismuth oxide layer while the device is in high vacuum.

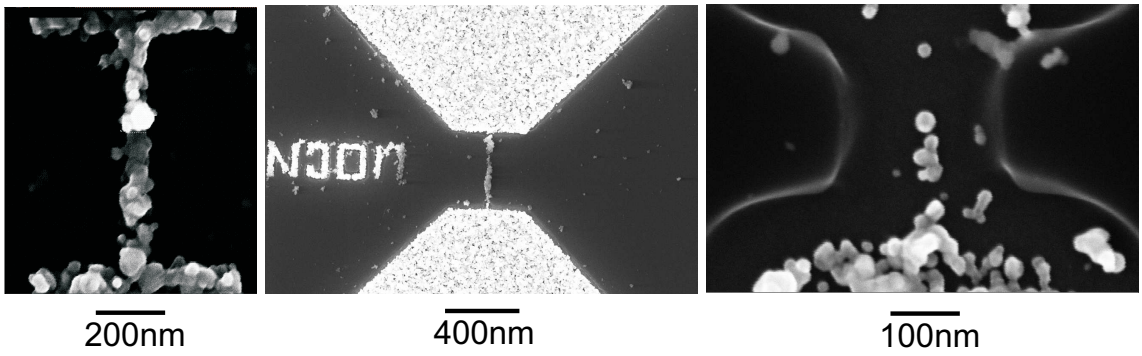

Figure 3.6: Bismuth clusters deposited into PMMA apertures of (Left): 100 nm [32], (Middle): 50 nm and (Right): 25 nm.

3.2 Adaptation of the PMMA Aperture Method

As seen in §3.1.3, field effects in bismuth wires have been observed when the channel has been less than 150 nm wide. Therefore, in order for a gate effect to be maximized in a bismuth device, a wire width of under 200 nm is desired. Nanowires of these dimensions are possible using the IGA source and the PMMA aperture method (§2.3.2). Experiments were performed to determine the lower width limitation of the PMMA aperture technique.

This section explains how the limitation of the PMMA aperture method was determined, how the Raith EBL system was used to produced sub-100 nm features in PMMA, and how those features were used to construct a sidegated device from bismuth clusters.

3.2.1 Limitations of the PMMA Aperture Method

An investigation was carried out to determine the smallest width possible for cluster depositions using the PMMA aperture method[4] for the purpose of fabricating sidegated devices with very narrow wires so that any gate effect was more likely to be detected. In previous research at Canterbury [32] nanowires of 100 nm diameter have been produced (Figure 3.6(left)). PMMA aperture samples were formed using bismuth clusters from the IGA source heated to between 765°C and 840°C and using an argon flow rate of 180 sccm.

To produce narrower trenches in PMMA, the original pattern file was modified in Wavemaker. The smaller slot samples were prepared using the same preparation technique as the 100 nm wide wire, with electron beam area dose = 120 μC/cm^2, electron beam line dose = 120 μC/cm and development time of 60 s. Several samples of each wire diameter were produced and one of each size was checked post develop-

[4]See §1.3.2 for PMMA aperture details and §2.3.2 for fabrication details.

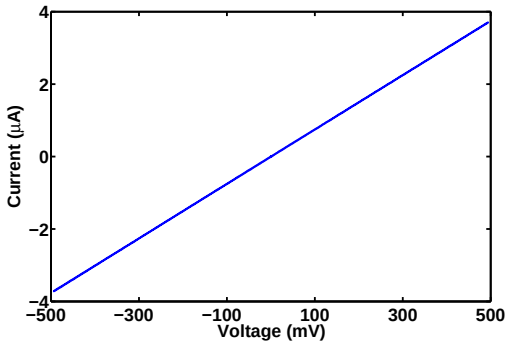

Figure 3.7: Current-voltage characteristics of a 50 nm wide bismuth wire made using the PMMA aperture method showing an Ohmic resistance of 125 kΩ. SEM image of this wire is shown in Figure 3.6(middle).

ment with the SEM to ensure that slot sizes were accurately written. Samples with 50 nm wide slots (Figure 3.6(middle)) shows the typical sharp onset of conduction behaviour expected for bismuth cluster devices. I(V) characterization revealed the wires were Ohmic, an example of the I(V) curve of a 125 kΩ wire is shown in Figure 3.7.

25 nm Width PMMA Aperture

The smallest PMMA aperture dimension attempted was a wire of 25 nm width. The 25 nm trench is close to the lower writing limit of the Raith 150 EBL system and smaller than the average diameter of a bismuth cluster produced in the IGA source. No onset of conduction was detected with a 25 nm width PMMA aperture sample and the results of the deposition are shown in Figure 3.6(right). A small number of clusters were able to be deposited in the trench. However, at one point in the wire a few clusters were deposited outside the boundary of the trench which created a 50 nm wide section. This so-called *overflowing* of PMMA trenches occurs when a large amount of material is deposited. The overflowing of trenches has consequences for how close PMMA apertures can be placed before clusters would overlap, connecting parallel wires. This was eventually found the be the limitation of the PMMA aperture method, discussed further in §3.2.6. The narrowest wires where no significant overflowing was observed were 80 nm wide, so this was the starting point chosen for fabrication of multi-trench devices.

3.2.2 Preliminary Design

The initial design for a sidegated structure is shown in Figure 3.8 and consists of a long, narrow channel and two symmetrical gates. The large scale contacts (Figure 3.8(right)) were defined using photolithography and the small scale contacts (Figure

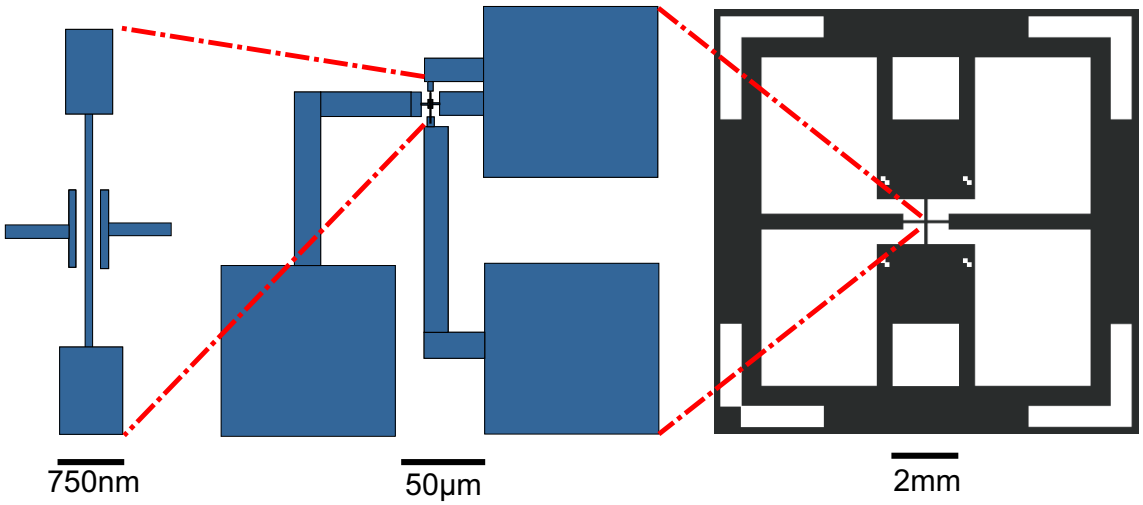

Figure 3.8: Initial sidegate design. (Left): Parts of circuit formed by PMMA aperture method consisting of two gates of 80 nm width with gate contacts and 150 nm wide 5 μm long channel. (Middle): Small scale contacts formed via EBL/thermal evaporation. (Right): Large scale contacts formed via photolithography/thermal evaporation.

3.8(middle)) were defined using electron-beam lithography. Both sets of gold contacts were deposited using thermal evaporation. A subsequent electron-beam write defines the channel and gate, which are to be deposited using the PMMA aperture method. The gate width was 150 nm and channel width was 80 nm. However, proximity effects from electron scattering make writing patterns using EBL more difficult if features are close to each other. To write any particular pattern, a series of dose tests are required. The question is: what would be the limitation of this technique, the writing resolution of the SEM or the PMMA aperture method itself?

Dose Tests

With a preliminary sample designed and confirmation that ultra-thin bismuth cluster wires in PMMA trenches were possible, the correct settings and method were required to write the initial sidegate pattern (Figure 3.8) using EBL. The FE-SEM was set up to write the pattern shown in Figure 3.8 using several different area and line dose combinations. Results are shown in Figure 3.9.

For a small line and area dose of 90 μC/cm and 90 μC/cm^2 respectively (Figure 3.9(a)), the gates were partially formed, but the gate contacts were not formed. When the doses were increased to 150 μC/cm and 150 μC/cm^2 (Figure 3.9(b)), a similar effect occurred and there was a more noticeable proximity effect at the center of the gates. This resulted from the area dose being too large. Figure 3.9(c) shows an increased line dose to 500 μC/cm, with area dose of 150 μC/cm^2. The pattern was defined more accurately, however proximity effects caused the gates to connect to the channel. Figure 3.9(d) shows sample 4 with area and line doses of area

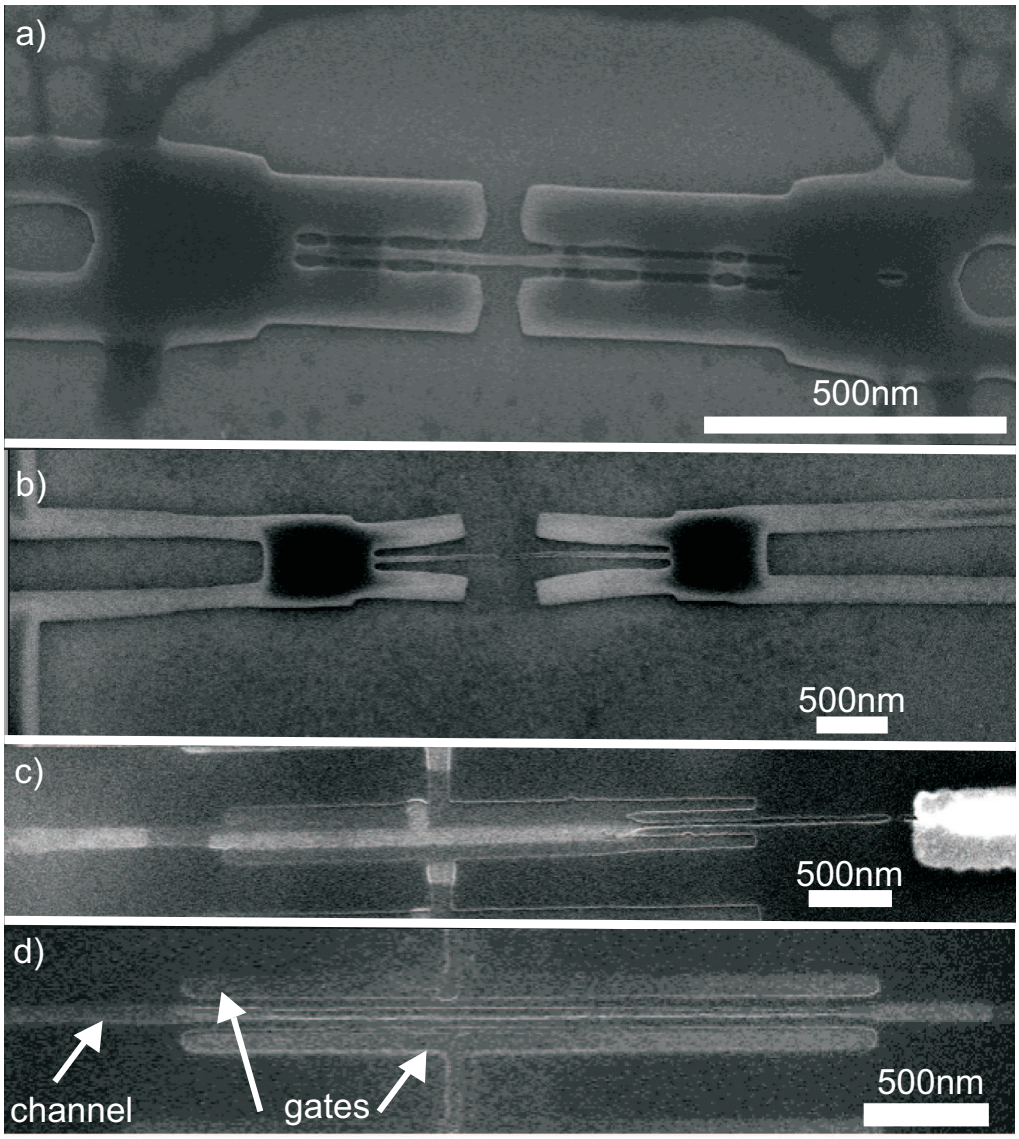

Figure 3.9: Sidegate dose tests (all with development time of 60 seconds) (a): Sample 1 with area dose 90 μC/cm^2 and line dose 90 μC/cm. (b): Sample 2 with area dose 150 μC/cm^2 and line dose 150 μC/cm. (c): Sample 3 with area dose 200 μC/cm^2 and line dose 500 μC/cm. (d): Sample 4 with area dose 120 μC/cm^2 and line dose 500 μC/cm.

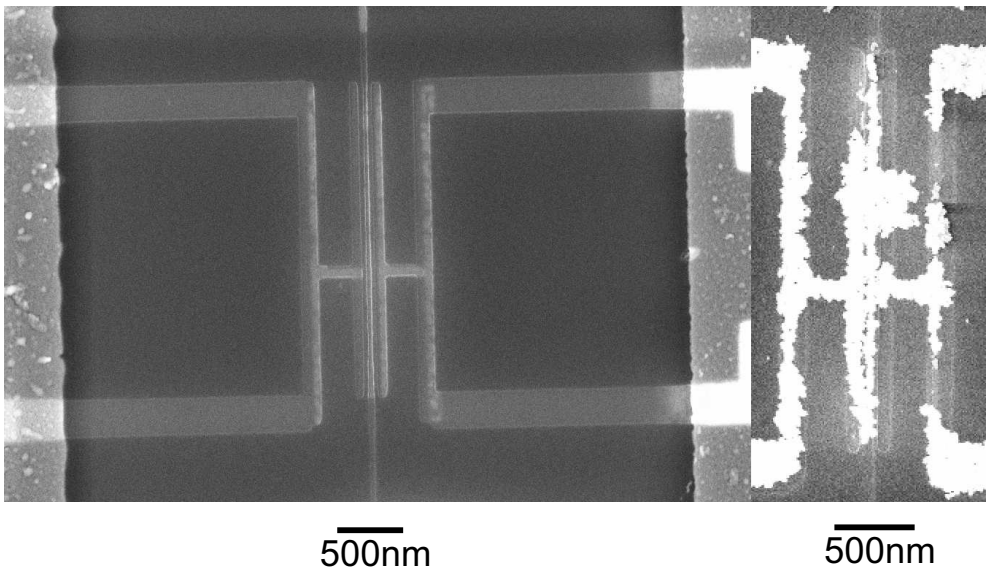

Figure 3.10: FE-SEM images of Left: Correctly exposed and developed sidegate PMMA pattern. Right: Sidegate pattern with identical exposure settings after cluster deposition with 180 sccm of argon and 4Å/s deposition rate for 55 minutes.

dose 120 μC/cm^2 and line dose 500 μC/cm. In this case, the gates and channel were clearly defined and properly developed. These settings were used to create all subsequent sidegate samples.

3.2.3 Preliminary Samples: Deposition Results

With the dose tests complete, two gates and a channel could then be formed in PMMA with sub-100 nm gaps between each. The gates and channels were connected to small-scale electrical contacts and cluster depositions could be performed. When no onset of conduction was observed, the substrate was inspected under the SEM. A typical result is shown in Figure 3.10(right).

Figure 3.10(right) shows that neither the channel or the gates formed correctly. Clusters deposited in the channel are physically connected to clusters deposited in the gate. This is partially caused by the 5 μm length of the channel, considerably longer than the 800 nm long samples from Figure 3.6. The extra length of the channel means the amount of material deposited for onset of conduction is increased. It was clear the sample design required modification to resolve the issues of gate-channel connection.

3.2.4 Redesigning the Sidegate Pattern

The sidegate pattern was redesigned by decreasing the length of the wires and increasing the gap between the channel and gate in order to remove overflowing effects.

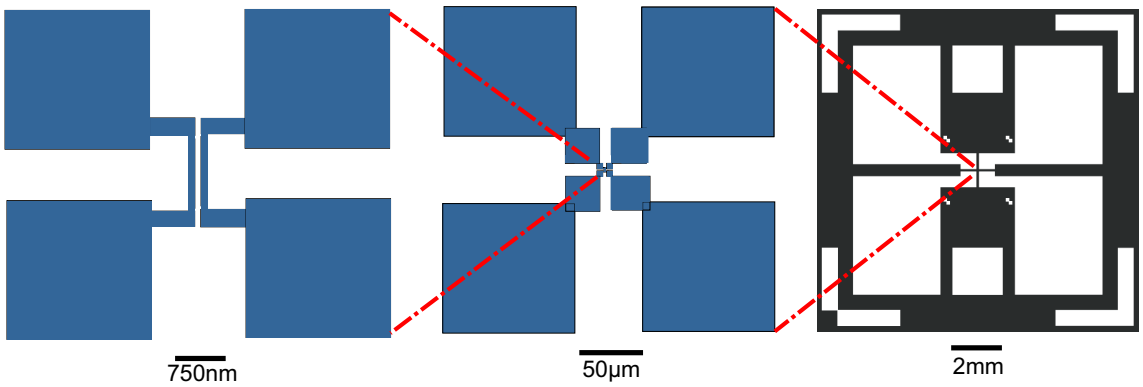

Figure 3.11: Sidegate Sample design. (Left): Parts of circuit formed by PMMA aperture method consisting of two contacted 200 nm wide wires a distance of 200 nm apart. (Middle): Small scale contacts also formed via PMMA aperture method. (Right): Large scale contacts formed via photolithography/thermal evaporation.

To achieve this, one gate was removed altogether. This design also allowed the conduction of both the gate and channel to be monitored during cluster deposition. The final design is shown in Figure 3.11. Each of the corners of the pattern in Figure 3.11(middle) is connected to the large scale photolithographically-defined contacts shown in Figure 3.11(right). Both the small scale contact (Figure 3.11(middle)) and the gate and channel (Figure 3.11(left)) are designed to be written using a single EBL process. The advantages of a single write include avoiding any tricky realignment issues and decreasing the production time of samples. The writing time of an individual sample using EBL was less than ten minutes.

Initially, the new sample pattern was created using relatively large dimensions to demonstrate this sample design would work in principle; the gate distance and wire widths were both chosen as 200 nm. This was easily achieved using the methods above[5]. Using such a large wire separation distances, both proximity effects and clusters exceeding trench dimensions posed less of a problem. The wire width and separation were easily modifiable using Wavemaker or the built in editor of the Raith EBL system.

3.2.5 Sidegate Circuit Setup

Different circuits were required to measure onset of conduction or "transistor mode" operation. These setups are now explained.

The same equipment used for electrical measurements as described in §2.4.1 was used for these circuits. For onset of conduction detection, the circuit in Figure 3.12(top) was used. (This circuit was two copies of the onset circuit for a two-

[5]Samples were prepared using identical settings from the previous design; area dose 120 μC/cm^2 and line dose 500 μC/cm.

point wire.) A constant source-drain voltage (typically 50 mV) was held across the contacts and the potential difference and current were simultaneously monitored and recorded using LabView 7. The cluster deposition was stopped immediately when both onsets were detected.

The circuit was modified for transistor-mode operation. A schematic of this circuit is shown in Figure 3.12(bottom). One of the two wires was designated to be the gate. This was connected so that the entire gate was at X volts, where X was the output of the variable voltage supply. This voltage supply could be ramped as a sawtooth wave or be kept at a constant voltage. The other wire was designated to be the channel and held at a constant voltage with the current being monitored as a function of the gate bias. Both circuits were simultaneously monitored and recorded using LabView 7. The choice of wires for the gate or channel was arbitrary and could be switched at any stage.

3.2.6 Sidegate Sample Deposition Results

This subsection explains the deposition and onset of conduction results of sidegated samples. Results of gate measurement on sidegate samples are discussed in §3.3. The first sample where an onset of conduction was successfully measured was the first of the new samples, Sidegate Sample 1.

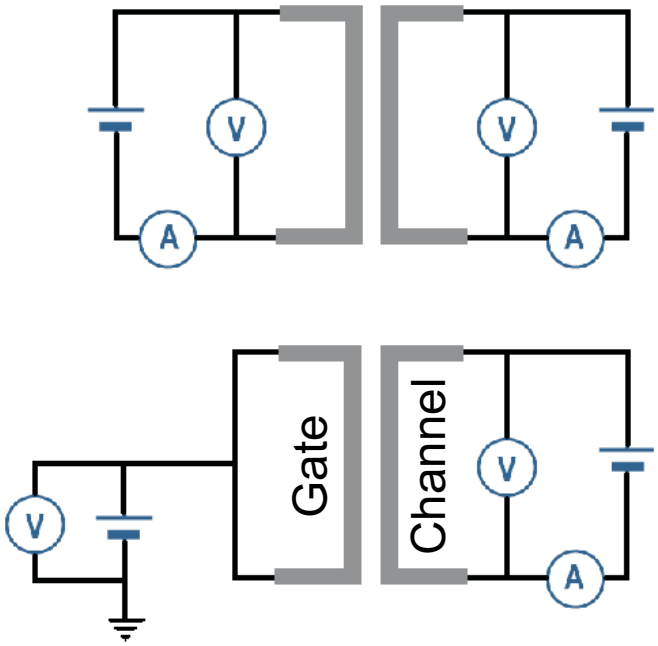

Figure 3.12: Schematic of circuits used for sidegate samples. (Top): Onset of conduction detection (Bottom): Transistor mode operation: Gate circuit (left), channel circuit(right).

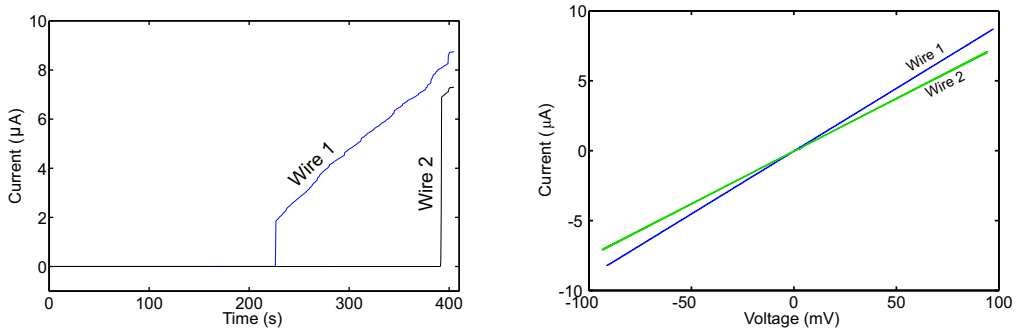

Figure 3.13: Sidegate Sample 1 (Left): onset of conduction of wire 1 and wire 2 occur at 230 s and 350 s respectively. Deposition details: Source temperature 815°C, argon flow rate 180 sccm, deposition rate 0.5Å/s. (Right): 100 mV current-voltage characteristics of both wires showing both wires are Ohmic with resistances of 11.5 kΩ and 13 kΩ for wire 1 and wire 2 respectively.

Sidegate Sample 1

The first of the new sample design, Sidegate Sample 1, shows an onset of conduction and current-voltage characteristics typical of other sidegated samples produced for this thesis. Sidegate Sample 1 consisted of two contacted nanowires of 200 nm diameter, positioned 200 nm apart. Figure 3.13 shows the onset of both wires and the current-voltage characteristics of both wires. The onset of wire 1 and wire 2 occurs at 230 s and 350 s respectively. Despite the 35% difference in onset times, the resistances of the wires are within 10% because both wires have the same writing pattern and the same coverage, so the resistances are closely matched. The reason both wires onset at different times is because the deposition of the clusters in the PMMA trench is a random process and the expected onset time of a PMMA aperture device has a large uncertainty [26].

Figure 3.13(right) shows the current-voltage characteristics of both wires of Sidegate Sample 1. Both wires are linear in the ±100 mV range with wire 1 and wire 2

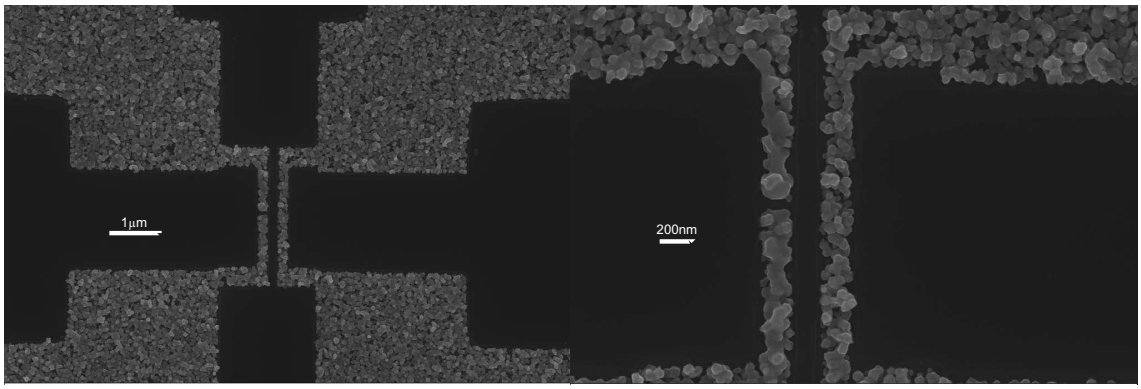

Figure 3.14: SEM Images of Sample 1. Deposition details: Source Temperature 815°C, argon flow rate 180 sccm, deposition rate 0.5Å/s. One wire shows partial melting due to Joule heating which occurred during an I(V) characterization process.

Wire width	Average thickness required for onset of both wires
100 nm	730 nm
200 nm	505 nm
300 nm	216 nm

Table 3.3: Average film thicknesses required for onset of conduction of both wires for Sidegate Samples for different wire widths.

having resistances of 11.5 kΩ and 13 kΩ respectively. The I(V) characteristics of all sidegate samples tested in this project were always linear over all measured voltage ranges. This voltage range encompasses the channel source-drain voltages[6] used in this chapter.

Sidegate Sample 1, shown in Figure 3.14, demonstrated that the new sample design was capable of producing parallel nanowires without a gate-channel connection. The fabrication of transistor structures had now been realized.

Wire Width versus Sample Thickness

There is no direct way to control the thickness of the sidegate samples. Because of the possibility of gate-channel connection, the deposition must be stopped as soon as both wires have formed. Hence there is no possibility to directly alter the film coverage. The film coverage can be indirectly controlled by changing the width of the gate/channel because a smaller width channel requires more material to be deposited to form a continuous wire. The average thicknesses for different wire widths for Sidegate Samples are shown in Table 3.3. The thickness values are far greater than a percolation sample (§2.3.3) which only required about 30 nm coverage to achieve an onset of conduction.

Sidegate Sample Spatial Variations

The process of forming two parallel nanowires from clusters had now been established. A summary of all depositions using the new sample design is shown in Table 3.4. The change in sample dimensions is now explained. The initial gate-channel separation and wire width of 200 nm worked but occasional problems occurred with gate-channel connections during deposition. When only one of the first ten samples samples showed a weak field effect[7], an attempt was made to reduce the dimensions of the devices to enhance the field effect. For samples 11-15, both the wire and the gate separation were reduced to 100 nm. It was found that the combination

[6] See Figure 3.12(top).

[7] The results of the gate measurements are described in the next section.

Sample	Wire Width	Wire Separation	Thickness Deposited	Details
1	200 nm	200 nm	135 nm	Annealing process caused discontinuous wire; No gate effect
2	200 nm	200 nm	1070 nm	Gate-channel connection formed during deposition
3	200 nm	200 nm	172 nm	Wire became discontinuous during measurements; No gate effect
4	200 nm	200 nm	585 nm	Gate-channel connection formed during deposition
5	200 nm	200 nm	670 nm	Wire became discontinuous during measurements; No gate effect
6	200 nm	200 nm	356 nm	Annealing process caused discontinuous wire; No gate effect
7	200 nm	200 nm	336 nm	No gate effect
8	200 nm	200 nm	1280 nm	No onset of conduction
9	200 nm	200 nm	186 nm	Gate effect observed
10	200 nm	200 nm	528 nm	Short between gate and channel
11	100 nm	100 nm	395 nm	Gate-channel connection formed during deposition
12	100 nm	100 nm	900 nm	Gate-channel connection formed during deposition
13	100 nm	100 nm	450 nm	Reduced deposition rate; No onset of conduction
14	100 nm	100 nm	856 nm	Annealing process caused discontinuous wire; No gate effect
15	100 nm	100 nm	-	No onset of conduction
16	200 nm	200 nm	1050 nm	Gate-channel connection formed during deposition
17	200 nm	100 nm	-	No onset of conduction
18	200 nm	100 nm	600 nm	Gate-channel connection formed during deposition
19	200 nm	100 nm	565 nm	Gate-channel connection formed during deposition
20	200 nm	100 nm	-	No onset of conduction
21	200 nm	100 nm	274 nm	Gate-channel connection formed during deposition
22	300 nm	200 nm	-	1 out of 2 wires onset of conduction
23	300 nm	200 nm	840 nm	Gate-channel connection formed during deposition
24	200 nm	200 nm	440 nm	Gate-channel connection formed during deposition
25	300 nm	200 nm	126 nm	No gate effect
26	300 nm	200 nm	132 nm	No gate effect
27	300 nm	200 nm	-	No onset of conduction
28	300 nm	200 nm	-	1 out of 2 wires onset of conduction
29	300 nm	200 nm	123 nm	Channel became discontinuous during measurements
30	300 nm	200 nm	-	1 out of 2 wires onset of conduction
31	300 nm	200 nm	132 nm	Both wires simultaneously died during measurements
32	300 nm	200 nm	310 nm	Gate-channel connection formed during deposition
33	300 nm	200 nm	-	Sample connector connection broke
34	300 nm	200 nm	250 nm	No Gate Effect
35	300 nm	200 nm	215 nm	Gate effect observed
36	300 nm	200 nm	164 nm	No Gate Effect
37	300 nm	200 nm	150 nm	Gate effect observed
38	300 nm	200 nm	120 nm	Investigated possible fractal conductance fluctuations; No gate effect
39	300 nm	200 nm	210 nm	Investigated possible fractal conductance fluctuations; No gate effect
40	300 nm	200 nm	210 nm	Investigated possible fractal conductance fluctuations; No gate effect

Table 3.4: Deposition details of Sidegate Samples showing variation in wire diameter, gate channel separation and associated thickness required for onset of conduction.

of a larger amount of deposited material required for onset of conduction and the physical separation of the gate and channel meant the gate and channel connected before both wires were able to form. The limitation of this method had been exceeded with these sample parameters. For samples 17-21, in order to reduce the amount of material required to measure an onset of conduction, the channel/gate wire width was then pegged back to have a wire diameter of 200 nm while maintaining the 100 nm wire separation. The cluster deposition rate was also decreased by a factor of ten, this was to ensure that the smallest amount of material possible was deposited after the onset of conduction. The trench overflow problem was not solved. For samples 25 onwards, in an attempt to completely remove the problem of gate-channel connections during deposition, the wire width was increased to 300 nm and the gate-channel separation was 200 nm. These sample parameters greatly reduced the number of samples where a gate-channel connection occurred. In fact, a gate-channel connection only occurred for only one sample with 300 nm wide wire width.

When an onset of conduction is observed, the deposition can be stopped within 5 seconds. For a deposition rate of 1 Å per second this would correspond to 0.5 nm additional thickness. This additional amount is unlikely to affect the probability of the parallel wires connecting. If no onset of conduction is observed, the deposition is allowed to continue for five times the expected onset time, to be certain there sufficient material has been deposited.

3.3 Sidegate Gate Measurements

This section describes the data from the three sidegated samples where a gate effect was observed. The data from each sample are discussed in §3.3.1, followed by SEM image analysis in §3.3.2 and then, finally, in §3.3.3 the results are compared to the EFE mechanisms of §3.1.4.

3.3.1 Bismuth Field Effects

With the PMMA aperture method modified and capable of producing a sidegated sample, field effect measurements were able to be performed. Three sidegate samples showed a small field effect, samples 9, 35 and 37. A different type of field effect was observed in each sample and all field effects were weak and inconclusive.

Sidegate Sample 9

The first sample where a gate effect was observed was Sidegate Sample 9. Sidegate Sample 9 had a gate-channel separation of 200 nm and wire diameter of 200 nm. Gate data is shown in Figure 3.15 and was obtained at 77 K. Figure 3.15(left) shows that a reversible increase in resistance occurs for gate bias values less than -13 V up to the minimum output of the power supply of -14.5 V. The positive gate bias run shows a similar reversible resistance increase at +13 to +14.5V (Figure 3.15(right)). The resistance increased for both positive and negative gate biases above |13 V| and changed by approximately the same magnitude of 0.1%. The change in resistance is of the same order of magnitude as a device with a similar dimensions from Table 3.2/[59].

When the gate bias is changed on a very small timescale a capacitive charging effect occurs (see §2.4.1), which explains the resistance spikes. These resistance

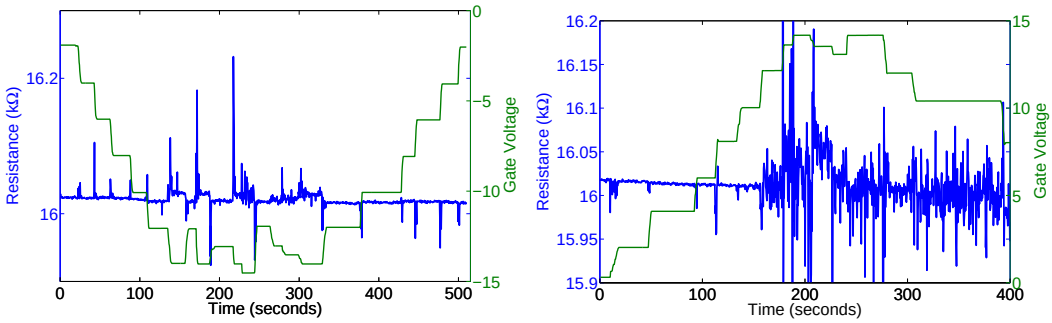

Figure 3.15: (Left): Sidegate Sample 9 gate run with negative gate bias. (Right): Sidegate Sample 9 gate run with positive gate bias. Gate bias ramped manually with channel offset = 50 mV and sample temperature = 77 K.

spikes are significantly larger in the regions for high gate biases, where the resistance increase is occurring. The resistance spikes are also directional; a resistance-increase spike for decreasing gate and a resistance-decrease spike for increasing gate bias.

Sidegate Sample 35

Figure 3.16 and Figure 3.17 show the gate-dependent change in resistance of the channel of Sidegate Sample 35 for four sample temperatures. It appears from Figure 3.16 that the curves above 11 K are completely flat meaning that no gate effect was observed. However, Figure 3.17 shows the same data presented in a different way using a normalized resistance scale. In this plot, both the up and down traces of the gate data are plotted separately to ensure the direction of the gate ramp or capacitive effects did not affect channel resistance. It should be noted the maximum gate bias has increased from Sidegate Sample 9. The change in channel resistance with temperature is behaviour which has been previously observed for bismuth cluster wires [29] and is shown in Figure 3.16 to demonstrate the sample has reached the minimum temperature at 11.2 K.

There is no visible gate effect (above noise) for any negative gate biases. However, for positive gate biases there is an apparent decrease in resistance of 0.05% when the sample is at 11 K. For other temperatures, the data appears to have a slight

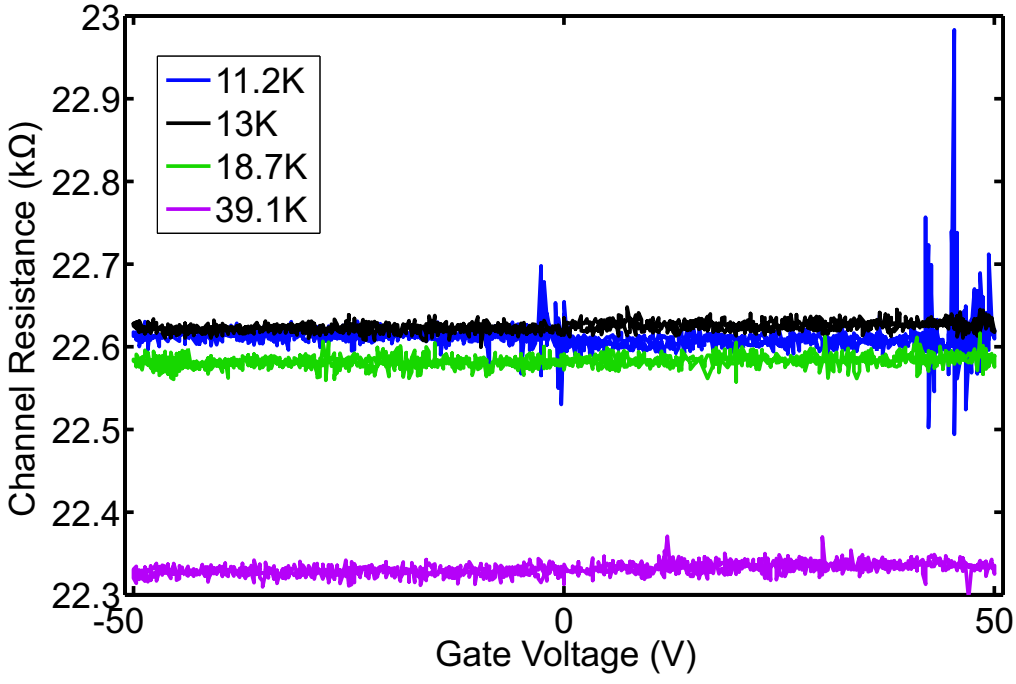

Figure 3.16: Sidegate Sample 35 gate bias data for 4 low-temperature gate runs. Gate bias ramped with LabView controlled power supply, temperature controlled with liquid helium and temperature controller. The offset was 50 mV.

trend of an increase in resistance for positive gate biases. The increase equates to a change in resistance of roughly 0.03% and therefore is only just observable above noise.

The channel was annealed and the gate runs were repeated. The wire was annealed via Joule heating, i.e. a relatively high current of 185 μA/4 mW was passed through the wire. A large resistor was put in series with the channel in order to avoid a current run-away effect. The circuit is shown in Figure 3.18(inset). The annealing process can affect the morphology of the wire (shown in §3.3.2). The annealing process decreased the 11 K resistance of the wire by 13% from 22.7 kΩ to 19.8 kΩ. When gate runs were performed after the annealing process, there appeared to be a slight resistance decrease in the 45-50 V range. The gate voltage range was then increased to $\pm$70 V in an attempt to enhance the features seen at +50V.

Figure 3.18 shows Sidegate Sample 35 at 11 K with the gate bias range increased to $\pm$70 V. Both the up and down ramps produce a decrease in resistance for gate voltages above 50 V. The resistance decrease did not occur when the sample was at temperatures of 18 K and above. The change in resistance at 11 K is of the order of 0.1%. The change in signal is greater than the noise level (0.02%) This resistance change, as well as the wire width and sample temperature are comparable with

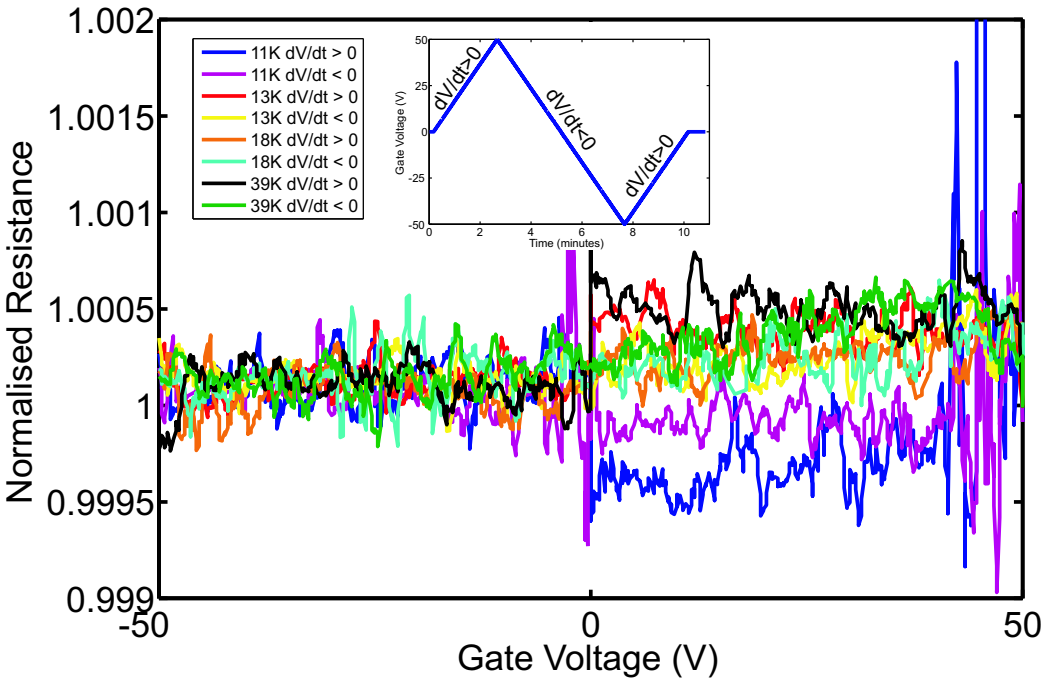

Figure 3.17: Normalized Sidegate Sample 35 gate bias data at four sample temperatures. Inset: Gate voltage variation with time. Gate bias ramped with LabView controlled power supply, temperature controlled with liquid helium and temperature controller. The offset was 50 mV. Same data from Figure 3.16 but data is normalized and split into up and down traces to ensure the direction of the gate ramp did not affect channel resistance.

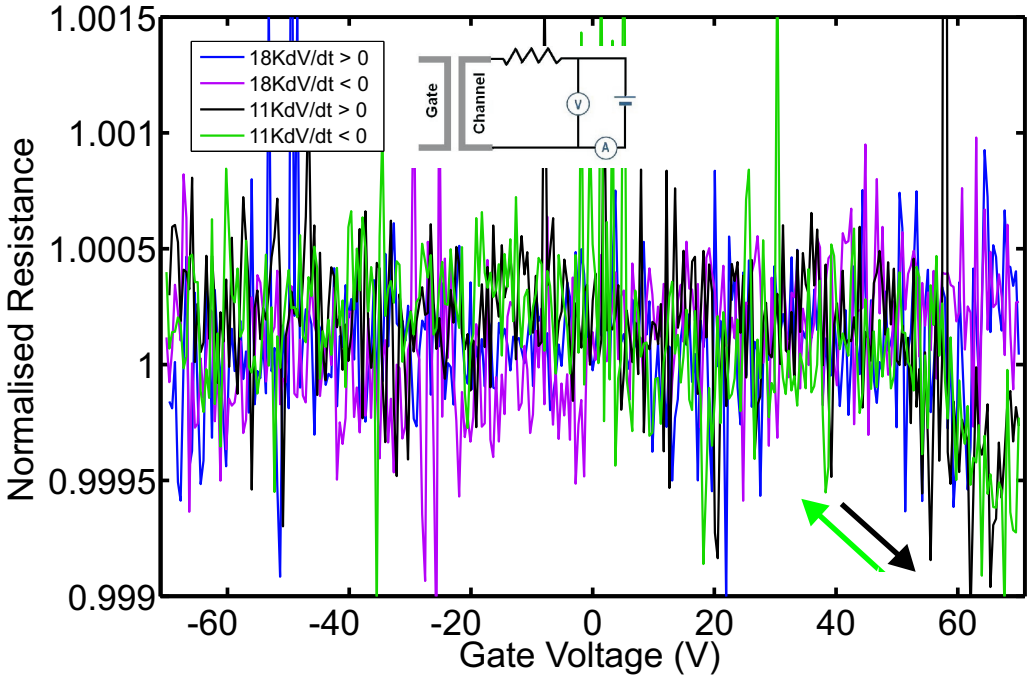

Figure 3.18: Normalized gate bias data from Sidegate Sample 35 after annealing process showing both 11 K and 18 K data. Inset: Circuit for annealing process, resistor = 100 kΩ.

Butenko [59] (see Table 3.2). The results from Butenko are now compared with Figures 3.16 and 3.18.

Butenko observed a linear increase of conductance in bismuth films with positive gate voltage of up to 30 V and a linear decrease (with a smaller gradient) for negative gate biases. The change in resistance was 0.2% at + 30 V gate bias and 0.1% at - 30 V and is shown in Figure 3.19. Although the sample parameters and magnitude of the resistance change are similar, the low temperature behaviour of the Butenko device

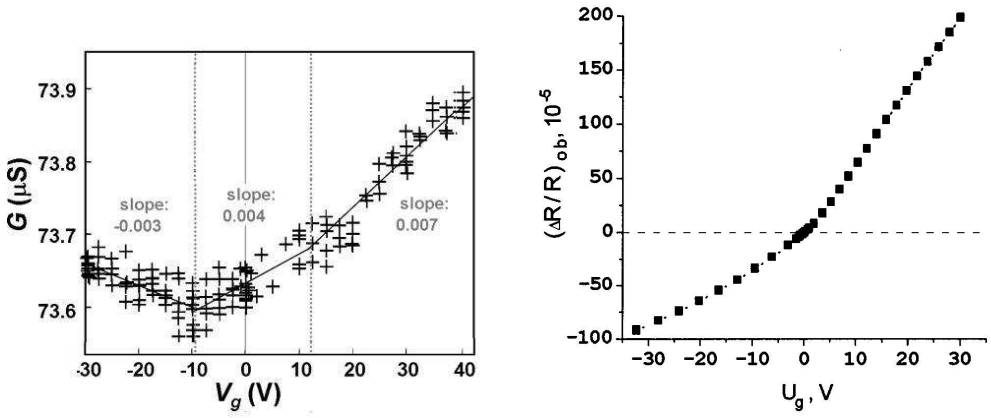

Figure 3.19: (Left): Gate effect in a 40 nm bismuth wire [60]. (Right): Gate effect in a 130 nm bismuth film at 15 K, from [59].

and Sidegate Sample 35 at ±70 V are quite different. Sidegate Sample 35 shows no electric-field effect until the device "turns on" at a gate bias of 50 V whereas the Butenko device shows an effect for the full ±30 V gate range. In addition, the resistance of the Butenko sample increases for positive gate biases, whereas a resistance decrease is observed for Sidegate Sample 35. However, data above 11 K shown in Figure 3.16 appear to show a slight linear increase in resistance as a function of gate voltage. This is an effect also observed in Sidegate Sample 37. The electric fields involved in Buteko are similar in magnitude to Sample 37, with a 100 V gate bias and 300 nm gate-channel separation the electric field strength of 3×10^8 V/m.

Sidegate Sample 37

Sidegate Sample 37 was fabricated identically to Sidegate Sample 35. Figure 3.20 shows the ±100 V 18 K gate run data for Sidegate Sample 37.

The reduced signal-to-noise ratio reveals a gradient in the data; the resistance increases slightly for a positive gate bias. The magnitude of the gradient in this data resembles the slope seen by Butenko [59] from Figure 3.19. However, the Butenko slope is ten times greater. A slope is visible at 12 K-22 K, but not at 41 K. The increase in signal with gate bias of 0.0004 is greater than the noise level of 0.0002.

A gradient was measured from each of the data sets and are plotted in Figure

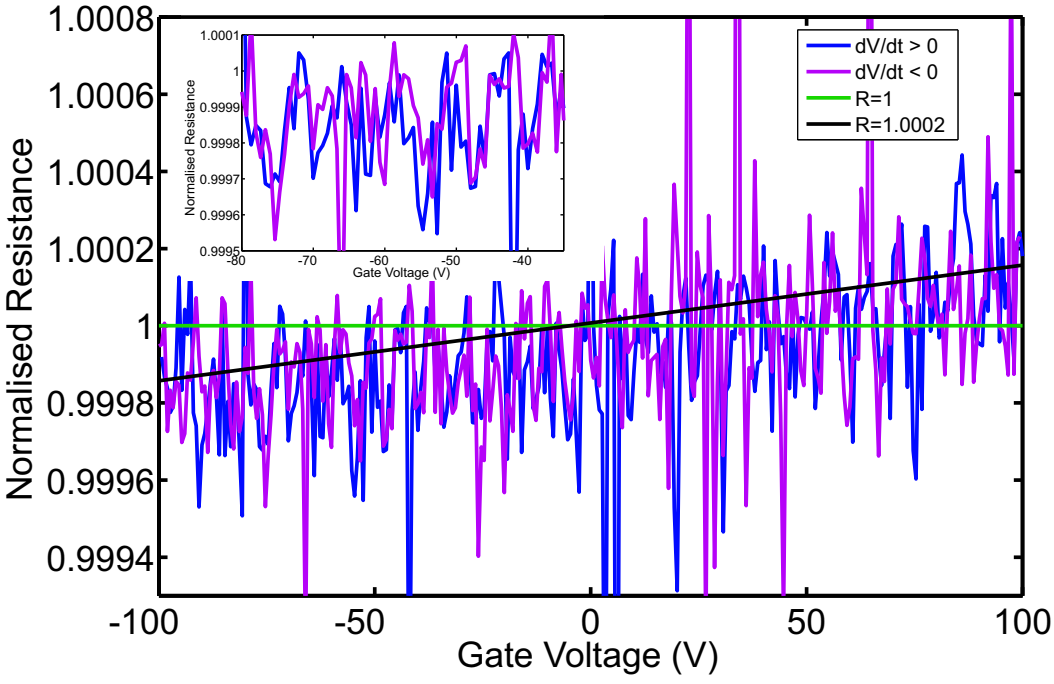

Figure 3.20: Normalized gate bias data of Sidegate Sample 37 gate run at 18 K. Also shown is a line used as a guide to the eye to show the slope and a line at R = 1 for comparison. Inset: Magnified section of main plot showing correlation of signal from both up and down traces.

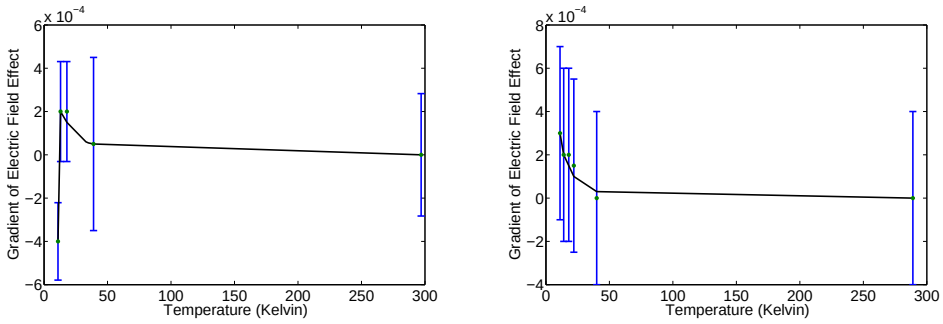

Figure 3.21: Temperature dependence of linear gate effect for (Left): Sidegate Sample 35 and (Right): Sidegate Sample 37. Each data point is extracted from plots of the same type as Figure 3.20. Variation in error bar size is based on number runs at each temperature.

3.21(right) with a slight temperature dependence observed. Because the noise is of the same order as the change in slope, the error bars are large and it is difficult to draw any strong conclusions from the data. However, the change in gradient is larger than the noise. Figure 3.21(right) shows that the gate-gradient is possibly affected by temperature and may increase significantly for even lower temperatures, which is consistent with the literature reporting the greatest field-effects at 2 K (not available at Canterbury).

Unlike Sidegate Sample 35, Sidegate Sample 37 did not show any turn-on resistance enhancement at large gate biases, even when the gate voltages were increased to ± 100 V. Another interesting feature of Sidegate Sample 37 is there appears to be an excellent correlation of the noise between the up and down gate traces (Figure 3.20(inset)). However, further investigation using high-resolution gate scans and gate runs with different periods (Samples 37-40), showed this effect to be an extrinsic time-dependent effect with a 12 second period. There was not time to remove or determine the origin of this noise source.

3.3.2 Sidegate SEM Image Analysis

FE-SEM images of Sidegate Samples 9, 35 and 37 are shown in Figure 3.22. Comparison of SEM images can potentially reveal why a small field effect was seen in some samples, but other samples showed no gate effect.

Effective Gate Distance

One feature that differentiates both Sidegate Sample 35 (Figure 3.22(middle)) and Sidegate Sample 9 (Figure 3.22(top)) from most previous sidegate samples is the slight overflowing of the gate, shown by Figure 3.22(arrows). In both cases, the overflow makes the minimum distance between the gate and the channel $\sim$60 nm.

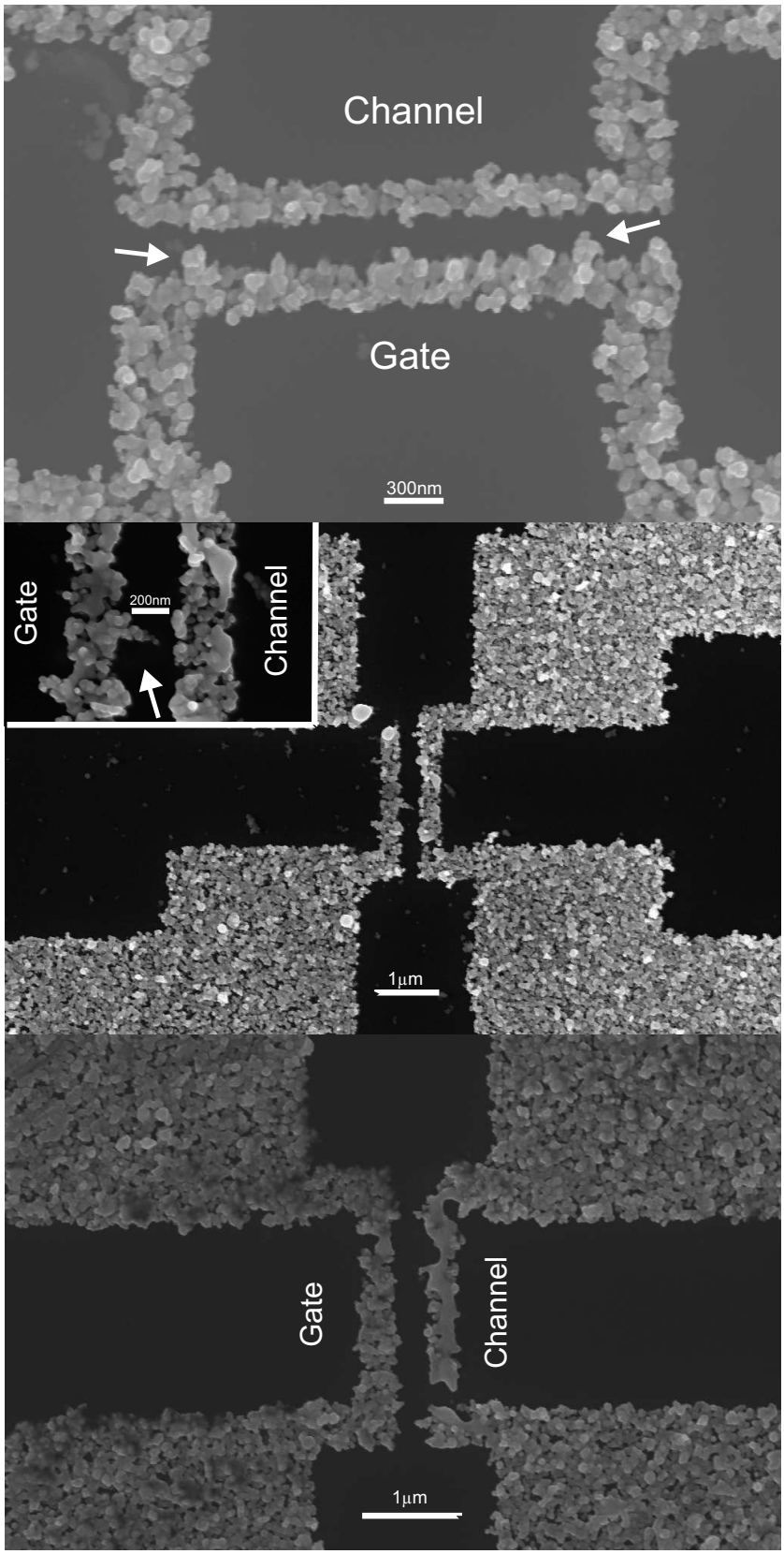

Figure 3.22: FE-SEM images of (Top): Sidegate Sample 9. (Middle): Sidegate Sample 35. (Bottom): Sidegate Sample 37. Sidegate Samples 9 and 35 show overflowing trenches on the gate, both reducing the minimum gate-channel distance to 60 nm. Sidegate Sample 37 shows an example of an annealing failure in the channel. Arrows indicate position of trench overflows.

In other samples this effect caused the gate-channel connection during deposition. It is interesting to note that the only two samples where a resistance turn-on was observed occurred when the gate had a trench overflow. The overflowing trench potentially affects the gate effect of the sample in two ways. Firstly, the physical separation of the gate and channel is smaller in these samples. Hence, the electric field produced for any gate bias is therefore greater. Secondly, the shape of the overflows are spiked which will enhance the electric field at that point.

Annealing/Breaking of Wires

The channels of both Sidegate Sample 35 (Figure 3.22(middle)) and Sidegate Sample 37 (Figure 3.22(bottom)) were annealed. The effects of the annealing process are visible in the channel of Sidegate Sample 35 as some clusters have melted and fused together. Figure 3.22(middle) shows the wire used as the gate is not continuous, this break occurred only after the gate experiments were completed.

The annealing process used on Sidegate Sample 37 exceeded the current limit for the channel which caused the wire to melt. This meant that no post-anneal measurements were possible. The current that caused the channel of Sidegate Sample 37 to become discontinuous was 160 μA. Although this is less current used for the successful annealing process of Sidegate Sample 35, the amount of material deposited on Sidegate Sample 37 is less: 150 nm for Sidegate Sample 37 compared to 215 nm for Sidegate Sample 35. For comparison, no annealing process was performed on Sidegate Sample 9 (Figure 3.22(top)).

3.3.3 Summary and Discussion

Magnitude of Electric Field Effects

The magnitude of electric field effects from §3.3.2 are summarized in Table 3.5. There are two types of gate effect observed in the sidegate cluster samples. The first is the so-called *linear gate effect* where the change of resistance is approximately linear with applied gate bias. The second is a *non-linear gate effect*, where a change in resistance is only observed for gate biases above a threshold gate bias.

Sidegate Sample	linear gate effect	non-linear gate effect
9	n/a	0.1%
35	0.03%	0.1%
37	0.05%	n/a

Table 3.5: Maximum magnitude of linear and non-linear gate effects observed in bismuth sidegate devices.

Sidegate Sample 37 appears to have a temperature-dependent electric field effect, having a linear gradient in the range of 11 K to 22 K, but not at 40 K. Butenko [59] also observed a linear decrease in gate effect from 15 K up to 77 K, shown in Figure 3.23. The decreasing gate effect for higher temperatures is consistent with the data for Sidegate Sample 35 and 37 (Figures 3.17 and 3.20).

What differentiates the non-linear gate effect observed in Sidegate Sample 9 is that it occurred at both positive and negative gate biases and the sample temperature was 77 K. The gate effect turn-on occurred at |13 V| for both positive and negative gate biases. There were no other cases of samples showing a similar effect for any positive voltages in the 10-15 V range and no others observed in the negative gate bias range or at 77 K.

Effects of Annealing

Because the devices studied in this project were fabricated from clusters, it was anticipated to be more difficult to observe a gate effect in comparison to thermally evaporated films. However, if the clusters are annealed, then the device becomes more uniform (a comparison of annealed and non-annealed cluster wires is shown in Figure 3.22). If the boundary between clusters or the clusters themselves have an effect on the gate dependence of the resistance, then a difference should be observable between an annealed wire and a non-annealed wire. Annealing wires is a difficult process, even with a large resistor in series there was still a very narrow range of currents that would anneal a wire without destroying it. The largest gate effect occurred in Sidegate Sample 35 for a gate bias of 70 V, when the device was at 11 K after it had been annealed. Unfortunately, when the annealing procedure was

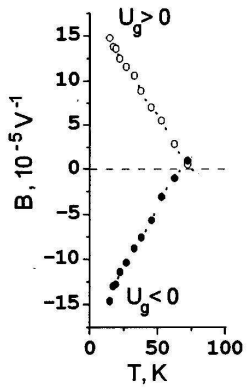

Figure 3.23: Temperature dependence of the magnitude of the linear gate effect observed by Butenko [59]. B=gate-dependent gradient, U_g=gate bias.

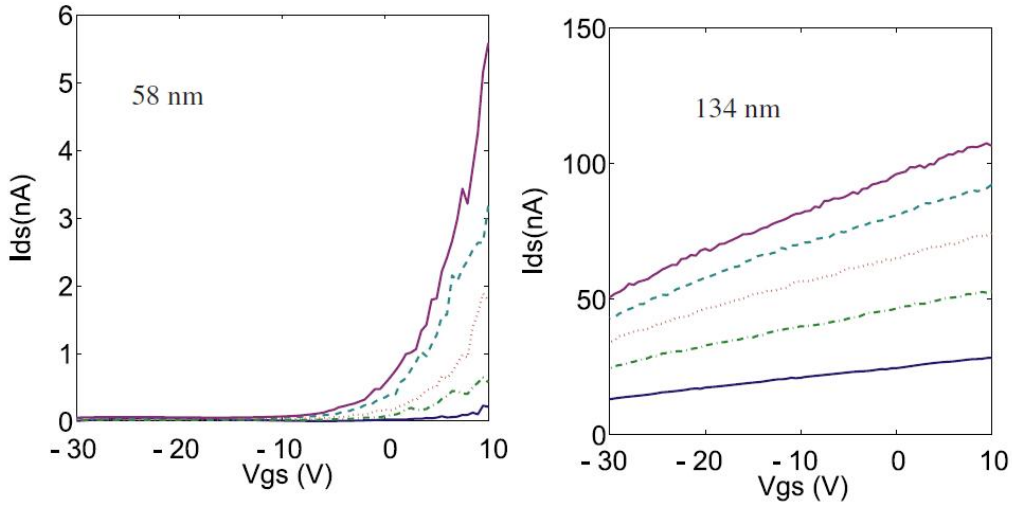

Figure 3.24: Change in transistor behaviour of tin oxide cluster nanowires, showing the difference between 52 nm wide and 134 nm wires for 5 different offset voltages [70].

performed on Sidegate Sample 37, the channel broke (see Figure 3.22 (bottom)), so it cannot be ascertained if the non-linear gate effect seen in Sidegate Sample 35 was repeatable across samples.

Comparison with Other Cluster Gated Devices

Figure 3.24 shows the room temperature field effect for tin oxide nanowires made at Canterbury [70]. A non-linear current enhancement is observed for 58 nm wide wire (Figure 3.24(left)), but a near-linear current enhancement for a 134 nm wire (Figure 3.24(right)). If nanowires made from bismuth have the same properties, then making the transition to thinner wires could significantly enhance any field effect. The thinner wires could also potentially undo a semimetal-to-semiconducting transition, could further enhance any gate effect.

Comparing the Models with the Results

Sample 9 showed a small non-linear gate effect with approximately the same magnitude for both positive and negative gate biases. The gate bias required to deplete charge carriers for Sidegate Sample 9 was |13V|. The resistance spikes seen in Figure 3.15 are consistent with capacitive charging, which is compatible with the mechanism from Model 1 as the sign of the resistance spikes always matched the direction of the gate bias ramp.

Sidegate Sample 35 showed a non-linear gate effect at low temperature and for high positive gate bias. The non-linear effects can be explained in terms of a barrier which is overcome. The gate effect implies the barrier overcome is for electrons and

therefore this behaviour is qualitatively consistent with Model 2. The gate bias required to overcome the barrier for Sidegate Sample 35 was 50 V. Gate bias values below 50 V do not provide sufficient energy for electrons to overcome this barrier. It is possible this barrier height is reduced by annealing the channel and that additional annealing would further enhance the gate effect.

Sidegate Samples 35 and 37 showed a weak linear gate effect. The linear gate effects observed can be explained, at least qualitatively, in terms of model 3. Model 3 suggests that holes are the dominant charge carriers. If holes are dominant, an increase in resistance is expected for positive gate voltages and decrease in resistance for negative gate voltages.

An effective doping level can be calculated from the magnitude of the gate effect and Model 1. It follows from the definition of conductivity (Equation 4.3) that the percentage change in resistance is the percentage change in carrier concentration. If it is assumed that at 2 K we have $5\times10^{17}\text{cm}^{-3}$ carriers [65], then the change in carrier concentration caused by a 100 V gate bias is $5\times10^{14}\text{cm}^{-3}$. Hence the effective doping level at 100 V for sample 37 (Equation 3.1) is $5\times10^{14}\text{cm}^{-3}$.

Overall, there is insufficient detail in the data to accurately identify the nature of any field effect in the bismuth sidegate structures in this study. Therefore, no firm conclusions can be made about the gate effects observed in bismuth sidegated devices.

3.4 Conclusion

In this chapter the limitations of the PMMA aperture method were investigated and then used to explore the possibility of observing a field effect in bismuth cluster devices. Initially, the Raith 150 EBL system was used to produce three parallel PMMA trenches of 80 nm width and sub-100 nm pitch. Parallel bismuth nanowires of 300 nm diameter were deposited 200 nm apart without any connection occurring during cluster deposition. Although these dimensions are not as small as those from Table 3.2, the fabrication of nanoscale bismuth cluster devices with sidegates using the PMMA aperture method was a success.

The gate effects observed in the sidegate structures were weak and inconclusive. A small gate effect up to 0.1% was observed in some devices, but other devices with the same sample dimensions showed no gate effect. It would appear that the temperatures and wire dimensions are just above the range where a consistent observable gate effect is possible. The limitation of the PMMA aperture method to produce bismuth devices with a significant gate effect is the tendency of clusters to be deposited outside the boundary of the PMMA trenches meaning it is not possible

to produce very thin wires or obtain very small gate-channel separation.

The experimental set up could be improved in several ways. If the small-scale contacts (Figure 3.11(middle)) were gold rather than clusters, then a greater percentage of the resistance of the device would be the channel as the methods used in this chapter measure the resistance of the small-scale contacts as well. Gold small-scale contacts would require an additional lithography and lift-off process. This style of sample is certainly achievable using the methods in this thesis, but was not attempted due to alignment difficulties and time constraints.

Decreasing the sample temperature should theoretically increase the gate effect. With the current cryostat, 11 K is the lower limit of device temperature available. A new bath-style cryostat is on order, which should allow for a lower device temperature.

Using smaller diameter bismuth clusters should reduce the magnitude of the overflowing effect and enable a smaller channel-gate separation. This process would have to allow for smaller clusters having a higher tendency to be deposited on PMMA [26]. The current bismuth source produces a very consistent $\sim$30 nm cluster diameter, so source modifications would be required. It is also possible smaller clusters could create thinner bismuth wires and this could induce the bismuth semimetal to semiconductor transition from §3.1.1.

Chapter 4

Preparation of Germanium Cluster Devices

The previous chapter evaluated the possibility of observing electric-field effect behaviour in devices made from semimetallic atomic clusters. This chapter continues the investigation into transistor behaviour of cluster devices by fabricating cluster structures made from a semiconducting material: germanium. In order to achieve this, a source of germanium clusters was required.

This chapter describes the development of a germanium cluster source and investigates the properties of films of germanium clusters in vacuum. To begin, §4.1 contains a review of the properties of germanium and the relevant literature. §4.2 discusses the redesign of the cluster source and the subsequent source characterization. §4.3-4.4 describe the electrical characterization of percolating films of germanium clusters. Finally, in §4.6 results are summarized and conclusions drawn.

4.1 Properties of Germanium

This section contains a of review of the general and electrical properties of germanium, comparison of germanium and silicon, a review of semiconductor/metal interfaces and finally a review of germanium thin films, nanowires and nanoparticles.

4.1.1 Germanium: History and General Properties

Germanium (Ge) is an elemental semiconductor with atomic number 32 [40]. It was first chemically isolated in 1886 [71], but only received limited research interest for the next 40 years because of its perceived lack of interesting qualities and its rarity/high-price [72]. By the 1940s, the main uses for germanium were as rectifiers

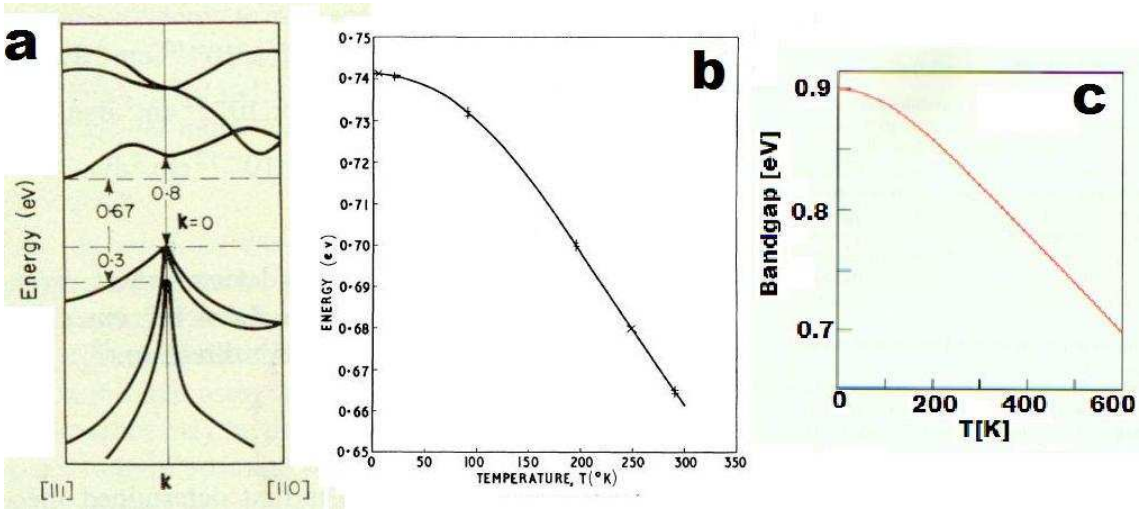

Figure 4.1: Germanium band gap information; (a) Band structure at 300 K showing the indirect gap of 0.67 eV in the <111> direction and the direct gap of 0.8 eV [76]. (b) Variation of the indirect band gap with temperature shows a range of 0.67 eV at 300 K to 0.71 eV at 0 K [43]. (c) Variation of the direct band gap with temperature shows a range of 0.7 eV at 600 K to 0.9 eV at 0 K [77].

and photodiodes [2]. This changed in 1947 with germanium used in the development of the first transistor [73]. Germanium was used for two decades in commercial transistors before being replaced by silicon, which is still used today[1].

Germanium has a melting point of 937°C, a density of 5.32674 g/cm^3 at 298 K [74] and has a bulk diamond structure with a lattice parameter of 5.65754 Å [75]. The band gap of germanium is 0.67 eV at 300 K and 0.71 eV at 0 K [76]. The band structure of germanium [43] and the variation of the indirect [76] and direct [77] gaps with temperature are shown in Figure 4.1. Figure 4.1(b)&(c) show how the indirect and direct band gaps vary from 0 K to higher temperatures. The band gap is partially determined by the lattice constant [78]. The decrease in band gap for higher temperatures is due to the thermal expansion of the lattice and increased lattice vibrations.

The drift mobility is derived from considering the force on charge-carriers due to the electric field from an applied voltage and solving Newton's second law of motion, giving [79]:

$$\mathbf{v}_d = \mu_x \mathbf{E} \tag{4.1}$$

where $\mathbf{v}_d$ = drift velocity, $\mathbf{E}$ = electric field, μ_x = mobility where x represents either electrons or holes. The mobility of germanium at 300 K is 1900±50 cm^{2}V^{-1}s^{-1} and 3900±100 cm^{2}V^{-1}s^{-1} for holes and electrons respectively [80]. Mobility can be

[1]See §4.1.2 for a germanium/silicon comparison.

Property	Germanium	Silicon
Band gap at 300 K	0.66 eV	1.12 eV
Band gap type	Indirect	Indirect
Mobility (electrons)	3900 $cm^2V^{-1}s$	1500 $cm^2V^{-1}s$
Mobility (holes)	1900 $cm^2V^{-1}s$	450 $cm^2V^{-1}s$
Intrinsic Carrier Concentration	$2.4\times10^{13}cm^{-3}$	$1.45\times10^{10}cm^{-3}$
Intrinsic Resistivity	47 Ωcm	2.3×10^{-5} Ωcm
Electron effective mass	m_l=1.64m_0	m_l=0.98m_0
	m_t=0.082m_0	m_t=0.19m_0
Hole effective mass	m_l=0.044m_0	m_l=0.16m_0
	m_h=0.28m_0	m_h=0.49m_0

Table 4.1: Properties of germanium and silicon, taken from Sze [2]. m_0 = rest mass of electron, m_l = mass in longitudinal direction, m_t = mass in transverse direction.

related as the carrier lifetime, τ:

$$\mu_x = \frac{e}{\tau m_x} \tag{4.2}$$

where m_x is the mass of the charge carrier and e = electronic charge. The carrier lifetime is a useful parameter in assessing the frequency responses of diodes and transistors. The maximum transistor frequency response is determined by the current of minority carriers [2]. Mobility is related to the conductivity via Ohm's law (see [78] for derivation) for electrons and holes:

$$\sigma = e(n_e\mu_e + n_h\mu_h) \tag{4.3}$$

This equation is important for relating the carrier concentration to the electrical resistance.

4.1.2 Germanium versus Silicon

Silicon replaced germanium as the device material for consumer electronics in the 1960s. A practical reason for the change was the maximum operating temperatures of devices based on germanium is ∼80°C (compared to ∼160°C for silicon). Above these temperatures any differences in conduction between n and p type germanium become negligible, so transistors and diodes no longer function. Although most consumer devices operate at room temperature, dissipating the heat generated from a device is a major design issue [81]. This temperature dependence, combined with a more stable oxide (see §5.1.1) and the previously unavailable purifying technique of zone refining [82] allowed silicon to become the semiconductor of choice for virtually all consumer electronic devices and it remains so today. Selected properties of both

germanium and silicon are listed in Table 4.1. Each of the properties are related to device performance and are discussed below.

Both germanium and silicon have an indirect band gap; this means any devices using optical absorption properties will be less efficient than those made with a direct band gap material. The band gap of germanium is roughly half of that of silicon. The consequences for devices are that germanium can absorb photons further in the infrared range whereas silicon can only absorb photons with energy above 1.1 eV. However, the smaller band gap contributes to the lower device operating temperatures discussed above. The distinctive properties of both germanium and silicon lead to devices tailored to their specific properties.

4.1.3 Germanium: Electrical Properties

The resistivity of bulk germanium is $\sim$40 Ωcm which corresponds to a room temperature carrier concentration of $\sim 10^{13}\text{cm}^{-3}$ [43]. This carrier concentration provides the *intrinsic* conductivity for germanium, that is charge carriers originating from band gap excitation[2]. For all semiconductors, the resistivity of germanium can be decreased by adding dopants to the crystal, which provide the *extrinsic* conductivity of the germanium crystals. Germanium is in group IV of the periodic table so dopants are commonly added from group III or group V to make p-type or n-type samples respectively. These dopants are commonly aluminium or antinomy and have typically produced carrier concentrations up to 10^{19}cm^{-3} [83]. Different concentrations of dopants affect how the resistivity changes with temperature. This is illustrated in Figure 4.2(right), which shows the resistivity variation with temperature of 18 samples of n-type germanium doped with various amounts of antimony. The impurity concentrations range from $5.3\times10^{14}\text{cm}^{-3}$ for sample 1 to $9.5\times10^{17}\text{cm}^{-3}$ for sample 29 [84].

The resistivity behaviour can be described by three conduction regimes. Regime 1: high temperatures where T>200 K. Regime 2: (12 K-20 K <T< 200 K). Regime 3: low temperatures (value of T<12 K - 20 K). Each regime is now described.

Resistivity at high temperatures is described by regime 1 where intrinsic conduction provides the majority of charge carriers. Conductivity in this temperature range is dominated by charge carriers with enough thermal energy to overcome the band gap. Although the band gap is much greater than the thermal energy, a few charge carriers are able to conduct. This intrinsic behaviour is described by $n =$ number of carriers [78]:

$$n = \sqrt{N_c N_v} e^{\frac{-E_g}{2k_b T}} \tag{4.4}$$

[2]The carrier concentration is related to the conductivity by Equation 4.3.

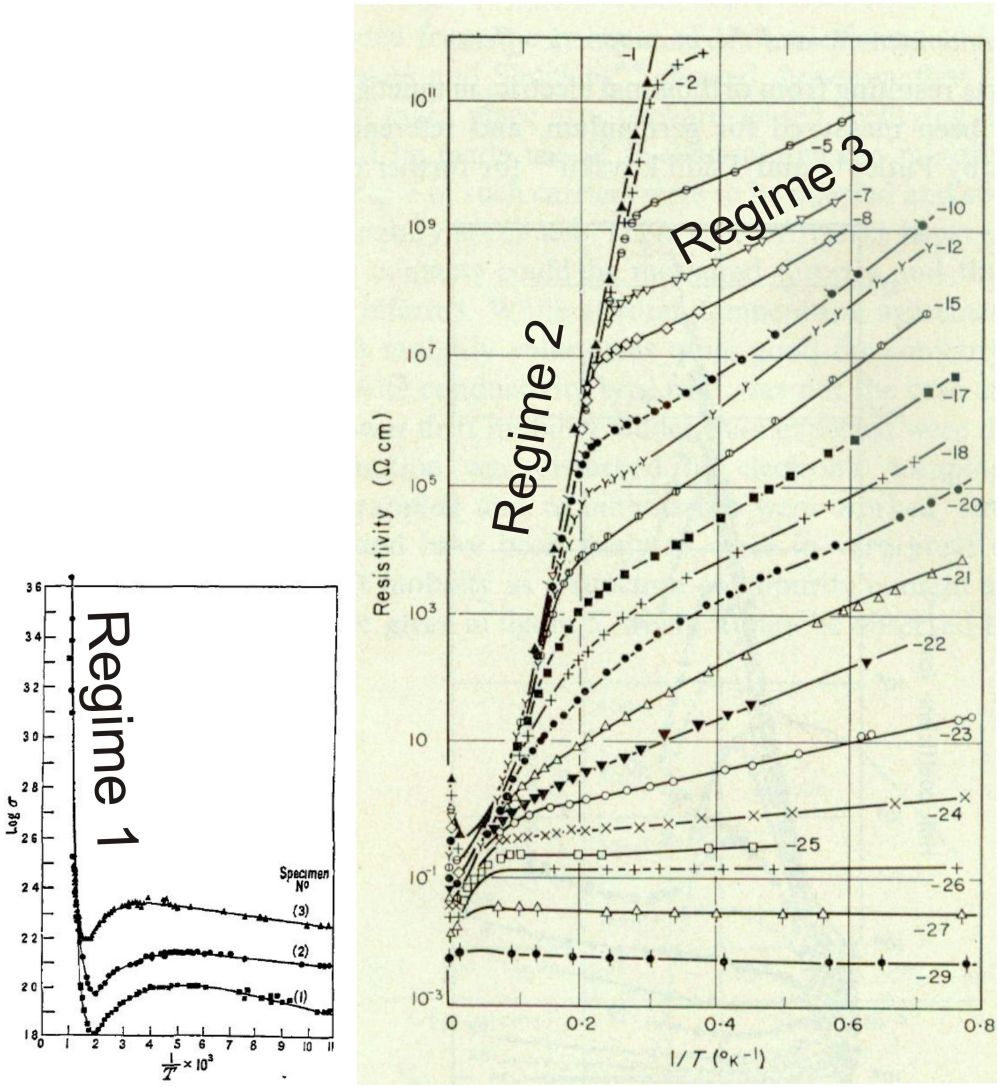

Figure 4.2: (Left): Conductivity as a function of inverse temperature over a higher temperature range [85].(Right): Bulk n-type germanium temperature-dependent data for 18 samples of various antimony concentrations. Impurity concentrations vary from $5.3\times10^{14}\text{cm}^{-3}$ for sample 1 to $9.5\times10^{17}\text{cm}^{-3}$ for sample 29 [84].

where N_c = carrier concentration of conduction band, N_v = carrier concentration of valence band, E_g = band gap, k_b = Boltzmann constant, T = temperature. In this regime all samples have the same gradient on the $\log(\sigma)$ versus 1/T plot independent of impurity level, as shown in Figure 4.2(left). This phenomenon is commonly exploited to determine the band gap by plotting the natural log of the resistivity against inverse temperature and using Equation 4.4. Although the intrinsic conduction contributes charge carriers for all non-zero temperatures, as the temperature decreases conduction becomes dominated by dopants and a transition to regime 2 occurs.

Regime 2 is for mid-range temperatures, typically in the range of 20-200 K , where extrinsic conduction dominates; the impurities in the sample provide the majority of

Group III	Boron	Aluminium	Gallium	Thallium	Indium
	0.0104 eV	0.0102 eV	0.0108 eV	0.01 eV	0.0112 eV
Group V		Phosphorous	Arsenic	Antimony	
		-0.0120 eV	-0.0127 eV	-0.0096 eV	

Table 4.2: Ionization levels of impurities in bulk germanium. Data taken from Hogarth [43].

charge carriers. The binding energy of donors and acceptors is less than the thermal energy for this regime, hence (essentially) all of the impurities are ionized for this entire regime. (See Table 4.2 for levels of impurity binding levels for germanium).

The samples with higher impurity levels have lower resistivity simply because of a larger number of charge carriers available for conduction. The temperature that the transition from regime 1 to 2 is observed is affected. The transition occurs at the critical temperature where both intrinsic and extrinsic charge carriers equally contribute to the conductivity. This must occur at higher temperatures for samples with higher levels of extrinsic carriers. The transition temperature is another tool in the characterization of semiconductors.

Because the carrier concentration is almost constant in this regime, any changes in resistivity are due to mobility changes [69]. Depending on if the sample is n or p-type, the conductivities are [83]:

$$\sigma_h = en_h\mu_h \tag{4.5}$$

$$\sigma_e = en_e\mu_e \tag{4.6}$$

Hence, the changes in mobility linearly affect the conductivity. As can be seen in Figure 4.2(b), samples with low levels of doping have the most dramatic resistivity increase in this regime. Samples with very high levels of doping, such as Samples 25-29, show degeneracy over the entire temperature range and still have low resistivity, even at 4 K. This means that the devices with the highest impurity levels behave as in regime 2, even for low temperatures.

Regime 3 is when temperatures are below 20 K and where resistivity increases. This region is the carrier freeze-out, when the thermal energy is no longer sufficient to excite all impurity carriers for conduction. A similar physical process occurs as in regime 1. The resistivity obeys a Boltzmann distribution [84]:

$$\rho = Ce^{-\frac{\epsilon_3}{kT}} \tag{4.7}$$

where ϵ_3 is the activation energy of impurity conduction and C is temperature-independent factor which depends on the level of doping. Regime 3 is where infor-

mation about the ionization levels of impurities in germanium can be determined by solving Equation 4.7 for ϵ_3.

4.1.4 Germanium Contact Issues

Many of the properties of semiconductor devices are determined by their interaction with an electrical contact or by surface states induced on the semiconductor surface. These are discussed for the case of a general semiconductor.

When a metal and semiconductor are brought into contact, charge carriers will move between materials because the Fermi levels are mismatched. An electric field is created by charges at the surface of both the metal and semiconductor. As a consequence, band bending must occur at close proximity to the interface. The electric field penetration in a metal is typically less than 0.1 nm [86], compared to 10-1000 nm for germanium (with doping of 10^{14}-10^{18}cm^{-3} respectively [2]). This means the charges in the semiconductor are affected much more and this creates a so-called depletion region.

Ohmic versus non-Ohmic Contacts for Semiconductors

When a semiconductor and a metal have a junction and are in thermal equilibrium, the resulting contact can be either Ohmic or non-Ohmic. The barrier between the metal and semiconductor depends on the relative positions of the Fermi levels [86]. Four cases are discussed from Figure 4.3. The symbols for Figure 4.3 are E = energy, E_c = conduction band, E_v = valence band, E_F = Fermi level, Φ_B = barrier height. If the Fermi level of an n-type semiconductor is higher than that of the metal, then electrons will flow into the metal creating a depletion layer in the semiconductor. The bands will bend up as shown in Figure 4.3(a). If this is the case, a Schottky barrier is created, so the junction is non-Ohmic. However, if the Fermi level of the metal is less than the Fermi level of the n-type semiconductor, then electrons transfer into the semiconductor from the metal, the bands bend down, creating an accumulation of electrons, shown in Figure 4.3(b). Because electrons can pass the interface without a barrier, the contacts are Ohmic.

If the Fermi level of the metal is greater than the Fermi level of the p -type semiconductor, then electrons flow from the metal to the semiconductor creating a depletion zone in the semiconductor. The bands bend down, creating a Schottky barrier as shown in Figure 4.3(c). If the semiconductor is p-type, and the Fermi level of the semiconductor is greater than the Fermi level of the metal, then electrons will flow into the metal and create a hole accumulation layer. This causes the bands to bend up as shown in Figure 4.3(d). The case of the non-Ohmic contacts are now

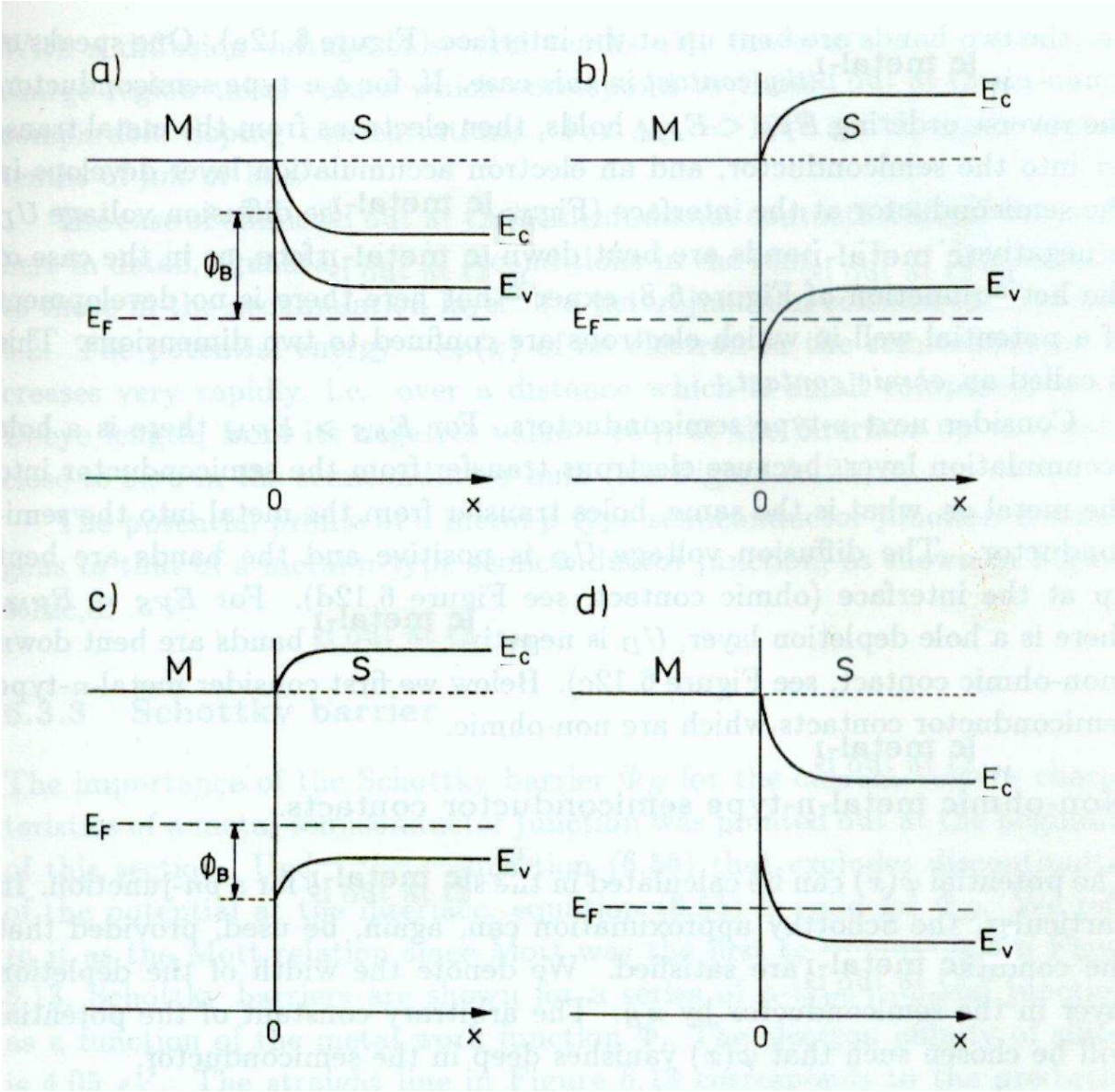

Figure 4.3: Relative Fermi levels determining barrier-type of a metal and semiconductor interface [86]. (a) n-type non-Ohmic contacts. (b) n-type Ohmic contacts. (c) p-type non-Ohmic contacts. (d) p-type Ohmic contacts.

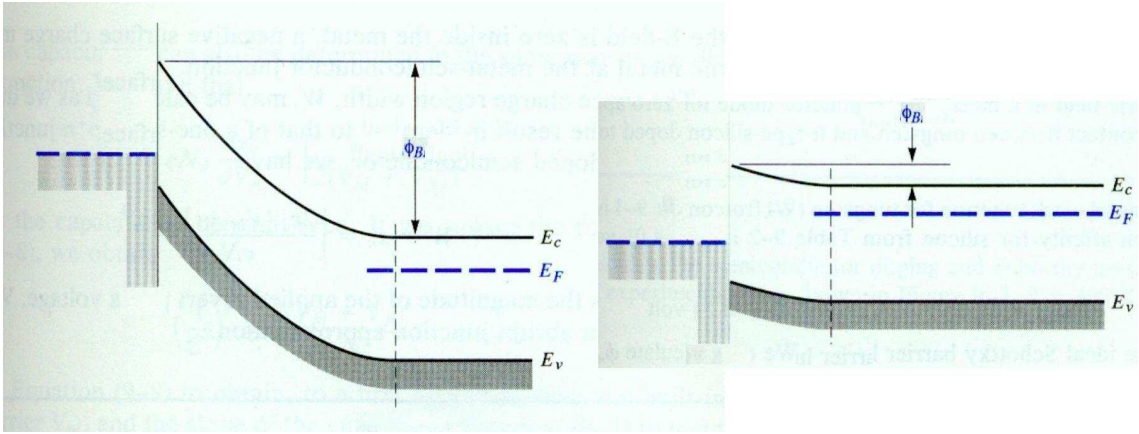

Figure 4.4: Band diagram of a metal-semiconductor contacts (Left) under reverse bias and (Right) under forward bias [87].

discussed when under an applied bias.

The barrier creates electrical resistance and the barrier height can be increased or decreased with an applied voltage. The Schottky barrier can be calculated via [88]:

$$\Phi_B = K(WF_{Metal} - WF_{Semiconductor}) \tag{4.8}$$

where K = material-dependent linear coefficient and $\mathrm{WF}_{material}$ the work function of the material. For the case of germanium/gold contacts, $\mathrm{K}_{germanium} = 0.2$ [89], $\mathrm{WF}_{germanium} = 4.78\,\mathrm{eV}$ [90], $\mathrm{WF}_{gold} = 5.28\,\mathrm{eV}$ [91], leading to a Schottky barrier height of 0.048 eV.

If a metal semiconductor interface is under an applied bias, then the Schottky barrier height is affected (Figure 4.4). If a positive bias is applied to the semiconductor (known as reverse bias), then the Schottky barrier height is increased. If a positive bias is applied to the metal (known as forward bias), then some of the energy supplied by the voltage source increases the Fermi energy of the semiconductor and this decreases the Schottky barrier. If the forward bias is sufficiently high, the barrier will disappear so beyond that voltage the junction acts as if it was Ohmic.

4.1.5 Germanium Films and Wires

Typically, germanium films from the literature have been grown in high vacuum via thermal evaporation and then electrically characterized [94–98]. The resistivity of a crystalline germanium thin film begins to vary from bulk when the thickness is less than 1 μm [94, 96]. The resistivity of intrinsic germanium increases from the bulk value of 40 Ωcm for 1 μm films to $\sim$5000 Ωcm for 5 nm films [96, 97].

Germanium nanowires have been produced by various methods including simple-vapour transport [101], vapour-liquid-solid growth [99], controlled vapour deposition

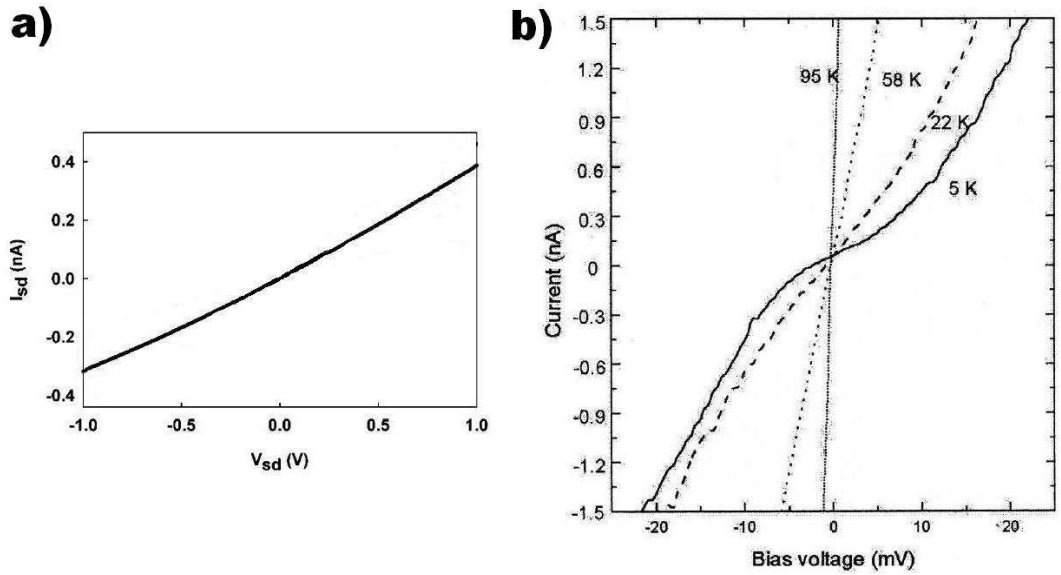

Figure 4.5: Current-voltage characteristics of germanium nanowires. (a) Room temperature I(V) characteristics for a single 80 nm wire [92]. (b) Temperature dependent I(V) characteristics for an array of germanium nanowires with 20-45 nm diameters [93].

[102], molecular beam epitaxy [103], chemical vapor deposition [104] as well as in chemical solutions [105]. In the cases where nanowires were fabricated on substrates, they could be electrically characterized.

Contacted germanium nanowires have shown linear I(V) curves over a ± 1 V range at room temperature [92], as shown in Figure 4.5(a). For these single germanium nanowires of 80 nm diameter, the effective resistivity was $\sim$1000 Ωcm. Temperature dependent I(V) data of a germanium nanowire is shown in Figure 4.5(b) [93]. These wires show non-linear I(V) characteristics in the extrinsic-carriers regime only with the non-linearity increasing for lower temperatures. No gate dependence was observed due to the difficulty of depleting the highly doped ($>10^{16}$cm^{-3}) channel. The higher conductance of these wires (compared to those in Figure 4.5(a)) is due to the greater level of doping. Germanium devices where gated behaviour has been observed are now discussed.

Germanium Nanotransistors

Because germanium is a semiconductor, a common research theme for germanium nanowires is to be used as the channel of a field-effect transistor [99, 100, 106–108] (also, see §1.1). Nanowires have been doped, with typical gate voltages applied of up to $|5\,\mathrm{V}|$. These gate biases affect channel current by up to six orders-of-magnitude. Some examples are now discussed.

Germanium nanowires of 20 nm diameter have been used to make FETs [99]. The

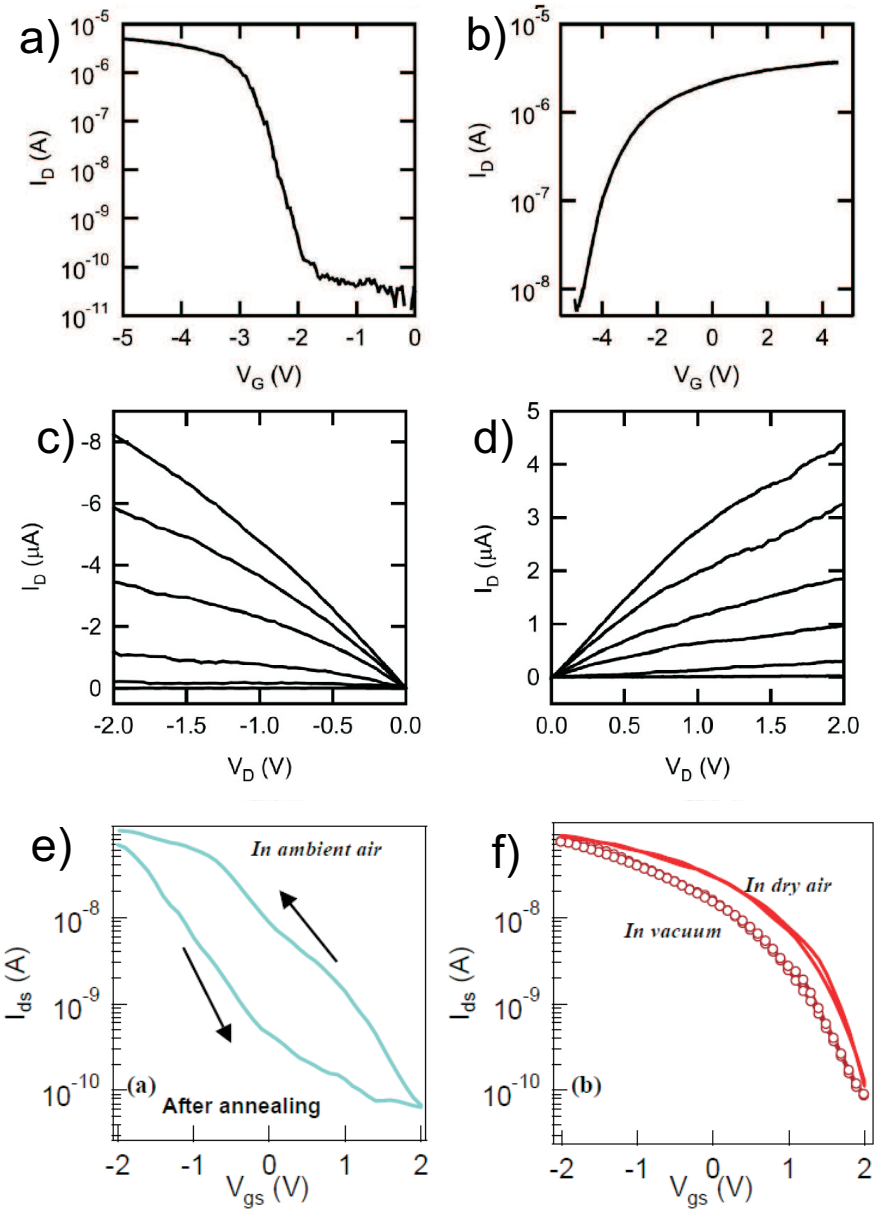

Figure 4.6: Germanium nanowire p- and n-FETs. a) Output characteristics of p-FET. The gate voltage was stepped in 0.5 V increments from 25 to 22.5 V. b) Transfer characteristic of p-FET at 1 V drain. c) Output characteristics of n-FET. The gate voltages were, starting from the top, 15 V, 12.5 V, 0 V, 20.5 V, 21.5 V, and 25 V. d) Transfer characteristic of n-FET at 1 V drain [99]. e)& f) comparison of p-type FET in vacuum, dry air and ambient air [100]. Devices in these figures use gold contacts.

wires were produced using vapour-liquid-solid growth. The p-type FETs showed a five order-of-magnitude current enhancement when a gate bias of -4 V was applied, shown in Figure 4.6(b). The device is normally off with gate voltage enhancing current. The n-type FET (Figure 4.6(d)) is normally on and increasing the gate voltage to 5 V causes a small increase to the channel current and a gate voltage of -5 V causes a three order-of-magnitude current decrease. Figure 4.6(a)&(c) show how the current-voltage characteristics change with gate bias for the both n and

p-type devices.

When germanium-nanowires FETs have been exposed to air, oxidation affected their characteristics. Wang *et al.* [100] studied germanium nanowires of 10 nm diameter to create p-type FETs with gold contacts. Figure 4.6(e) shows hysteresis of FET I(V) characteristics. When the water vapour was removed by having an atmosphere of either dry air or vacuum or by annealing, the hysteresis disappeared (Figure 4.6(f)) due to the removal of surface water molecules which are responsible for causing the hysteresis.

4.1.6 Germanium Nanoparticles

The semiconducting nature of germanium has attracted substantial nanoparticle research attention. Germanium nanoparticles have been studied via molecular dynamics [111, 112] and have been produced by a variety of methods, including controlled-vapour deposition [113, 114], solution synthesis of $GeCl_4$ [115, 116], by molecular-beam epitaxy [117], thermal evaporation [118], by a sol-gel method [119], ion implantation [120], CVD from gaseous GeH_4 [121] or, as used in this thesis, using the inert-gas-aggregation method [122–126, 126–131].

Many of the results suggest an observed change in the optical and electrical properties for particles less than a critical diameter due to a transition in the crystal structure. Saito [126] found that when clusters less than 20 nm in diameter were produced in a pure argon atmosphere, the crystal structure was tetragonal. For clusters larger than 20 nm, or if the system had an air-leak, the clusters were diamond structured. Both diamond and tetragonal unit-cells are shown in Figure 4.7.

Germanium clusters created by Taylor [115] via solution synthesis have been analyzed with an HR-TEM showing the 3.5 nm particles have a (bulk) diamond structure. Jiang [121] created particles above 5 nm in diameter which showed the bulk diamond structure. When particles were less than 5 nm they have a tetragonal

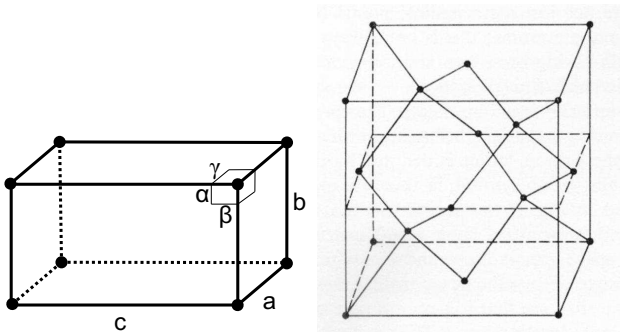

Figure 4.7: (Left): Unit cell of tetragonal lattice a = b ≠ c. $\alpha = \beta = \gamma = 90°$ [109]. (Right): Unit cell of diamond structure [110].

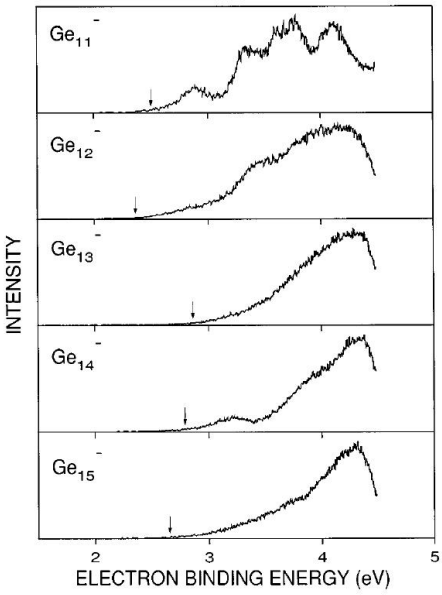

Figure 4.8: PES of germanium clusters. Arrows indicate electron affinities. [122].

structure, consistent with small germanium particles made by other methods. The cluster structure results are summarized in Table 4.3.

A blueshift in luminescence is common for small germanium clusters. Germanium clusters created by solution synthesis of $GeCl_4$ and separated by high-pressure liquid chromatography [116] have shown evidence for quantum confinement provided by a blue-shift in photoluminescence measurements. Zacharias [134] deposited small germanium particles into SiO_2 matrices. These clusters show blue luminescence at room temperature. Clusters were imaged under HR-TEM and shown to have a crystal structure change for clusters $\leq$4 nm in diameter [132]. A change in the spacing of the crystal structure is seen in the HR-TEM images, the lattice fringes of smaller clusters change from to 0.298 nm from the 0.326 nm bulk value.

Germanium clusters produced via methods which use an inert gas and germanium vapour are now summarized. Like other clusters, the ionization potentials [122–124] and crystal structures [125–127] have been analyzed. Negatively charged

Diameter	Notes	Reference
3.5 nm	No transition observed	[115]
2 nm	No transition observed	[116]
5 nm	No transition observed	[120]
5 nm	Transition to tetragonal	[121]
20 nm	Transition to tetragonal	[126]
4.5 nm	Transition to tetragonal	[132]

Table 4.3: Crystal structures of small germanium clusters. If no transition observed, structure is diamond.

germanium clusters up to 15 atoms in size have had ionization potentials determined using photoelectron spectroscopy (PES) [122, 135]. The observed bands are shown in Figure 4.8, the arrows indicating the work function of the clusters. If a bandgap exists, the extra electron in the negative cluster will be at the bottom of the conduction band. Removing two electrons will remove both the single electron in the conduction band and the highest energy electron of the valence band. The difference in energies of the electrons determines the bandgap. Electronic bands have been observed for clusters of more than 6 atoms, which indicates a move away from atomic behaviour.

Germanium Cluster Film I(V)s

Germanium cluster films have been electrically characterized [131, 133]. Films of 4 nm diameter germanium clusters have been deposited onto silicon substrates. The 30 nm thick films were sandwiched between two gold electrodes, shown in Figure 4.9(a)[3]. Figure 4.9(b) and (c) show I(V) characteristics at room temperature and low temperatures respectively. Linear behaviour was observed at room temperature

[3]These films differ from the percolation films used in this thesis (described in §2.5) because the films in Figure 4.9(a) are deposited onto gold and the electrical measurements are made through contacts orthogonal to the substrate.

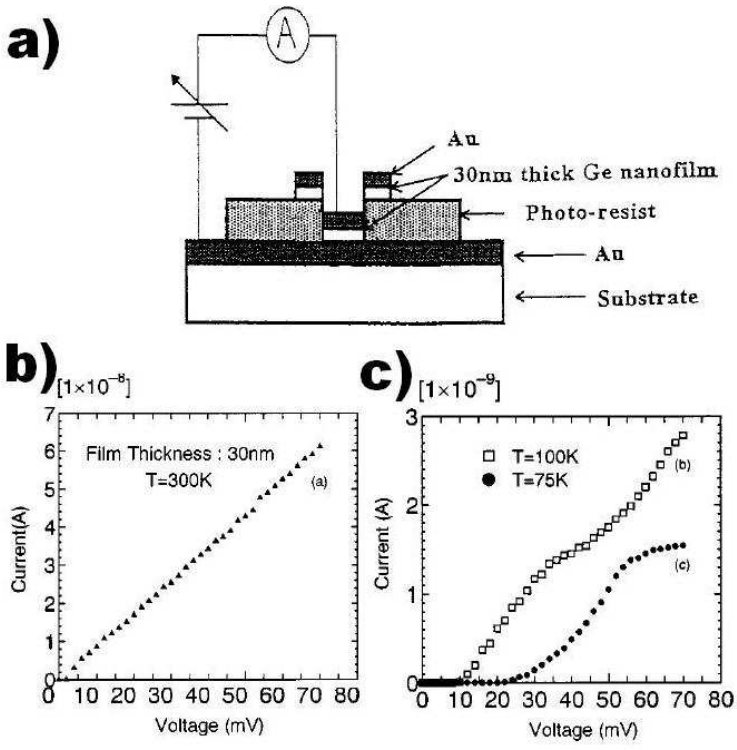

Figure 4.9: Figures taken from [133]. a): circuit schematic showing the sandwich nature of the 30 nm film. b): Linear I(V) characteristics at room temperature. c): non-linear I(V) characteristics at low temperatures.

and a temperature-dependent non-linearity was observed at T= 100K and 77 K. The suggested low-temperature conduction mechanism is Coulomb blockade by electrons tunnelling from cluster to cluster through the surface-oxide layers. These films studied by Banerjee show a low room temperature resistance of 1 MΩ, suggesting that the clusters have a high level of doping.

In order to produce germanium clusters using the Canterbury system (§2.1), a germanium cluster source was required. The details of the design and characterization of a germanium cluster source are described in the following section.

4.2 Germanium Cluster Source Design and Characterization

In order to produce germanium clusters, the IGA source described in §2.1.1 required modification. This chapter describes that process and the subsequent characterization necessary to prepare the cluster source for deposition of germanium cluster devices. §4.2.1 describes the development of an IGA source for germanium clusters. §4.2.3-§4.2.4 discuss the size and crystal structure characterization of germanium clusters using electron microscopy.

4.2.1 Development of an IGA Source for Germanium Clusters

Previously at Canterbury (§1.3.1) several materials have been used to produce clusters using the IGA system. The pumps and vacuum chambers used for germanium were the same system as used for bismuth; the difference being modified source components (see §2.1 for details of the Canterbury IGA system). The initial setup for germanium was an exact copy of the source design used for the production of copper clusters [27]. This decision was based on the similarities of the melting points and vapour pressures of germanium and copper which are displayed in Table 4.4.

The crucible and heat shields used for germanium are shown in Figure 4.10. The heatshields and lids (Figure 4.10(a)/(b)) were made from 99.9% pure, 0.10 mm thick tantalum foil. The inner and outer crucibles were made from hot-pressed boron nitride. Both the heatshields and crucibles were manufactured in-house by the Physics Department workshop. The inner crucible (Figure 4.10(d)) was threaded to hold the filament in place. The filament was made from 99.95% pure tungsten wire with a diameter of 0.5 mm±2%. The length of the filament was 58 cm which corresponded to a room temperature resistance of 0.6 Ω.

Figure 4.11 shows the variety of nozzles used to produce germanium clusters. Nozzles (a)&(b)&(c) are first-stage nozzles. (a) is made from boron nitride and (b)&(c) are made from graphite. Nozzles (d)&(e) are second-stage nozzles and (e) is the skimmer (a large diameter nozzle). Both the skimmer and second-stage nozzles are made from stainless steel.

	Germanium	Copper
Melting point	938°C	1085°C
Temperature for vapour pressure of 1 Torr	1644°C	1508°C

Table 4.4: Melting point and vapour pressures of germanium and copper.

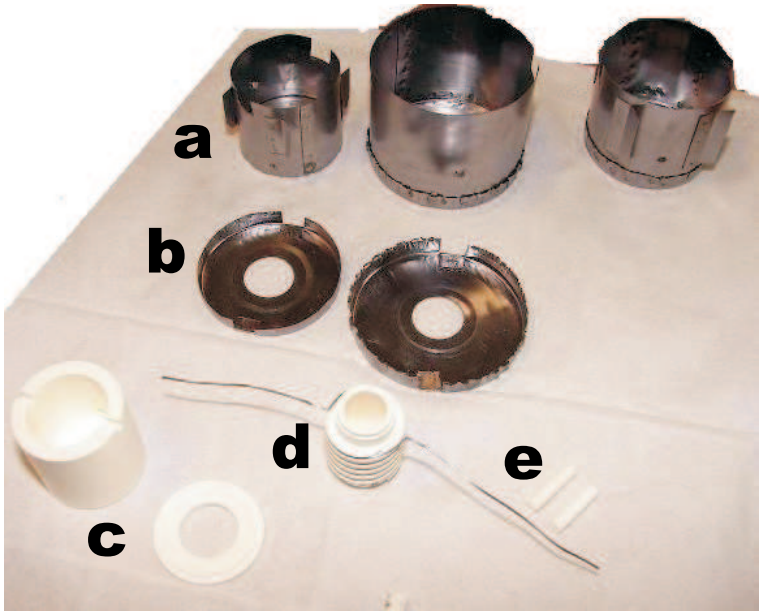

Figure 4.10: Components of the germanium source: (a)&(b) Tantalum heatshields and lids (c) Boron nitride outer crucible and lid. (d) Boron nitride crucible and tungsten filament (first design). (e) Alumina spacers for filament.

Despite the success of the copper nozzle/crucible configuration to produce copper clusters, no temperature and flow-rate combination produced a significant cluster deposition rate on the film-thickness monitor. Several nozzle configurations were attempted and a very small rate (0.02 Å/s) was able to be measured; if the temperature was increased further to increase cluster flux, the tungsten filament would fracture. The system had reached the upper limit of crucible temperature. In order to get more power into the crucible it was redesigned to have a longer filament. The new crucible design added 10 cm to the length of the tungsten filament to make the total length 68 cm and increased the filament resistance to 0.7 Ω. A comparison

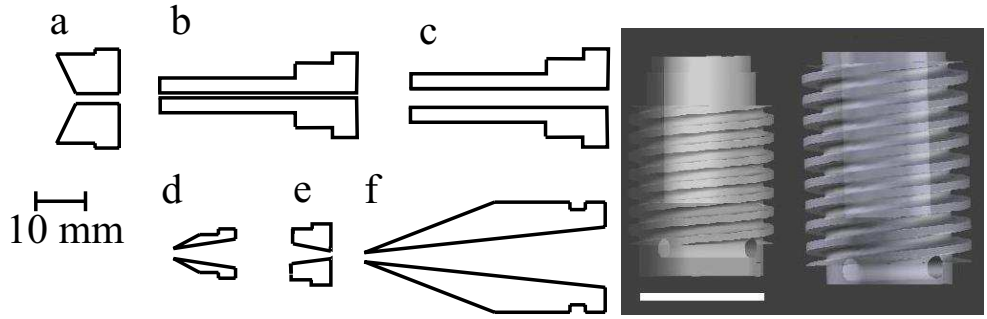

Figure 4.11: Left: Schematic of nozzles used for germanium. (a)&(b)&(c) First stage nozzles. (d)&(e) Second stage nozzles. (f) Skimmer. Minimum diameters of nozzles a): 2 mm b): 1 mm c): 4 mm d): 2 mm e): 1.5 mm f): 2.5 mm. Right: Crucible comparison showing original and modified designs. Scale bar = 12 mm.

Nozzle Configuration (1st/2nd/Skimmer)	Filament Length (cm)	Maximum Deposition Rate (Å/s)
a/d/f	56	0
b/d/f	58	0
c/d/f	58	0.02
c/d/f	68	0.15
c/e/f	68	40

Table 4.5: Germanium source iterations. Nozzle configurations and filament lengths with corresponding deposition rates. Nozzles correspond to those in Figure 4.11.

between the crucibles is shown in Figure 4.11. Both crucibles had a double-start thread with 4 mm pitch. The original crucible had 4.5 rotations per thread, for the final design this was increased to 5.5 rotations per thread. The total height of the crucible was kept constant by removing vestigial spacing at the top and bottom of the crucible. With the new crucible design in place, cluster production became more reliable. The nozzle configurations and filament lengths with corresponding deposition rates are shown in Table 4.5 and the corresponding range of deposition conditions are shown in Figure 4.12. With a reliable source and nozzle configuration (nozzles c/e/f from Figure 4.11), the source was now able to be characterized further.

The range of cluster-producing temperatures and argon flow rates for the germanium inert-gas aggregation source was 1350-1580°C and 30-250 sccm. As source temperature and gas flow rate can determine cluster size [26] and cluster bouncing on substrates (§1.3.2), variations in both these parameters were investigated.

Two methods were used for the size determination of germanium clusters. Initially, clusters were deposited onto silicon substrates and inspected using a scanning electron microscope (SEM). Cluster sizes were then determined more accurately

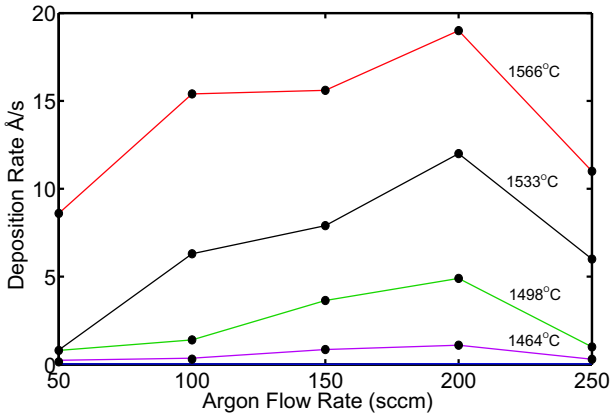

Figure 4.12: Examples of deposition rate variation for selected argon flow rates and crucible temperatures with nozzles c/e/f from Figure 4.11. Lines are a guide to the eye only.

via transmission electron microscopy (TEM) of clusters deposited onto TEM grids. Cluster morphology and presence of germanium oxide were investigated using a high resolution TEM.

4.2.2 Germanium Cluster Size Analysis using Scanning Electron Microscopy

Clusters were deposited (as described in §2.1.2) onto silicon with a passivation layer of silicon oxide. The silicon samples had a small number of etched inverted pyramids and V-grooves. The inverted pyramids/V-grooves were used to assess any variation in cluster bounce. Clusters were deposited onto ten samples; five with the same crucible temperature (1480°C) with different argon flow-rates and five with a constant argon flow-rate (50 sccm) and different temperatures. Examples of SEM images of the germanium clusters are shown in Figures 4.13 and 4.14.

Figure 4.13 shows two SEM images of clusters produced with an argon flow rate of 50 sccm and the source temperatures of 1385°C and 1475°C for (a)&(b) respectively. Figure 4.13(a) has an even cluster coverage and cluster size of ∼30 nm. The cluster coverage on the V-grooves is the same as the planar part of the substrate. This indicates clusters were not bouncing, the clusters stick where they land [29]. Accurate determination of cluster size was difficult using the SEM, although it appears the clusters have a larger diameter in Figure 4.13(b).

There are two main factors contributing to the poor resolution of germanium clusters when using an SEM. Firstly, germanium is a semiconductor (with possible germanium oxide layers), hence clusters are prone to charging effects when being imaged. In addition, since germanium has a relatively low atomic number (32), with

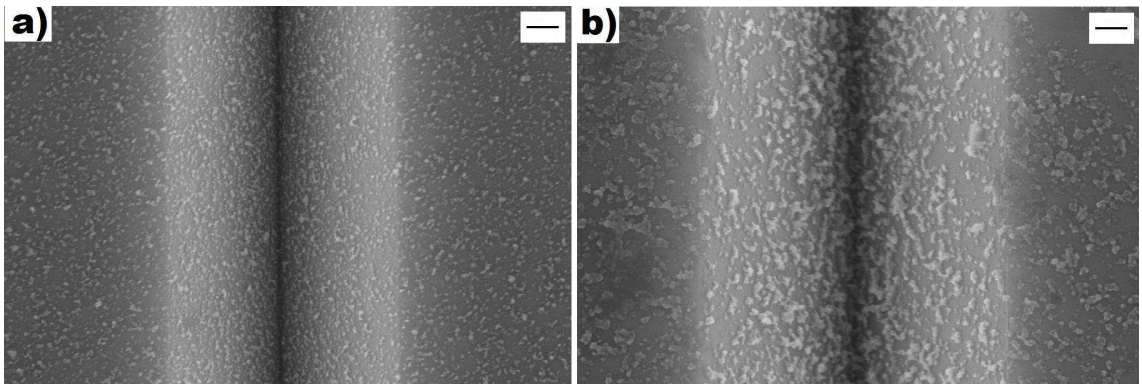

Figure 4.13: Scanning electron microscope images of germanium clusters with a source argon flow rate of 50 sccm. a) Sample 1; Source temperature: 1385°C. Deposition rate: 0.31 Å/s. Deposition time: 120 s. b) Sample 2; Source temperature: 1475°C. Deposition rate: 0.81 Å/s. Deposition time: 30 s. Scalebars are 200 nm.

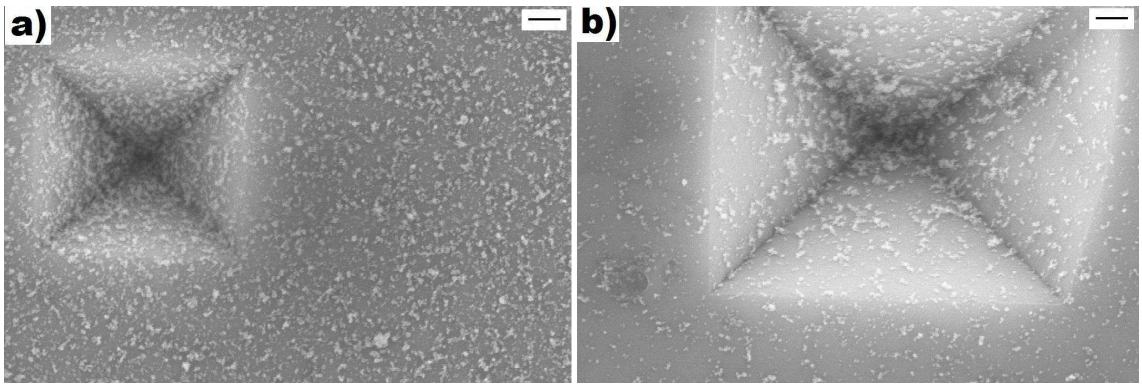

Figure 4.14: Scanning electron microscope images of germanium clusters with a source temperature of 1480°C. a) Sample 1; Argon flow rate 50 sccm. Deposition rate: 1.97 Å/s. Deposition time: 30 s. b) Sample 5; Argon flow rate: 110 sccm. Deposition rate: 1.41 Å/s. Deposition time: 30 s. Scalebars are 200 nm.

a smaller number of electrons in each atom to interact with the electron beam, high resolution imaging of small particles is difficult.

Figure 4.14 shows two SEM images of clusters with the same source temperature of 1480°C but different source flowrates. The argon flow rates were 50 and 110 sccm for (a)&(b), respectively. In Figure 4.14(a) there is a reasonably even coverage of clusters across the substrate, including inside the inverted pyramid, suggesting that the clusters were not bouncing much, or at all. For Figure 4.14(b) there appears to be a greater number of clusters at the apex of the pyramid compared to the surrounding substrate which is strong evidence for clusters bouncing. A higher argon source flow rate produces clusters with higher velocity, so more bouncing is expected, which is consistent with previous studies of bismuth clusters (§1.3.2). The clusters were approximately 25 nm in diameter for both Figure 4.14(a)&(b). Any size difference between samples was not distinguishable with the resolution of the SEM.

These initial experiments determined that the size and the tendency to bounce of germanium clusters is variable for certain values of source conditions. However, scanning electron microscopy was insufficient to accurately determine how cluster properties varied with source conditions. A higher resolution imaging technique was required and this was provided by transmission electron microscopy.

4.2.3 Germanium Cluster Size Analysis using Transmission Electron Microscopy

After deposition onto TEM grids, cluster size was determined with an accuracy of 0.5 nm for a variety of source conditions.

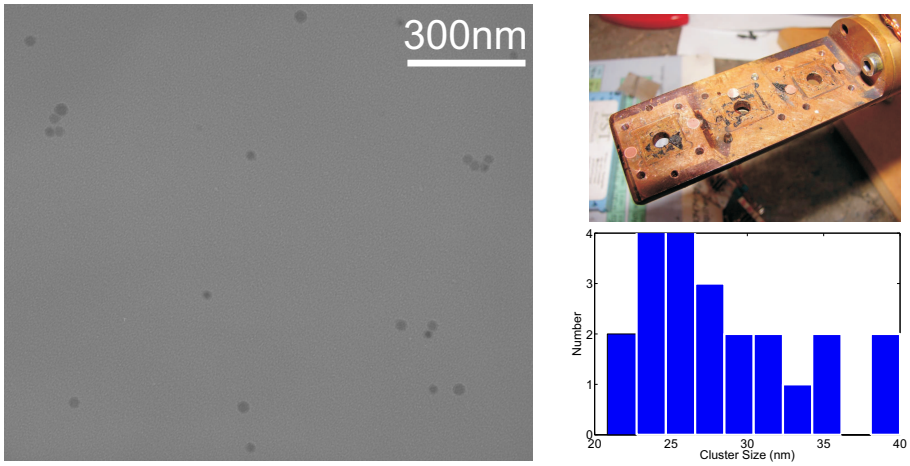

Figure 4.15: Left: Typical TEM image taken with Hitachi H-600 at 100 kV. This image shows TEM sample 7 magnified 150,000×; germanium clusters produced at a temperature of 1464°C and with an argon flow rate of 100 sccm. Right (top): TEM grids mounted on sample arm, ready for loading into UHV deposition chamber. Grids were mounted with a carbon tab adhesive. There was a maximum of five grids per deposition. Right (bottom): Cluster size analysis of TEM sample 7.

TEM grids were attached to the sample arm via a tiny piece of a vacuum-compatible adhesive carbon tab shown in Figure 4.15(top right). The beamspot size had to be taken into account when positioning the TEM grids to ensure that each deposition was only on a single sample. Hence, up to five TEM grids could be mounted at one time. Clusters were deposited on 23 TEM grids and the deposition details are shown in Table 4.6.

TEM grids were inspected using a Hitachi H-600 TEM operated with an accelerating voltage of 100 kV. Images were exposed onto Kodak SO-163 electron image film and developed in house. The microscope is located in the Canterbury University

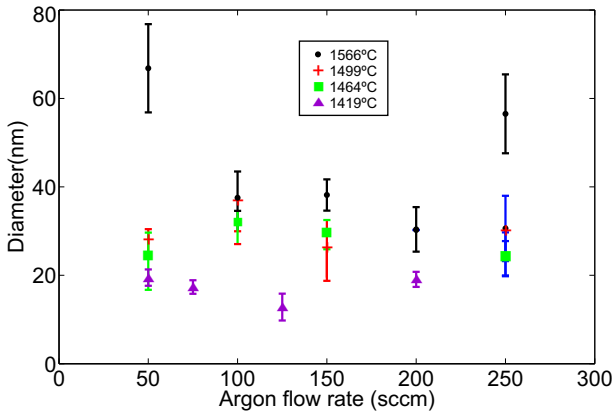

Figure 4.16: Variation in size of germanium clusters depending on flowrate of argon. Error bars were calculated using the standard deviations of cluster diameters. Key: Purple triangle = 1419°C, green square = 1464°C, red cross = 1499°C, black dot = 1564°C

.

Sample #	Temperature °Celsius	Source pressure Torr	Flow rate sccm	number of clusters measured	σ nm
1	1419	1.18	50	25	4
2	1418	1.58	75	15	4
3	1419	1.93	100	15	5
4	1420	2.28	125	25	6
5	1419	3.76	250	15	8
6	1466	1.15	50	15	13
7	1464	1.90	100	15	7
8	1465	2.58	150	15	7
9	1464	3.19	200	15	8
10	1464	3.78	250	15	10
11	1499	1.22	50	15	5
12	1498	1.96	100	15	11
13	1498	2.64	150	15	13
14	1498	3.26	200	15	10
15	1500	3.82	250	15	10
16	1535	1.14	50	15	13
17	1533	1.90	100	15	12
18	1533	2.58	150	25	11
19	1566	1.20	50	25	20
20	1567	1.97	100	15	15
21	1567	2.66	150	15	8
22	1567	3.30	200	9	11
23	1568	3.93	250	9	18

Table 4.6: Data for deposition of germanium cluster onto TEM grids. Temperature and flow rate set manually. σ = error.

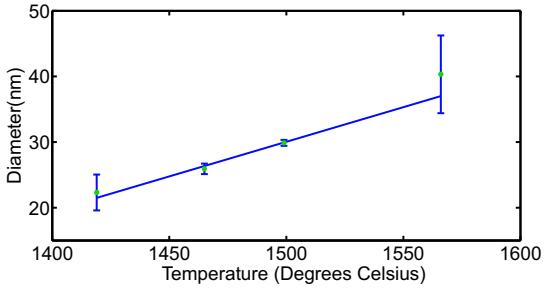

Figure 4.17: TEM results showing size variation depending on temperature. Flowrates for a given temperature are averaged over all flowrates and the error bars were calculated using the standard deviations of sizes for each image. The fit is a linear guide to the eye.

Mechanical Engineering department. All TEM grids were imaged at the maximum magnification of the system, which is 300,000× and also 150,000×, an example of which is shown in Figure 4.15(left).

Cluster diameters were determined using enlarged printed images and a set of digital calipers and an example of a size distribution is shown in Figure 4.15(bottom right). Variation in size are shown in Figures 4.16 and 4.17. The error bars are derived from the mean (location of error bar center) and standard deviation (height from center).

Figure 4.16 shows the variation in cluster size for different flow rates. The size of the clusters ranges from 10-65 nm. There are up to four data points for each value of the flow rate each corresponding to four different source temperatures. There appears to be a weak trend suggesting clusters are larger for higher flow rates. The majority of source conditions produced clusters with diameters in the range of 20-35 nm.

Figure 4.17 shows the variation in cluster size for different source temperatures. The size of the clusters ranges from 10-65 nm. The data points on Figure 4.17 are the values for each temperature averaged for each of the five flow rates. There is a clear correlation between source temperature and cluster diameter; as the source temperature is increased, the clusters increase in size. The fit has an approximate gradient of ∼1 nm/100°C. This data is useful for choosing the most effective source conditions for the particular substrate being deposited onto.

4.2.4 Germanium Cluster Crystal Structure Using High Resolution Transmission Electron Microscopy

To investigate the cluster crystal structure transmission electron microscopy with higher resolution was required. TEM grids were sent to Victoria University, Welling-

ton and inspected by using a JEOL 2100 200 keV TEM.

A typical image from the high coverage grids is shown in Figure 4.18(left). The images were focused on a single particle and showed one interference pattern across the most of that particle. This uniform interference pattern showed the clusters were single crystal and that there was a small amorphous oxide shell. The average lattice fringe spacing observed for several clusters was 3.24 Å, which is consistent with previous studies that have observed a lattice spacing of 3.26 Å [132] for germanium clusters of diamond structure.

In addition, crystal structures were able to be investigated using Selected Area Electron Diffraction (SAED). SAED is a crystal analysis technique which is used for elemental analysis. A TEM grid with higher coverage was deposited using the same source conditions. The SAED results are shown in Figure 4.18(right). The indexing on the SAED corresponds to a diamond crystal structure. All germanium clusters imaged with TEM showed the same lattice-fringe spacing, suggesting that the structure is diamond consistently.

With the cluster source now characterized in terms of cluster size, deposition and electrical characterization could take place.

4.3 Germanium Films Deposition: Onset of Conduction and Oxidation

The following section discusses the electrical behaviour of germanium cluster films both during and directly after deposition. Initially, special considerations for semi-

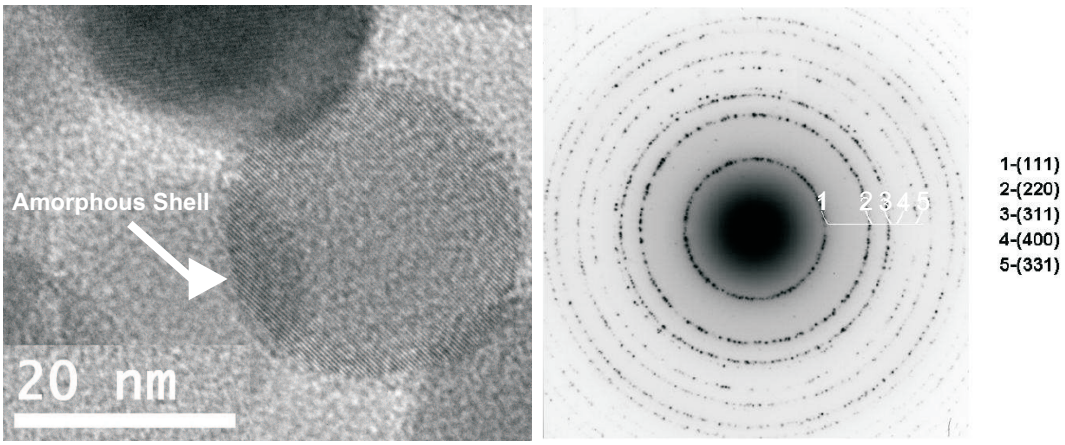

Figure 4.18: Left: High Resolution TEM image of a germanium cluster. This image shows sample 12; produced at a temperature of 1498°C and with an argon flow rate of 100 sccm. Right: Selected Area Electron Diffraction of germanium clusters corresponding to diamond cubic germanium.

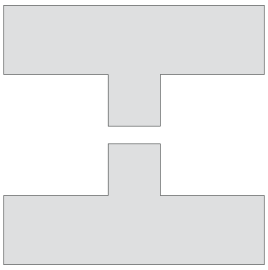

Figure 4.19: Schematic of percolation sample. Gap between electrodes = 100 μm. [26]

conducting clusters are allowed for (§4.3.1), then onset of conduction (§4.3.3) and subsequent increase in resistance due to oxidation of clusters (§4.3.4) are discussed.

4.3.1 Germanium Films: Onset of Conduction Considerations

Special considerations were required before depositing germanium clusters due to the semiconducting nature of germanium. The voltage applied between the contacts used to measure onset of conduction (as defined in §2.4.1) has previously been tens of millivolts for metallic cluster devices, enough to detect conduction without annealing the device.

Semiconducting clusters might be expected to form a Schoktty barrier with the gold contacts (§4.1.4). If a source-drain voltage used to detect onset of conduction is less than the barrier height, then any conduction of a device will be more difficult to measure.

In addition, the undoped germanium will be expected to have a high resistivity. A crude estimation of the expected resistance is now attempted. The resistivity of a cluster film can be divided into three terms:

$$\rho_{total} = \rho_{film} + \rho_{contactresistance} + \rho_{boundary} \tag{4.9}$$

The expected resistance of a 50 nm thick, 200 μm long, intrinsic bulk germanium film is 20 MΩ. For metallic cluster films [26], the $\rho_{boundary}$ term typically increases the resistivity by a factor of ten. If an upper resistance of 1 GΩ is assumed, a voltage of 5 V provides a 5 nA current, which is easily measurable above noise and leakage levels. Hence, a 5 V source-drain voltage was used as a starting point for detection of conduction in percolating films (contacts resistance assumed not to be significant).

Percolation Sample Overview

Devices discussed in this subsection are percolating films of germanium clusters. A device schematic is shown in Figure 4.19, the distance between the electrodes is 100 μm. Gold contacts were deposited onto Si/Si_3N_4 substrates by thermal evaporation, other fabrication details are described elsewhere (§2.3.3).

When clusters were deposited onto these substrates, a film of clusters connects the electrodes. These samples are referred to as percolation samples throughout the chapter (although films typically have a coverage exceeding the percolation threshold). These samples were used for the initial electrical characterization of germanium clusters.

4.3.2 Germanium Films Deposition: Onset of Conduction and Subsequent Oxidation

The onset of conduction for germanium films differs from metallic cluster films previously studied at Canterbury. For germanium cluster films to have a level of conductance distinguishable from leakage current, film thicknesses are required to be in excess of the percolation threshold. This requirement of thicker films is caused by two factors: low conductivity of germanium clusters and devices having a fast rate of oxidation. When the deposition is complete, the current immediately decreases before stabilizing, despite the sample being in high vacuum. A typical onset and

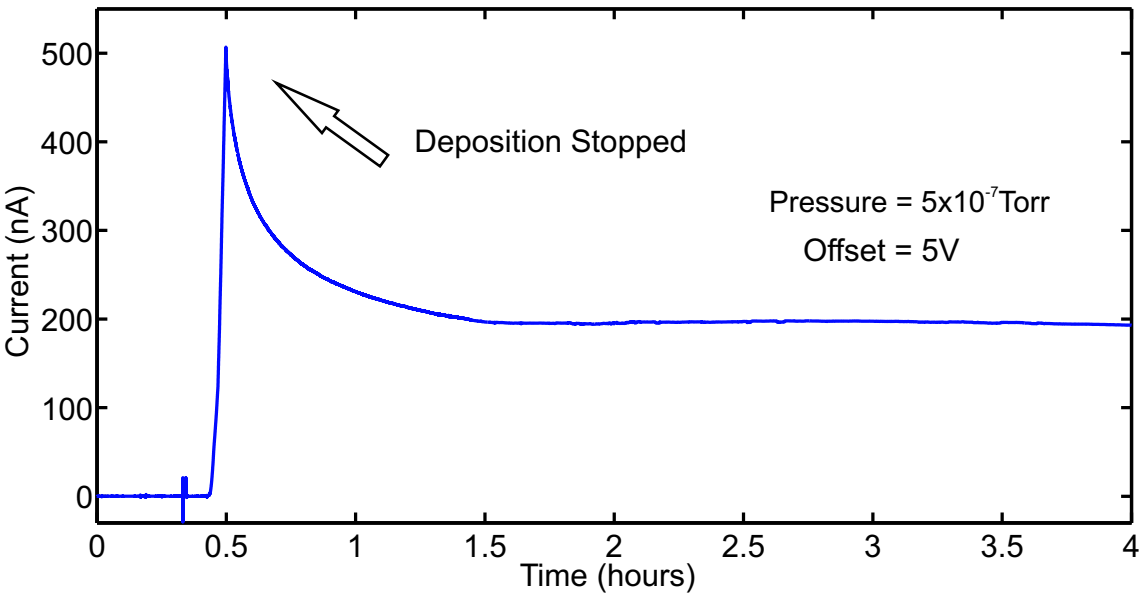

Figure 4.20: Left: Onset of conduction and oxidation data for Sample 4. The IGA source was heated to 1515°C and combined with an argon flow rate of 180 sccm to produce a deposition rate of 1.1 Å/s. During a deposition time of 30 minutes, the resistance decreased to 10 MΩ. The corresponding film thickness was 200 nm.

Sample #	Thickness	Energy Gap	Oxidation Power Exponent	Notes
1	130 nm	0.24 eV	-	Figure 4.26
4	200 nm	-	-0.47	Figure 4.23
5	490 nm	0.73 eV	-0.28	Figure 4.23, 4.26 and 4.27
11	50 nm	-	-	
12	260 nm	0.41 eV	-	Figure 4.26, 4.24 and 4.25
13	270 nm	-	-	
14	270 nm	-	-	
18	400 nm	-	-	
34	60 nm	0.44 eV	-0.5	Figure 4.23 and 4.26
40	240 nm	-	-0.94	Figure 4.23
44	60 nm	-	-	Figure 4.27
45	120 nm	0.32 eV	-	
48	75 nm	-	-0.87	Figure 4.23
50	550 nm	-	-	Figure 4.26
51	200 nm	-	-0.86	Figure 4.22
52	270 nm	0.32 eV	-	Figure 4.26
55	200 nm	-	-	
60	90 nm	-	-0.57	Figure 4.23 and 4.26
64	40 nm	-	-	
68	450 nm	-	-	
71	250 nm	0.32 eV	-	Figure 4.26
73	550 nm	0.53 eV	-	Figure 4.26
74	500 nm	0.58 eV	-	Figure 4.26
77	420 nm	0.51 eV	-	Figure 4.26 and 4.28
92	500 nm	-	-	Figure 4.29

Table 4.7: Parameters of selected germanium films showing Figures used throughout this chapter.

oxidation are shown in Figure 4.20 and are discussed in the next two subsections.

4.3.3 Germanium Films Deposition: Onset of Conduction

This subsection discusses the electrical properties of percolating films of germanium clusters during cluster deposition. Figure 4.20 shows the onset of conduction and oxidation of Sample 4. The IGA source was heated to 1515°C and combined with an argon flow rate of 180 sccm to produce a cluster flux of 1.1 Å/s. During a deposition time of 30 minutes, the resistance decreased to 10 MΩ. The corresponding film thickness was 200 nm. At all times during deposition, the sample had a source-drain voltage of 5 V.

Figure 4.21(top) is a magnified view of Figure 4.20 and shows the onset behaviour of a typical germanium cluster film. Unlike the onset of conduction for metallic clusters, there is not a sharp increase in current. The deposition of Sample 4 took place from t=30 seconds to t=30 minutes. There is no consistent increase in conduction before t=25 minutes and at this time the film is already 160 nm thick. This behaviour is expected during the deposition of a high resistance film [136]. For clusters of 30 nm diameter, this thickness is far above the percolation threshold. Properties of selected germanium cluster films are shown in Table 4.7.

The log-scale for the current on 4.21(top) reveals a high level of noise before the

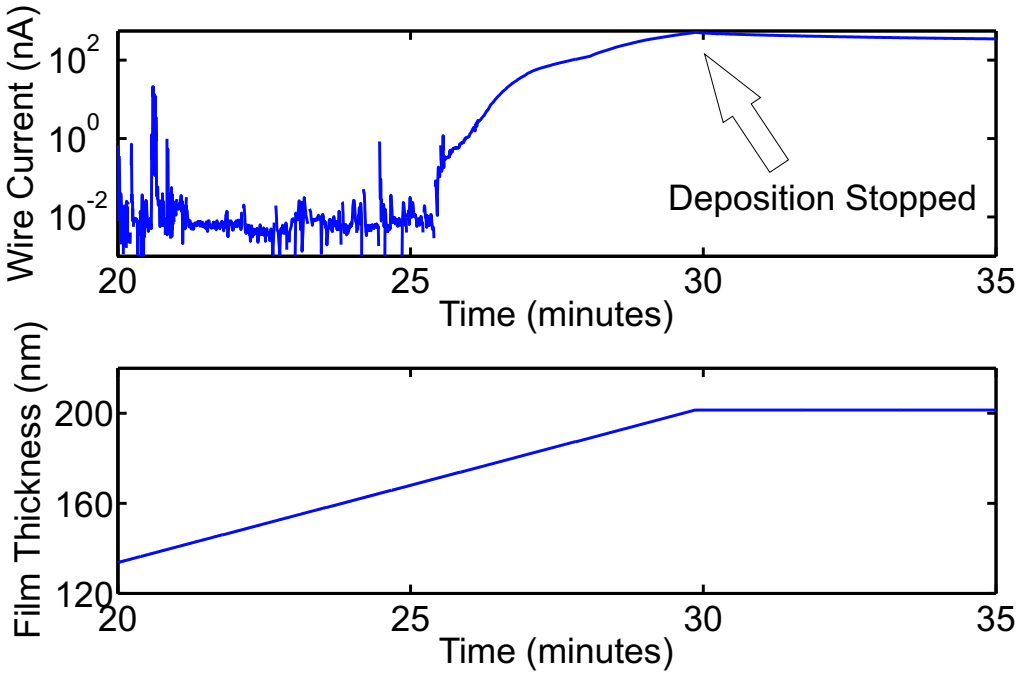

Figure 4.21: Top: Sample 4 onset of conduction on log-current scale. Bottom: Corresponding film thickness as a function of time.

onset of conduction occurs. The noisy pre-onset behaviour is similar to behaviour observed in cluster devices of other materials pre-onset. For Sample 4, the onset of conduction took place over a five minute period with a current increase rate of 100 nA/minute. The deposition was stopped when the current reached 500 nA. Immediately after the deposition was complete, the current began to decrease.

4.3.4 Germanium Films Deposition: Oxidation after Deposition

This subsection discusses the increase in resistance observed directly after deposition is complete. The conductance decrease began when the gate valve was shut ending the deposition. Although the film was still in high vacuum, the conductance of the films decreased according to a power law. The decrease in current is shown in the right-hand-side of Figure 4.20 and is also plotted for a typical sample on a log-log scale on Figure 4.22. For this sample, the conductance reached equilibrium approximately one hour after the deposition ended. The results for percolating films are shown in Table 4.7, the power law exponents for different films vary between -1.2 and -0.2.

The power-law exponent, an indication of how fast the film oxidizes, correlates with the deposition time and deposition rate, shown in Figure 4.23. It appears that films which are deposited quickly and/or for a short period of time oxidize faster and that this is independent of the film thickness. A possible explanation for the observed trends is that the initial layers of clusters that are deposited are in physical contact with the electrical contacts and it is assumed that the oxidation of these initial clusters are more important to the measured resistance of the film. If the deposition rate is high, the "contact clusters" are quickly covered by other clusters which slows their oxidation rate.

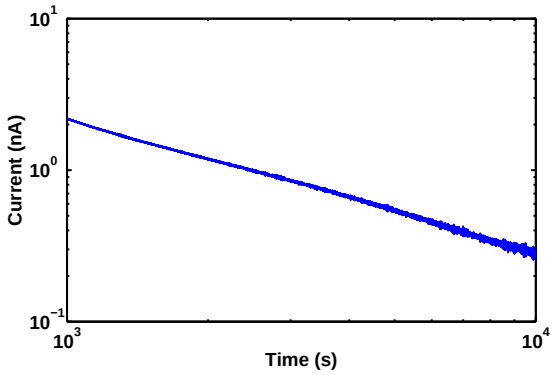

Figure 4.22: Oxidation of Sample 51. The log-log scale reveals the power-law exponent of -0.86.

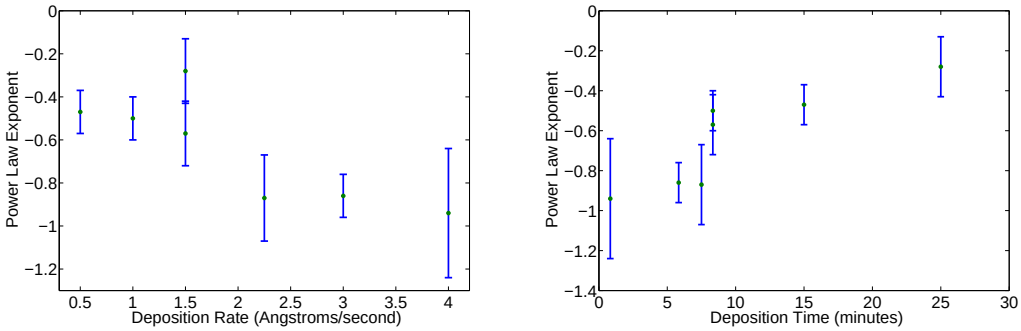

Figure 4.23: Left: Power law exponent dependence on deposition rate. Right: Power law exponent dependence on deposition time.

Oxidation versus Coalescence

After deposition of a cluster film is complete, the conductance can change over time for a number of reasons, including coalescence, annealing or oxidation of clusters. Coalescence was not observed for films of germanium clusters. Figure 4.24 shows two cluster films, one germanium and one bismuth. Both films had ∼30 nm diameter clusters deposited onto identical substrates and remained in high vacuum for 3 days. Figure 4.24(left) shows a germanium film where individual clusters are visible whereas Figure 4.24(right) shows coalesced bismuth clusters. This rules out the post-deposition change in conductivity is due to coalescence. It is therefore concluded that the post-deposition decrease in conductance is due to oxidation. A possible explanation for clusters not coalescing is the fast oxidation process in vacuum, as it has been observed for bismuth clusters that the coalescence process ceases when clusters have been oxidized [137].

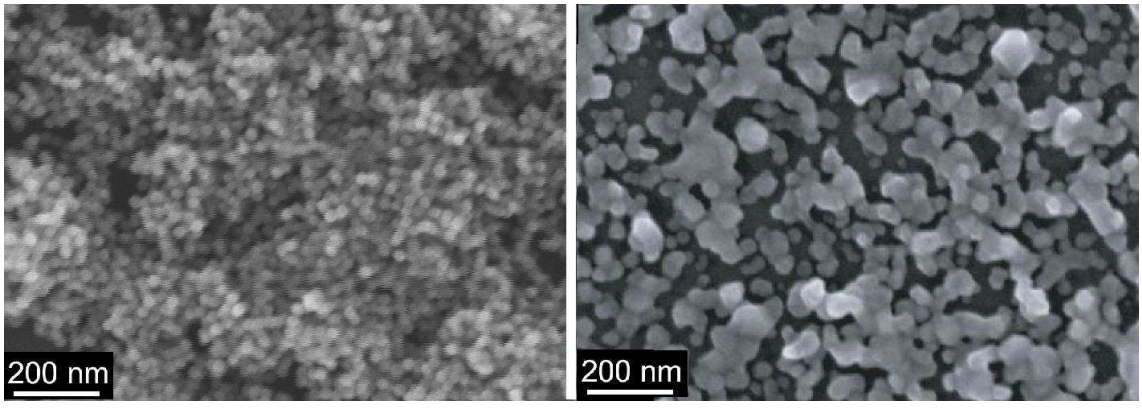

Figure 4.24: SEM images of cluster films held in vacuum for 3 days after deposition. Left: Germanium Sample 12. Right: Bismuth sample from [137]. The germanium clusters show no signs of coalescence and bismuth clusters are highly coalesced.

4.4 Germanium Films: Temperature-Dependent Electrical Characteristics

This section describes how the resistance of films of germanium clusters varies with temperature. The temperature-dependent electrical properties of a semiconductor are an important characterization tool for semiconductors, as reviewed in §4.1.3.

4.4.1 Experimental Technique

After samples had been deposited as described in §4.3.2, temperature-dependent data could be recorded. The data was recording using the following method. The sample temperature was reduced to 77 K when liquid nitrogen was added into the cryostat. The temperature was monitored and recorded via two temperature diodes and LabView. The temperature was allowed to naturally return to room temperature and this process took approximately twelve hours (additional details of data acquisition in §2.4.1). During this time, the resistance and temperature were recorded every five seconds. At all times during low temperature measurements samples were in high vacuum.

4.4.2 Temperature-Dependent Electrical Behaviour

The temperature dependent resistance of a typical germanium film is shown in Figure 4.25(left). Sample 12 is a percolating film deposited with source conditions of 1365°C and an argon flow rate of 50 sccm giving a 260 nm film thickness. The room temperature resistance is 4 GΩ and this increases rapidly at lower temperatures until the resistance reaches roughly 25 GΩ at 210 K. Below 210 K there is a slight resistance increase which continues to 77 K. Figure 4.25(right) shows the same data plotted

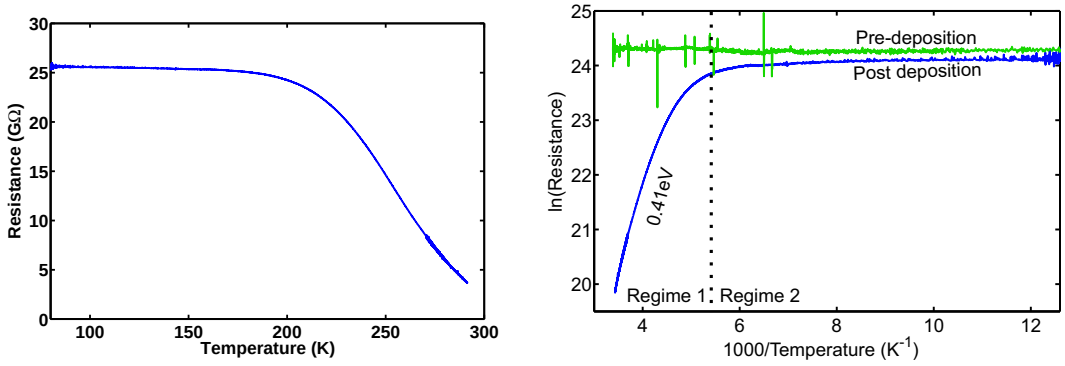

Figure 4.25: Left: Resistance variation with temperature for Sample 12 from liquid nitrogen to room temperature. Right: Same data on a log-scale in blue. Bare substrate temperature-resistance characteristics in green. Regime 1 and 2 from §4.1.3.

on a log scale. The two slopes present in Figure 4.25(right) correspond to regime 1 and regime 2 from §4.1.3. The slope in regime one is related to the bandgap of the film through Equation 4.4. The bandgap is calculated as 0.41±0.4 eV. This is less than the 0.71 eV expected for germanium. Other groups have reported measuring activation energies for germanium devices in this bandgap range [92, 138].

The resistance in regime 2 is very high and the measured current is close to the leakage current of the substrate. However, the green curve of Figure 4.25(right) shows the pre-deposition temperature dependence and this demonstrates that the current measured at 77 K is attributed to more than leakage values. No information about the activation energy of any impurities can be determined from this data as the temperature range does not extend to regime 3. Lower temperature measurements were attempted, but below 77 K the current measured was not distinguishable from the leakage current across the substrate, so meaningful low temperature results were not possible.

Figure 4.26 shows the variation for the measured bandgap of percolating films. The measured bandgap is largest for thicker films. The largest measured bandgap of the 500 nm thick film is consistent with the expected value of 0.71 eV of bulk germanium. Although a small number of papers have reported smaller than bulk value bandgaps for germanium films [92, 138], a possible explanation is that the temperature range where the activation energy was extracted from was not large enough for films with low impurity levels. It is possible that increasing the temperature to ∼500°C may reveal a slope with a smaller uncertainty that is therefore more linear than Figure 4.25(right) leading to a gradient closer to the expected value of

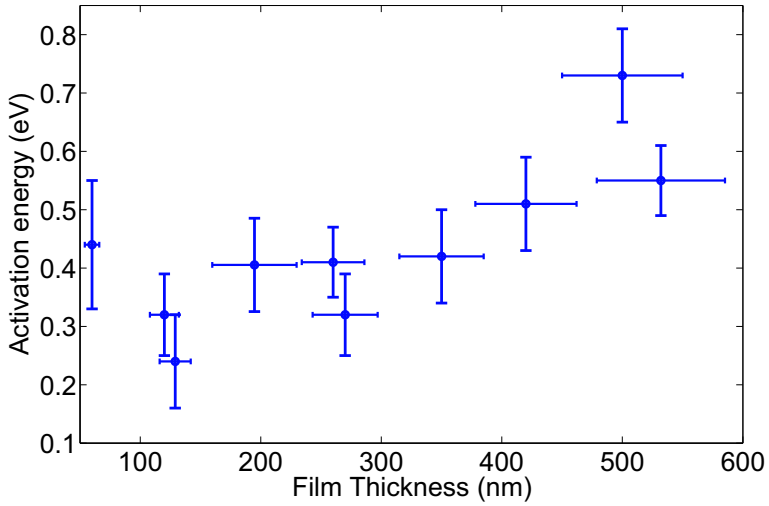

Figure 4.26: How the measured bandgap of percolating films of germanium clusters varies with film thickness. Error bars were derived from the variation in deposition rate during deposition and the activation energy was from the uncertainty in the linearity of the bandgap slope.

0.71 eV. Unfortunately, the current set-up at Canterbury doesn't allow for in situ temperature measurements in that range.

4.5 Germanium Films: Current-Voltage Characteristics

Typically, the first characterization technique performed after deposition was current-voltage characterization at room temperature. Three types of I(V) curves were observed: high-resistivity linear curves, low-resistivity linear and non-linear curves.

4.5.1 Germanium Films: Linear Current-Voltage Characteristics

An onset of conduction was not observed for all samples. When an onset was observed, the current-voltage characteristics were linear for the majority of samples with the remaining samples showing non-linear current-voltage characteristics.

Figure 4.27(left) shows the current-voltage characteristics for Sample 44. Sample 44 was a percolating film sample of 60 nm thickness with clusters of ∼30 nm diameter. The I(V) curve is linear with a slope corresponding to resistance of 8.5 GΩ. There is a noticeable hysteresis due to capacitive charging that occurs as a result of the voltage ramp used to measure the current-voltage characteristics, an effect discussed in §2.4.2. The pre-deposition current-voltage characteristics are also shown in Figure 4.27(left) to demonstrate the hysteresis is an effect not associated with the film. All films with high resistance (>1 GΩ) showed linear I(V) characteristics.

Figure 4.27(right) shows the current-voltage characteristics for Sample 5. Sample 5 was a percolating film sample of 490 nm thickness with clusters of ∼30 nm

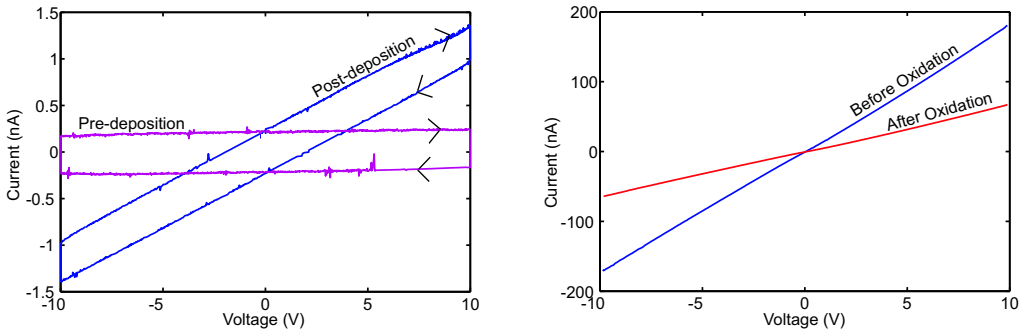

Figure 4.27: Linear current-voltage characteristics of germanium films. (Left): current-voltage characteristics of bare substrate and Sample 44 showing both the high resistivity I(V) with visible hysteresis due to capacitive charging effect. (Right): Sample 5 showing linear I(V) characteristics with no hysteresis both before and after oxidation in vacuum.

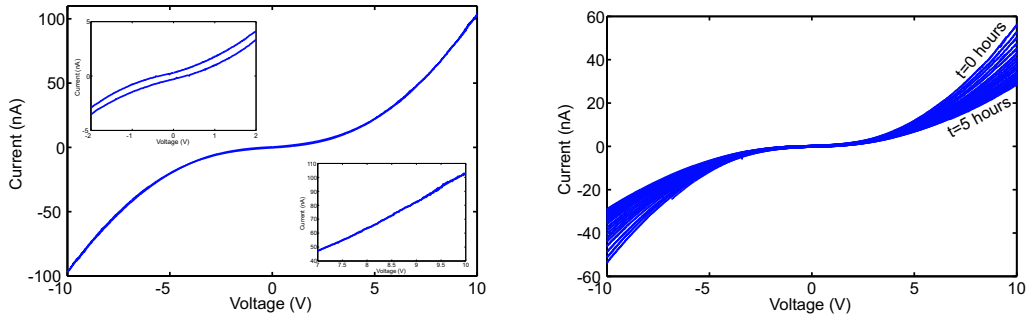

Figure 4.28: Current-voltage characteristics for Sample 77. (Left): Single I(V) curve showing non-linearity directly after deposition during the oxidation in vacuum stage. (Right): Time evolution of non-linearity over 5 hours showing decrease in non-linearity over time.

diameter. The blue curve shows the current-voltage characteristics before a period of oxidation in vacuum. The red curve shows the current-voltage characteristics after a 12 hour period of oxidation in vacuum. Both curves are linear with slopes corresponding to resistances of 150 MΩ and 55 MΩ respectively. The linear current-voltage characteristics imply the Fermi level of the films is less than the Fermi level of the gold contacts[4].

4.5.2 Germanium Films: Non-linear Current-Voltage Characteristics

Over ninety germanium films were deposited, with eight showing non-linear I(V) characteristics. Figure 4.28(left) shows the current-voltage characteristics of Sample 77 in the ±10 V range. Sample 77 is a two-point percolation sample of 420 nm thickness. The current-voltage characteristics are non-linear throughout the entire 20 V range. Figure 4.28(left)(inset) shows the ±2 V range; hysteresis is visible in this voltage range because the conductance is so low. Figure 4.28(right) shows the time evolution of the non-linear current-voltage characteristics over a 5 hour period. During this time, the current at +10 V decreased from 56 nA to 28 nA with an approximate resistance change from 358 MΩ to 172 MΩ. Non-linear current-voltage curves were only observed in thick films. The non-linearity is decreasing with time and this evolution of the non-linearity of I(V) curves as the films oxidize is shown in Figure 4.29. Following a one day period of oxidation in vacuum the current voltage characteristics of Sample 92 showed a slight non-linearity, consistent with similar films. After another three days in vacuum, the measurements were repeated and the I(V) curve was now linear. This effect is further investigated with carrier concentration measurements in §5.2.4.

[4]Films were subsequentially shown to be n-type

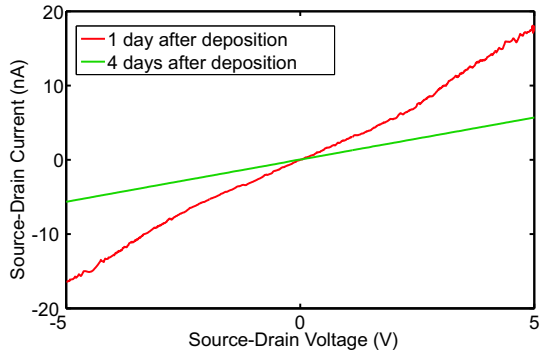

Figure 4.29: Evolution of current-voltage characteristics of Sample 92 over three days.

Current-Voltage Characteristics at Low Temperature

The resistance observed with temperatures below 200 K was always very high, an example shown in Figure 4.25. Due to that, no meaningful current-voltage characteristics were observed. An example is shown in Figure 4.30 which shows the characteristics for Sample 5 at 77 K and are very similar to the pre-onset characteristics shown in Figure 4.27(left). (For comparison, Sample 5 at 290 K is shown in Figure 4.27(right).)

The steps in I(V) curves observed in the literature for germanium cluster films ([131]/§4.1.6) were not observed. The films from [131] are different in a number of ways. The clusters are much smaller (4 nm diameter), the resistivity is much lower and the current is measured orthogonally to the substrate (see Figure 4.9(a)), so the number of clusters between the contacts is far less than in this project. The properties of germanium films studied here can not be directly compared to the work by Banerjee.

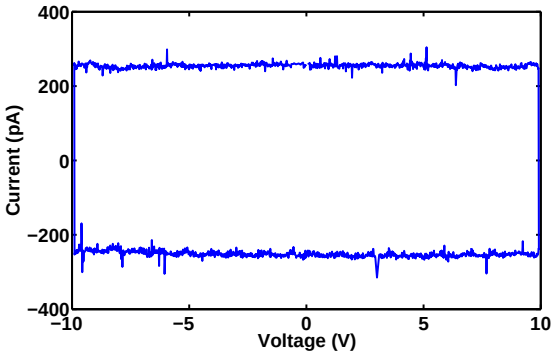

Figure 4.30: Current voltage characteristics of Sample 5 at 77 K.

4.6 Review and Conclusion

In this chapter a germanium cluster source was successfully designed, characterized and then used for deposition of basic cluster devices.

Once a reliable filament and nozzle configuration was able to produce a high flux of germanium clusters, cluster size and structure were probed with electron microscopes. Clusters were determined to be single crystal with a diamond structure with a thin oxide shell.

Percolation style samples were used to perform basic electrical characterization of germanium films. The onset of conduction was a gradual process when compared with previous materials studied using this system. The oxidation of films of germanium clusters was a dominant feature of the electrical characterization, causing the resistance and current-voltage characteristics to change over time. All films showed high resistance at room temperature, and when cooled to 77 K, no meaningful electrical data was observed due to the resistance increase. It was difficult to get any electrical data for films with thicknesses less than 200 nm because of the high resistivity of the cluster devices. The bandgap of germanium films was measured to be between 0.25 and 0.7 eV.

Current voltage characteristics were typically linear, with hysteresis appearing for very high resistance films. Non-linear current voltage characteristics observed for some thicker films became increasingly linear over time as the films oxidized in vacuum.

This chapter has described the basic electrical characterization of germanium cluster films. It is desirable to perform Hall measurements and gated measurements on germanium devices and these are investigated in the following chapter.

Chapter 5

Properties of Germanium Cluster Devices

In the previous chapter, a germanium cluster source was produced and used to deposit germanium cluster films for basic electrical characterization. The next step was to investigate the properties of germanium cluster devices.

In this chapter the properties of films of germanium clusters are studied using Hall measurements, gate measurements and by using a gas sensor test rig. Initially, §5.1 presents a review of gas and humidity sensors. The carrier concentration of germanium films is investigated with Hall measurements in §5.2. The effect of applying a gate bias to films of germanium clusters is then discussed in §5.3. The properties of germanium films when exposed to air are described in §5.4. Films of germanium clusters are then utilized as humidity and hydrogen sensors in §5.5 and §5.6 respectively. Conclusions and outlook are provided in §5.7.

5.1 Review of Gas and Humidity Sensors

Two common applications of semiconducting materials are to be used as gas [139] and humidity [140] sensors. Sensitivity to humidity and gases was first reported in germanium by Bardeen [141] in 1953. §5.1.1 discusses the properties of germanium oxide. Reviews of gas (§5.1.2-5.1.4) and humidity (§5.1.3) sensors then follow.

5.1.1 Oxides of Germanium and Silicon

Both germanium and silicon naturally form electrically insulating oxide layers in air [142]. Germanium can form either germanium oxide, GeO, or germanium dioxide, GeO_2. GeO is a dark-brown crystalline material which is unstable above 700°C where it disassociates into Ge and GeO_2 [143]. The oxide chemistry of germanium

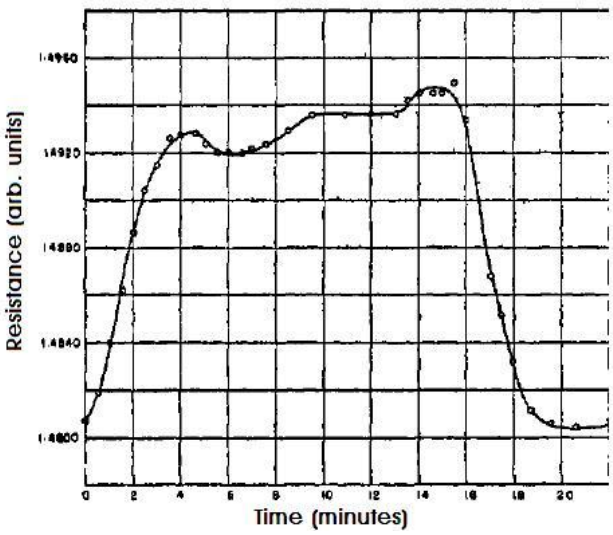

Figure 5.1: Germanium rod response to oxygen [148]. From t = 0 minutes to t = 13 minutes, the sample was exposed to dry oxygen. From t = 13 minutes to t = 22 minutes the sample was exposed to wet oxygen.

and silicon are similar with all three crystal forms of SiO_2 (quartz, hexagonal and vitreous) having equivalent forms in GeO_2 [144]. However, GeO_2 is far less chemically stable than SiO_2. SiO_2 is chemically inert (can be etched by hydrofluoric acid) whereas GeO_2 is soluble in water and this is considered one of the major factors as to why silicon is used in microprocessors today over germanium. Germanium films in vacuum show only surface oxidation (rather than becoming fully oxidized) for temperatures below 450°C [145]. However, further oxidation is possible and occurs exponentially faster for higher temperatures.

The resistivity of GeO_2 is very close to insulating, but thin films (15-200 nm) have been measured between sandwich electrodes to have resistances of $\sim$100 GΩ [146]. In the case of liquid GeO_2, the conductivity was measured over a range of temperatures (well above 300 K) and found to be of the order of $10^5\Omega$cm [147]. Therefore, room temperature germanium oxide can be treated as an insulator.

5.1.2 Semiconductor Gas Sensors

Semiconducting gas sensors have been used to detect a large number of gases[1]. The response is defined as:

$$Response = \frac{Resistance_{final} - Resistance_{initial}}{Resistance_{final}} \tag{5.1}$$

[1]Hydrogen [149], carbon monoxide [150], carbon dioxide [151], oxygen [152], ozone [153] as well as many others [154].

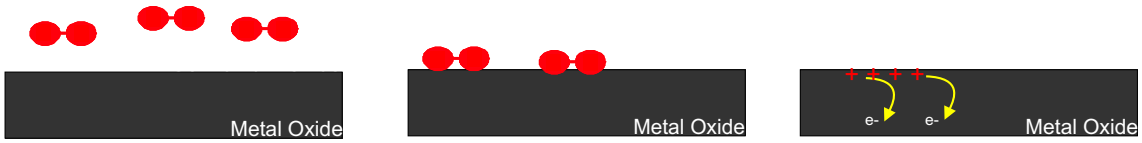

Figure 5.2: Schematic of the interaction of a reducing gas with an n-type metal oxide film. A reducing gas is introduced to the test chamber and interacts with the surface. Reduction occurs at the surface of the film and additional electrons are able to contribute to conduction; an increase in current is observed.

The gas can be detected using a change in device resistance [155], change in device capacitance [156], via frequency response [157], changes in Schottky-barrier heights [158], changes in Fermi energy [159] and work function [160]. The sensitivity of gas sensors can be affected by sensor temperature [161], film thickness [162], grain size [163] and others [89].

Semiconducting Gas Sensor Standard Mechanism

Sensors typically consist of a gas-sensitive film, a substrate with electrode and a heater [164]. There is a standard mechanism for semiconducting metal oxide gas sensors [154]. This standard mechanism is illustrated in Figure 5.2. There are four stages to the gas sensing process. First, a reducing gas is introduced to the to sensor and then it can become adsorbed on the surface of the sensor. When a reducing molecule (eg CO, H_2) is adsorbed on the sensor surface, reduction can occur and a surface defect is created. The defect acts as a donor which is ionized at the operating temperature of the sensor. The donor can act in two ways to change the sensor conductivity: either electrons becomes available from the donor which can contribute to conduction or the positive charge of the donors act as a gate and draws electrons from the contacts. Typically, both mechanisms are experimentally indistinguishable.

Because both mechanisms increase the number of electrons in the film, p and n-type devices have opposite conductivity changes for the same gas [89]. The inverse conductivity change is due to the different dominant charge carrier type in an n/p-type material. For an n-type device, a resistance decrease is observed for a reducing gas.

5.1.3 Semiconductor Humidity Sensors

Semiconducting films have been utilized as humidity sensors. The amount of water vapour present in a carrier gas is typically measured using units of relative humidity, defined as the ratio of partial pressure of water vapour to the saturation vapour pressure [140].

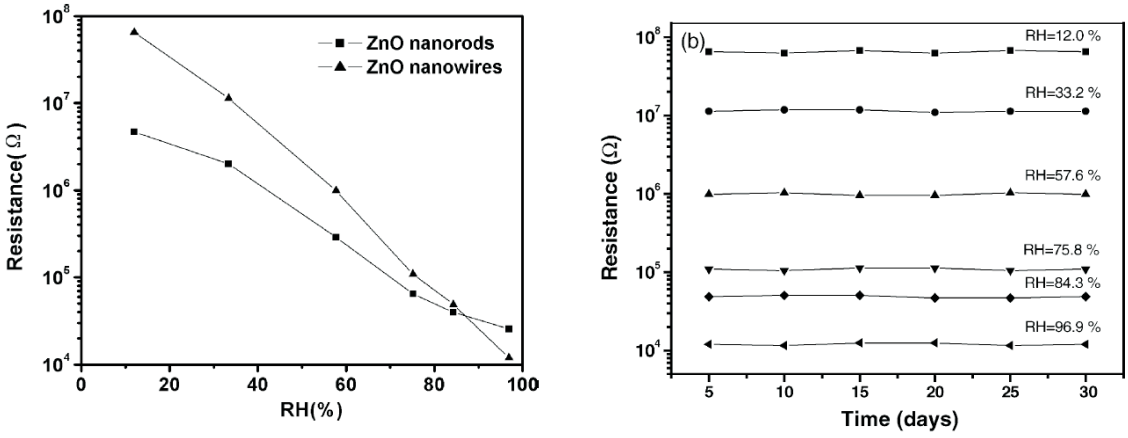

Figure 5.3: Relative humidity vs. DC resistance plots at 25°C for zinc oxide nanorods and nanowires [165].

Figure 5.3(left) shows the humidity response of zinc oxide [165]. The resistance of zinc oxide sensors changes by four orders of magnitude over a range of relative humidities between 10% and 99%. The resistance response to relative humidity of the sensors is relatively stable over time, as shown in Figure 5.3(right).

The surface of a semiconductor (or insulator) can react with or adsorb molecules from its environment, which can lead to a change in the conductivity [167]. There are several proposed mechanisms for the conductivity change in the presence of humidity, including surface conduction and addition of electrons into the film from donors. Both cases are considered in this section as germanium oxide can potentially act as an insulator or a wide bandgap semiconductor.

Figure 5.4 shows the schematic of two possible mechanisms for n-type conductivity change for water vapour adsorption. Electrons can be attracted by the adsorbed water molecules to the semiconductor surface and the energy bands bend or electrons are released by the competitive adsorption [166].

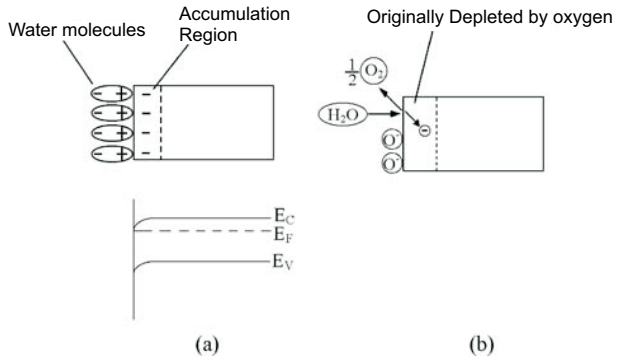

Figure 5.4: Two possible mechanisms for the n-type change in conduction with humidity: (a) Electrons are attracted by the adsorbed water molecules to the semiconductor surface and the energy bands bend; (b) Electrons are released by the competitive adsorption [166].

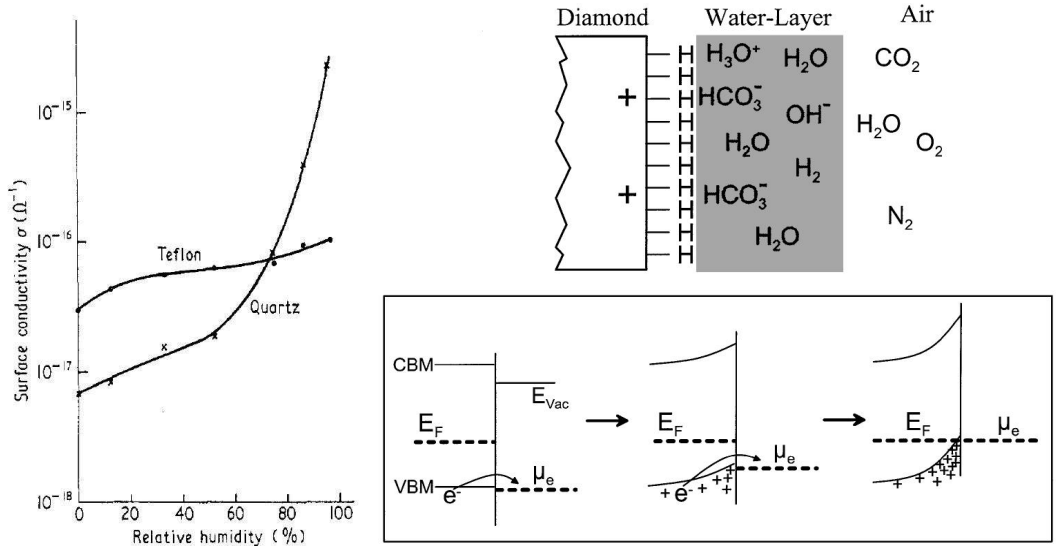

Figure 5.5: Left: Surface conductivity of Teflon and quartz as a function of humidity at 23°C [170]. Right: Top: Schematic picture of the hydrogenated diamond surface in contact with a water layer as it forms in air. Bottom: Evolution of band bending during the electron transfer process at the interface between diamond and a water layer [171].

The surface of insulators can also adsorb water vapour and this can significantly change the measured conductance. The surface conductivities of the large bandgap insulators quartz (9 eV [168]) and Teflon (8.5 eV [169]) are affected by the relative humidity [170]. The surface conduction was limited by the wetting angle of water droplets on the surface. Teflon is well known for its hydrophobic properties [169] which means water droplets have a high wetting angle. Therefore, Teflon is less affected than quartz by increased humidity, as shown in Figure 5.5(left). The mechanism is *proton* conduction, where H_3O^+ ions act as charge carriers with conduction occurring on the surface.

For narrower band gap insulators, a band bending mechanism has been suggested [171]. Hydrogen-terminated diamond (5.5 eV) can react with a water layer in the

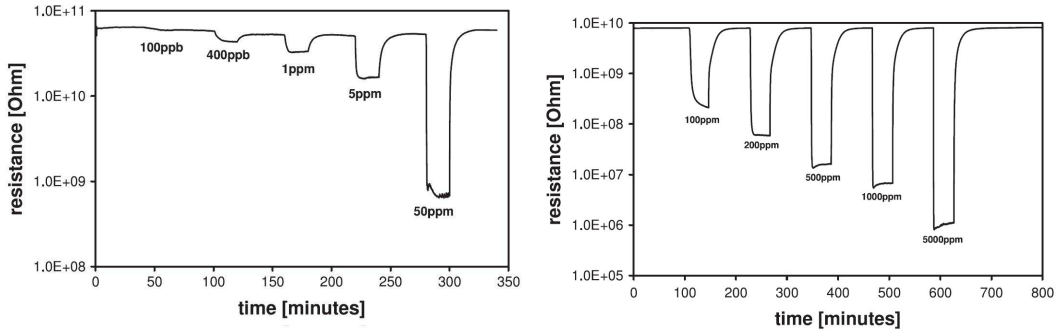

Figure 5.6: Tin-dioxide cluster-film response to varying concentrations of (Left) ammonia and (Right) hydrogen [25].

following reaction [172]:

$$2H_3O^+_{(water-layer)} + 2e^-_{(donated\,from\,film)} \rightleftharpoons H_2 + 2H_2O \tag{5.2}$$

The band bending is shown in Figure 5.5(right bottom). Electrons are donated from the valence band, which react with H_3O^+ ions in the water layer to create water and hydrogen (see Equation 5.2).

The Effect of Ambient Atmosphere on Germanium Conductivity

When water vapour is introduced to germanium rods of 2 mm length in an oxygen atmosphere, the resistance decreases until the water vapour is removed [141]. The increase and decrease are approximately exponential with the resistance measured over four minute periods. The observed change in resistance was up to 40%. When samples have been cleaned of any oxide in situ and then exposed to dry oxygen, the resistance increases rapidly over five minutes [148]. The increase is due to the oxidation of germanium. After oxidation, when germanium samples have been exposed to wet oxygen, a decrease in resistance to a value greater than the original has been observed, shown in Figure 5.1. This resistance decrease was attributed to water vapour creating donors on the surface oxide, the type of donor was not specified.

Different gases have different effects on the conductivity. When oxidized germanium has been exposed to wet nitrogen the resistance of the samples decreased by an order of magnitude compared to wet oxygen [173]. Germanium exposed to nitrogen which has been bubbled through OH groups (methanol or acetic acid) showed the same response as wet nitrogen whereas ozone or peroxide increased the resistance suggesting that oxidation was occurring, not reduction.

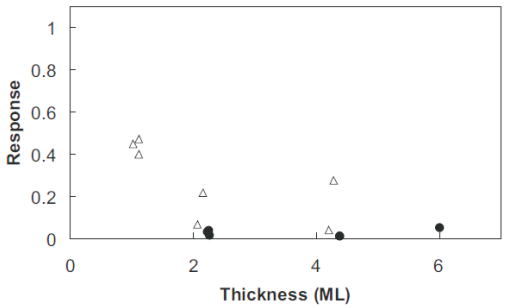

Figure 5.7: Response as a function of film thickness for tin oxide cluster sensors at 500 ppm hydrogen concentration. ML = monolayer, dots and triangles represent different cluster sizes [28].

5.1.4 Gas Sensing Behaviour of Cluster Films

Previously at Canterbury, films of percolating clusters have been used as ammonia sensors [25] and hydrogen sensors [24, 28].

Tin dioxide clusters have been used as hydrogen and ammonia sensors [25, 28]. Tin dioxide is a well known metal-oxide semiconductor with gas sensing capabilities [174]. The sensors work via the mechanism described in §5.1.2. The sensors have shown sensitivities to hydrogen concentrations of 100 ppm and for ammonia of 100 ppb. The responses are shown in Figure 5.6 and have shown higher sensitivities for thinner films [28], shown in Figure 5.7.

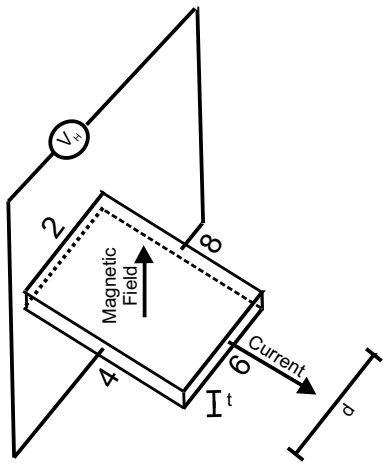

Figure 5.8: Schematic of Hall effect. V_H = Hall voltage, t = film thickness, d = film width. Numbers correspond to contacts from Figure 5.9.

5.2 Hall Measurements of Germanium Clusters

This section describes the Hall measurements performed on germanium cluster films that have been used to determine the sign and quantity of charge carriers. Initially, the Hall effect and experimental technique are reviewed. Hall effect results are then discussed and, finally, the variation in carrier concentration as a function of temperature is assessed.

5.2.1 Review of Hall Effect

The Hall effect can be used as a tool for determining the carrier concentration in a semiconductor. The geometry of the Hall effect is shown in Figure 5.8. The Hall effect is observed in a conductor when a magnetic field perpendicular to current flow produces a Lorentz force to create a distribution of charges across the sample. The charge distribution creates the so-called Hall voltage, V_H, which defines a Hall Resistance, R_H:

$$V_H = R_H i \tag{5.3}$$

where i is the current and is related to carrier concentration, n, and the magnetic field via[2]:

$$R_H = \frac{B}{qtn} \tag{5.4}$$

where t is the thickness of the material and B is the magnetic field. It follows from Equations 5.3 and 5.4 that the carrier concentration can be determined from the measurement of the Hall voltage. It should be noted that the sign of the Hall voltage

[2]The Hall voltage and Hall resistance are sometimes equivalently defined as $V_H = \frac{-iB}{tne}$ and $R_H = \frac{-1}{ne}$.

will reveal if electrons or holes are the dominant charge carrier, so the orientation of all contacts should be carefully noted at all times. Traditionally, the Hall resistance is negative if electrons are the dominant carrier. Further details of the Hall effect can be found elsewhere [78].

The mobility, μ, of charge carriers can be determined using the Hall resistance and conductivity:

$$\mu = |R_H|\sigma \tag{5.5}$$

However, Equation 5.5 only holds when there is significantly more of one type of carrier. In the case where both electrons and holes have a significant contribution to conduction, the Hall resistance is related to mobility via [78]:

$$R_H = \frac{n_h\mu_h^2 - n_e\mu_e^2}{q(n_h\mu_h - n_e\mu_e)^2} \tag{5.6}$$

It follows from Equation 5.6 that carrier mobility is far more difficult to determine in near-intrinsic samples using this method.

5.2.2 Hall Sample Experimental Technique

Figure 5.9(left) shows the photolithographically defined Hall sample with the contacts labelled. In order to achieve the geometry outlined in Figure 5.8, substrates were produced using the sample design shown in Figure 5.9(right). This sample design is identical to that used by Ayesh [29]. However, the substrates used in this project were Si/Si_3N_4 rather than Si/SiO_2. The fabrication techniques of these samples are detailed in §2.3. The mask shown in Figure 5.9(middle) is used to define a photoresist passivation layer to ensure that any conduction measured is from the $200\,\mu m \times 1000\,\mu m$ film. Clusters were deposited using the IGA source as described previously (§4.3). The typical circuit setup had current flowing between contacts 2

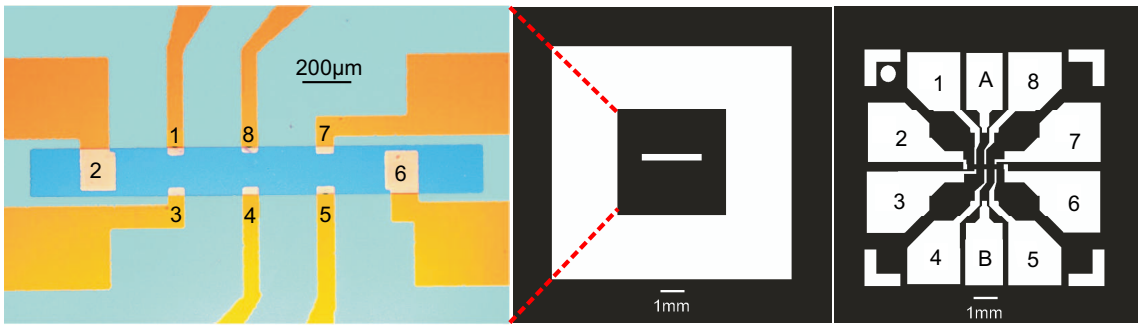

Figure 5.9: Hall Sample setup. Left: Optical microscope image of Hall Sample prior to deposition [29]. Numbers correspond to electrical contacts referred to in the text. Middle: Schematic of mask layer used to provide the passivation layer of photoresist. Right: Schematic of Hall sample layout fabricated using photolithography.

and 6, a magnetic field into the page and a Hall voltage measured between contacts 8 and 4 (or two other parallel contacts).

In order for Hall measurements to be performed, a magnet in the deposition chamber was required. Two permanent magnets were attached to a linear translator which could be positioned over the sample at will. The two magnets have a magnetic field of 0.3 T [29]. The magnets block the front of the substrate so Hall measurements can only begin after cluster deposition is complete.

5.2.3 Overview of Germanium Device Behaviour

Figure 5.10 shows a schematic overview of the change in current with time over the lifetime of a germanium sample. Each region is discussed with respect to Hall samples within this chapter. There are 7 stages of interest. Region 1: During cluster deposition a current increase is observed (§4.3.3). Region 2: Oxidation in vacuum, where current decrease is attributed to oxidation (§4.3.4). Region 3: Where the oxidation in vacuum has largely stopped and consistent measurements can be performed. Region 4: As the sample is exposed to air the current increases (§5.4). Region 5: Sample in air with stable resistance. Region 6: Where the pressure is

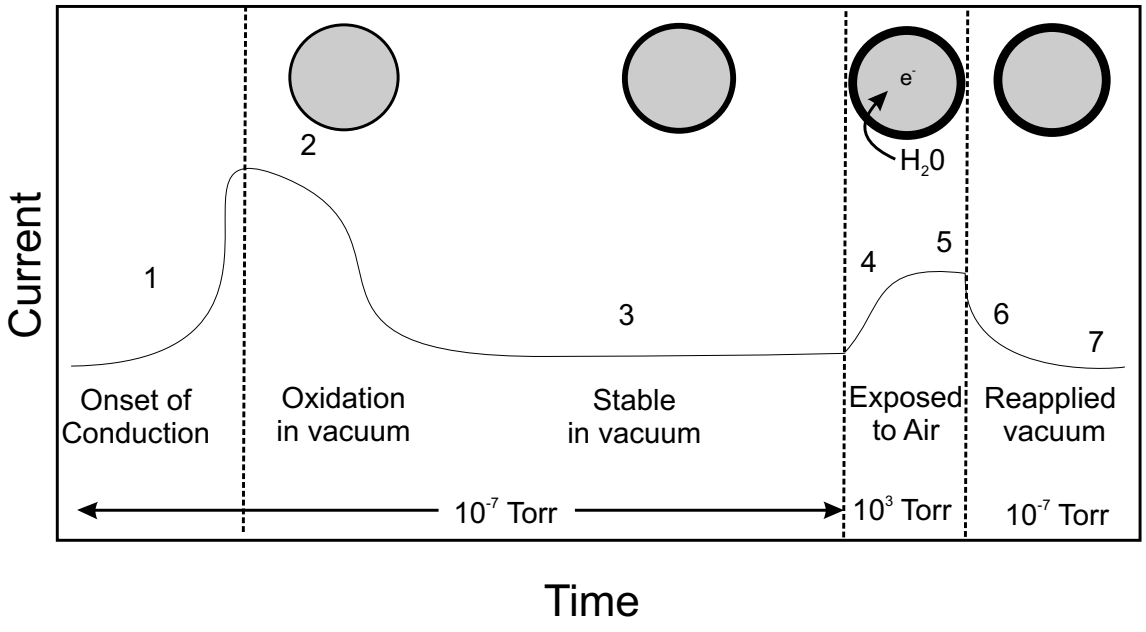

Figure 5.10: Schematic overview of the change in current with time over the lifetime of a germanium sample. Shown are 7 regions of interest. Region 1: During cluster deposition a current increase is observed. Region 2: Oxidation in vacuum, where current decreases that is attributed to oxidation. Region 3: Where the oxidation in vacuum has largely stopped and consistent measurements can be performed. Region 4: As the sample is exposed to air the current increases. Region 5: Sample in air with stable resistance. Region 6: Where the pressure is decreased and the current has a corresponding decrease. Region 7: Where resistance has stabilized in vacuum. Inset: Schematic of the progress of the oxidation of germanium clusters.

Hall Sample	Film Thickness	Carrier Concentration in region 3	Notes
1	550 nm	-	No Hall voltage
2	410 nm	-	No Hall voltage
3	465 nm	-	No Hall voltage
4	550 nm	$6\times10^{12}\text{cm}^{-3}$	
5	500 nm	$4\times10^{12}\text{cm}^{-3}$	Figure 5.18
6		-	Gate Leak
7		-	Gate Leak
8	430 nm	$7\times10^{12}\text{cm}^{-3}$	
9		-	Gate Leak
10		-	Gate Leak
11	300 nm	$4\times10^{13}\text{cm}^{-3}$	Figure 5.16
12	500 nm	-	No Onset
13	630 nm	$2\times10^{13}\text{cm}^{-3}$	Figure 5.16
14	470 nm	$2\times10^{12}\text{cm}^{-3}$	
15	370 nm		No Onset
16	180 nm	-	No Hall voltage
17	300 nm	-	No Onset
18	400 nm	-	No Hall voltage
19		-	No Onset
20	500 nm	$2\times10^{13}\text{cm}^{-3}$	
21	550 nm	$1\times10^{13}\text{cm}^{-3}$	Figures 5.11-5.14 and 5.19

Table 5.1: Details of Hall Samples.

decreased and the current has a corresponding decrease. Region 7: Where resistance has stabilized in vacuum. The insets of Figure 5.10 show schematics of the progress of the oxidation of germanium clusters. Figure 5.10 and regions 1-7 are referred to throughout this chapter.

5.2.4 Hall Effect Results

Most of the results presented in this and the following sections are taken from Hall Sample 21. Hall Sample 21 was the most consistent and successful sample, provided the most complete data set and avoided most of the charging effects that are described below.

Problems with Hall Measurements

As determined in Chapter 4, devices made from germanium clusters have high resistivity and in order to achieve a large measurable current the films have to be deposited in excess of the percolation threshold. Even films of several hundred nanometres thickness can still have resistances of hundreds of MΩ. However, because most of the Hall samples had large thicknesses, many also showed non-linear I(V) characteristics. Therefore the resistances at low voltages were typically much higher, of order GΩs. This had consequences that when an attempt was made to measure a Hall voltage in zero field, the voltmeter treated the signal as an open circuit and produced noisy data, presumably through the voltmeter input changing range to pick-up a signal. If the expected Hall voltage is small, then the voltmeter noise level is larger than the signal making measurements difficult. The voltmeter would occasionally pick up the correct signal, and then revert to the voltage range charging behaviour. This problem was overcome by increasing the source-drain

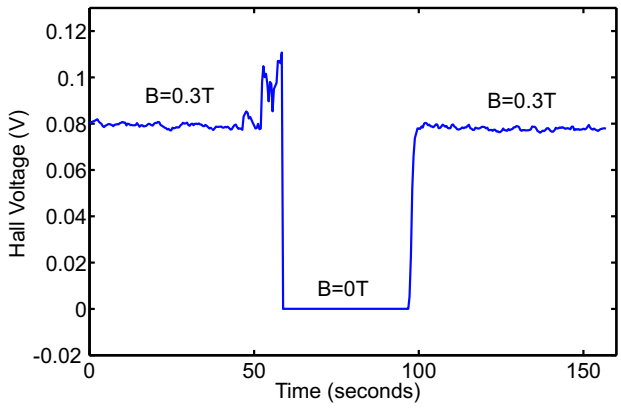

Figure 5.11: Measurement of Hall voltage for Hall Sample 21 after 9 hours of oxidation in vacuum.

voltage to increase the current and enhance the Hall voltage signal (Equation 5.3).

Hall Sample 21

Figure 5.11 shows the Hall voltage measurement of Hall Sample 21 at zero gate bias in region 3 from Figure 5.10. At 50 seconds the sample is removed from the magnetic field and the Hall voltage drops to $\sim$0 V. With a current of 230 nA, and film thickness of 500 nm, the corresponding carrier concentration is $1\times10^{13}\text{cm}^{-3}$. This carrier concentration is the same order as the carrier concentration of undoped bulk germanium Table 4.1/[43]. The sign of the Hall voltage reveals that the dominant charge carriers are electrons, hence the device is n-type. This measurement was taken 9 hours after deposition with the sample still in vacuum. The carrier concentration at the start of region 3 was typically in this range (when a Hall voltage could be measured), other results are listed in Table 5.1.

As the sample slowly oxidizes while in vacuum, the carrier concentration changes, an effect discussed in §5.3.1. The carrier concentration also changes with an applied gate bias, an effect that is discussed in §5.3.

5.3 Gate Effect in Germanium Clusters

Once the Hall measurement technique had been established as reliable the next logical experiments were to investigate the effect of a gate bias on germanium devices. Attempts were made to observe transistor-like behaviour by applying a backgate bias to Hall samples, enabling information about the carrier concentrations to be recorded.

This section investigates the gate effect in Hall samples of germanium clusters. Samples were backgated as in Figure 2.9 (right). §5.3.1 discusses how the gate effect varies during the initial oxidation stage (region 2 from Figure 5.10) and then §5.3.2 shows further evolution of the gate effect in regions 3-7 from Figure 5.10.

5.3.1 Evolution of Gate Effect with Oxidation

This subsection describes the gate effect of Hall sample 21 in the first eight hours after deposition when the sample is in region 2 from Figure 5.10. Carrier concentration, Hall resistance and film resistance were all monitored as a function of time and gate bias.

Directly after deposition of Hall sample 21 had ended, the sample was positioned into the magnetic field and Hall measurements were recorded during the oxidation in vacuum of the sample (region 2 of Figure 5.10). During the oxidation the gate bias was ramped in the $\pm 50\,\mathrm{V}$ range enabling simultaneous gate and Hall measurements. Figure 5.12 shows the change in carrier concentration in the eight hours after deposition. Figure 5.13 shows the change in Hall resistance and film resistance over the same time period. Over the 8 hours, the zero-bias carrier concentration decreases from $2.8\times10^{13}\mathrm{cm}^{-3}$ to $1\times10^{13}\mathrm{cm}^{-3}$. As expected from an oxidative process, the carrier concentration decreased over time as more carriers become unavailable to contribute to conduction. Figure 5.13 shows the zero-bias film resistance increased from $25\,\mathrm{M}\Omega$ to $65\,\mathrm{M}\Omega$ and the Hall resistance from $135\,\mathrm{k}\Omega$ to $400\,\mathrm{k}\Omega$.

The effect of gate bias is now also considered. The changes in carrier concentration observed in Figure 5.12 are caused by a combination of three factors: Oxidation, changes attributed to the gate bias (the real gate effect) and capacitive effects due to the gate bias ramps, which are explained below.

In Figure 5.12 (bottom left) there is a trend that the carrier concentration decreases over the first 100 minutes. On the shorter timescale of a single gate ramp, the change in carrier concentration follows the ramp of the gate bias so that when the gate bias is ramping up, the carrier concentration also increases, and vice versa for the ramp down. This apparent change in carrier concentration is attributed to capacitive charging, caused by the ramp rate of the gate bias (capacitive effects are

discussed in §2.4.2). At this early stage of oxidation the capacitive charging affects the Hall voltage measurement far more significantly than the film resistance. Figure 5.13 (bottom left) shows the Hall resistance changes as a function of gate bias but the film resistance is only effected by oxidation. However, after an additional four more hours of oxidation (Figure 5.13 (bottom right)), the change in carrier concentration in the region when the gate bias is constant starts to become more significant.

The following describes the behaviour observed in Figure 5.12(bottom right). A consistent decrease in carrier concentration is observed over the period where gate bias is held at 50 V and this is attributed to oxidation. As the gate bias ramps down to 0 V, a faster decrease of the carrier concentration is observed, and this is attributed to the combination of the decreasing gate bias and oxidation. At zero gate

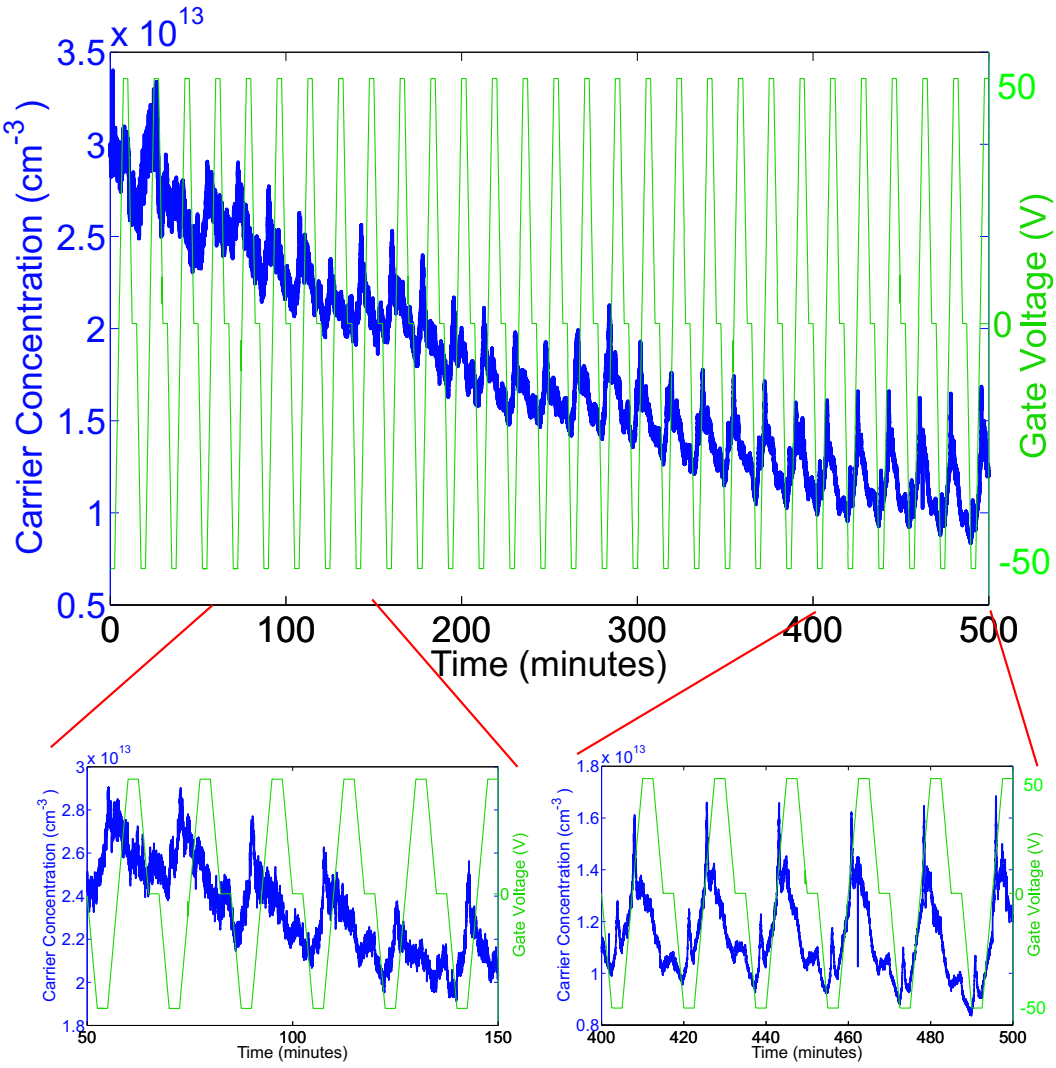

Figure 5.12: Evolution of the gate effect for Hall sample 21 showing variation in carrier concentration with time and gate bias.

bias, there is a clear decrease in carrier concentration (increase in Hall resistance) with time, with a decrease across measurements also being observed. At -50 V gate bias a spike in carrier concentration occurs. This is attributed to the capacitive charging effect and the sudden stop in gate-voltage ramp which then allows the carrier concentration to recover to the true -50 V value. It appears towards the end of the experiment the carrier concentrations for -50 V and 0 V gate biases are not significantly different, but that the carrier concentration is enhanced for positive gate biases. The dominant effect is capacitive charging but at each of the regions of constant gate bias, the real gate effect and oxidation effects can be observed.

Overall, at the start of the oxidation (Figure 5.12(bottom left)) the charging effect is dominant and the carrier concentration follows the ramp of the gate bias.

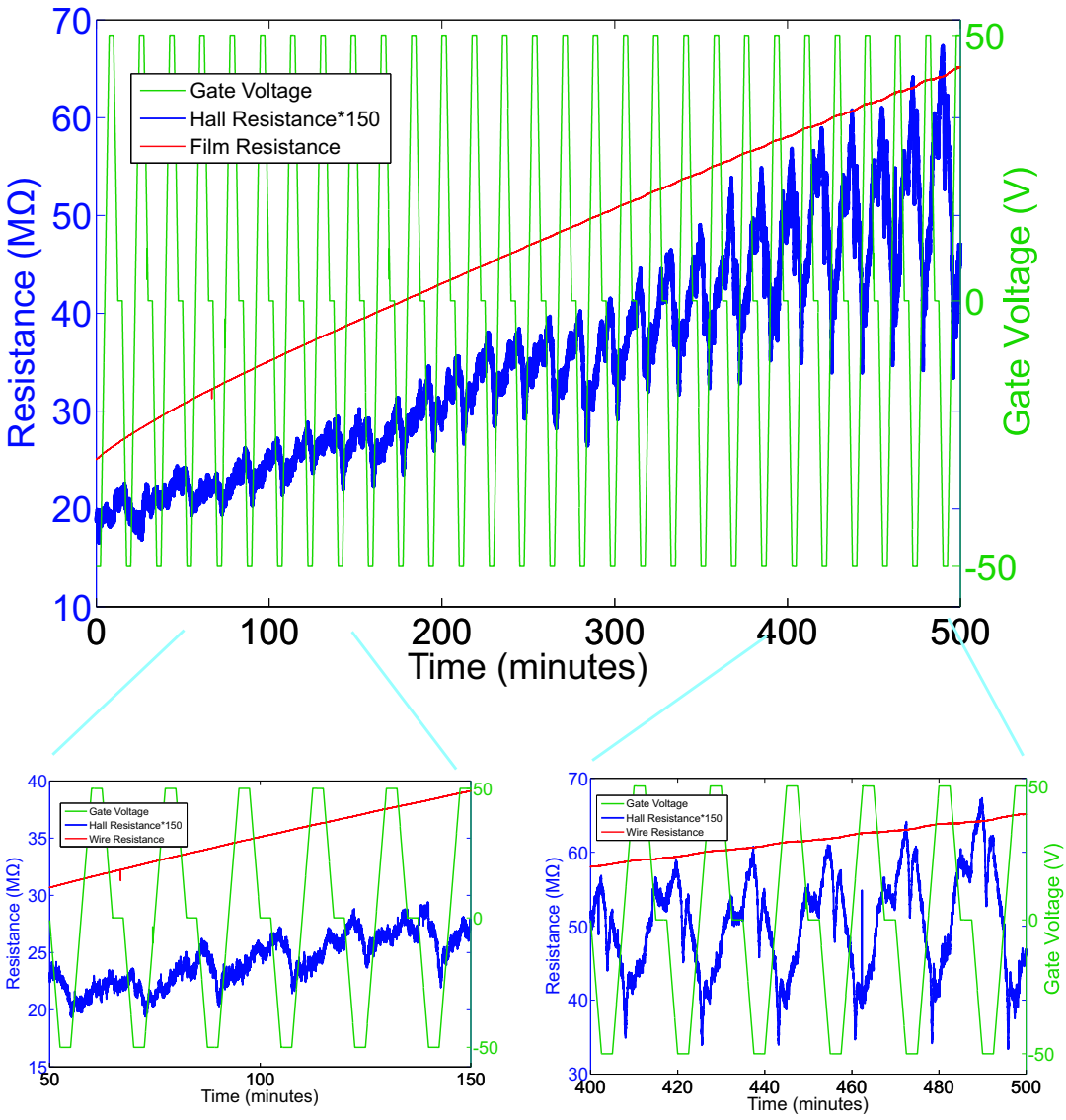

Figure 5.13: Evolution of the gate effect for Hall sample 21 showing variation in film and Hall resistance with time and gate bias.

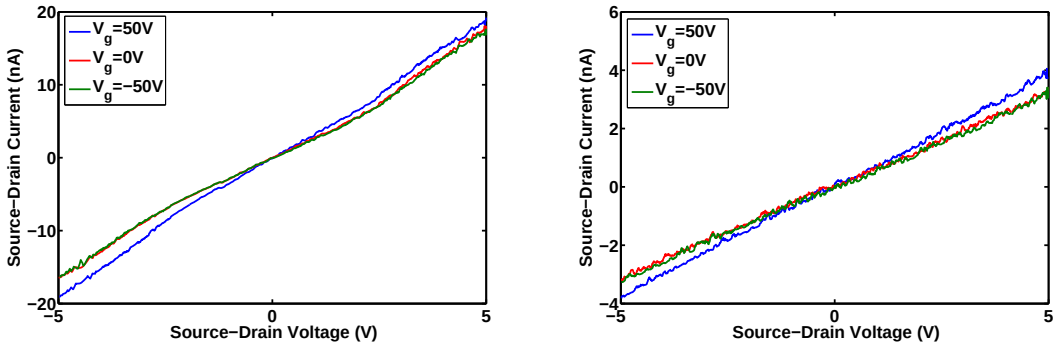

Figure 5.14: Gate bias data as a function of current-voltage characteristics for Left: 9 hours after deposition. Right: 57 hours after deposition.

However, after 400 minutes the change in carrier concentration due to constant gate bias (the actual gate effect) starts to become more significant. This is apparent in the film resistance beginning to change as a function of gate bias after 400 minutes. However, the greatest effect occurs when the gate bias is ramping, the capacitive charging effect, so the gate effect is not clearly observable. The gate effect is further investigated for region 3, in the next subsection.

5.3.2 Gate Effect in Germanium Films in Region 3

Now that the resistance of Hall Sample 21 was reasonably stable (region 3 from Figure 5.10), individual gate measurements were possible.

The gate effect in this subsection is presented using two types of graph. Source-drain current is plotted as a function of either source-drain voltage or gate voltage.

Figure 5.15 shows the gate dependent change in current in region 3 for an source-drain offset of 5 V in the ±50 V gate bias range. The gate effect is linear in the -50 V to +25 V range with a non-linear section observed for gate bias values above 25 V where additional current enhancement occurs. This current enhancement is small compared to the 7 orders-of-magnitude current enhancement observed in typical germanium FETs from the literature (§4.1.5), despite the devices in this project having gate biases ten times larger.

The mobility can be extracted from Figure 5.15 using the slope of the linear section using [2]:

$$\mu = \frac{dI_{ds}}{dV_{gs}} \frac{L^2}{C_{film} V_{ds}} \tag{5.7}$$

where L is the film length and C_{film} is the capacitance of the film. With a 200 nm thick silicon nitride dielectric, the capacitance of the film is 40 fF, leading to a mobility of 180 $V^2 m^{-1} s^{-1}$. This mobility value is roughly twenty times smaller than the electron mobility of bulk germanium but similar in comparison to nanosized

germanium transistors [100, 175].

Figure 5.14(left) shows the gate effect of Hall Sample 21 in region 3, directly after the oxidation measurements from §5.3.1. These measurements were performed by taking a standard I(V) measurement (as performed in §4.5), then repeating the measurement with different gate biases. This style of measurement was desirable as the capacitive charging effects due to changing gate bias observed in §5.3.1 were avoided.

The I(V) curves at all gate biases show a slight non-linearity. The plots for gate bias values of 0 V and -50 V show no significant differences between curves and this is consistent with the behaviour observed in region 2 from §5.3.1. The I(V) curve with a 50 V applied bias shows a current enhancement for positive source-drain currents and an equivalent decrease for a negative source-drain current.

The gate measurements were repeated two days later, just prior to the sample being vented to atmosphere. During this 48 hour period, the resistance increased due to oxidation, from ∼250 MΩ to 1.3 GΩ (at 5 V). The current-voltage characteristics are shown in Figure 5.14(right). The same gating behaviour is observed; the I(V) curves at 0 V and -50 V gate bias are equivalent and the curve for +50 V has a larger slope corresponding to a lower resistance. The data has higher noise levels due to the lower values of the current and corresponding larger signal-to-noise ratio. The non-linearity in the I(V) curves is no longer present, which is consistent with results from previous sections (§4.5.2) for non-linear current voltage characteristics.

The gate measurement shown in Figure 5.15 was recorded directly after the data shown in Figure 5.14. The non-linear section observed above +25 V gate bias is consistent with the additional current observed with the 50 V bias range in Figure 5.14. However, there is an observed decrease of 0.5% in the negative gate bias range and this decrease in the negative range is not reflected in the I_{sd}-V_g characteristics. This was a consistent effect between measurements and it is attributed to the failure

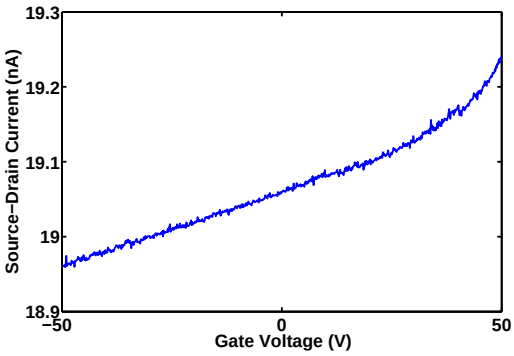

Figure 5.15: Gate data for Hall Sample 21 in region 3.

to properly correct for the capacitive charging effect described in the previous section (capacitive charging effect is the same because the same voltage ramp was used.)

Hall Sample 21 shows behaviour consistent with an n-type transistor, since a positive gate bias increases the conductivity of the film. This is also consistent with the Hall measurements from §5.2.4 revealing that the majority carriers were electrons.

Gated measurements were repeated after Hall Sample 21 was exposed to air and this is discussed in §5.4.2.

5.4 Germanium Films: Exposure to Atmosphere

In previous studies at Canterbury (§1.3.1), the device resistance has increased due to oxidative effects when cluster devices have been exposed to air. However, devices made from germanium clusters exhibited a decrease in resistance when vented to air. Typically, a sharp decrease in resistance was observed when the vent valve was opened, as shown for Percolation Sample 40 in Figure 5.16(inset top). However,

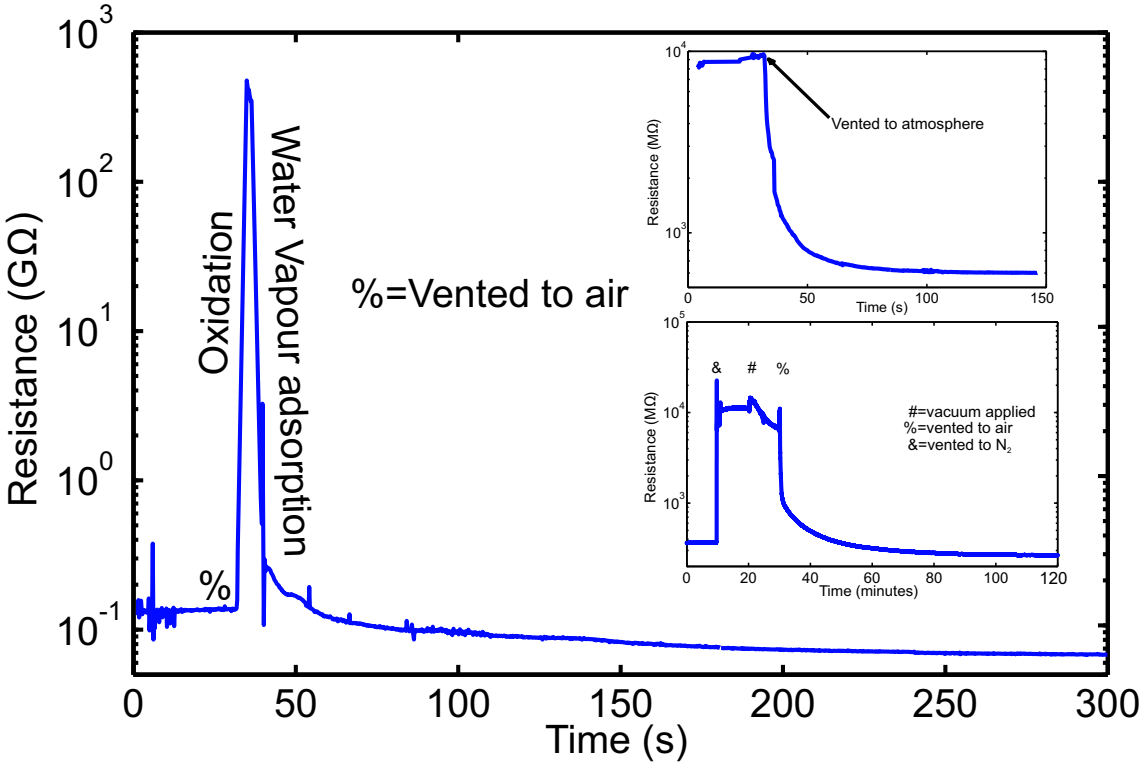

Figure 5.16: Oxidation of Hall Sample 11. Hall sample 11 was in high vacuum until t=30 s, when the vent valve is slowly opened, the resistance increases sharply before a sharp resistance decrease is observed. Inset Top: Percolation Sample 40, showing typical resistance decrease when sample is exposed to air. Inset Bottom: Hall Sample 13 oxidation. At t=10 minutes the sample is vented to dry 99%N_2/1%O_2 with an increase in resistance observed.

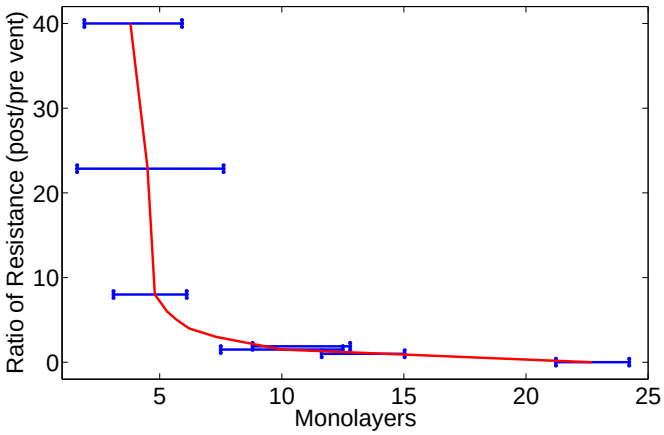

Figure 5.17: Germanium percolation film sensitivity to exposure to air as a function of film thickness. The ratio of resistance is defined as the resistance before exposure to air divided by the resistance after venting when the sample had stabilized. Each point represents a single germanium percolation sample. Red line is a guide to the eye.

Hall sample 11 was exposed to air at a slower than typical rate (Figure 5.16), which revealed a fast resistance enlargement process occurring over about ten seconds before the resistance reduction was observed.

Prior to the venting process at t = 30 seconds, the sample was in high vacuum with a pressure of 5×10^{-7} Torr. To expose the sample to air, the vent valve was opened and the pressure in the deposition chamber increased to ∼700 Torr over about sixty seconds[3]. During this time, the resistance of the sample increased quickly by over 3 orders of magnitude, before decreasing to less than the pre-vent resistance.

The change in resistance is attributed to two processes; oxidation and reaction with water vapour. When germanium films were kept in vacuum for a long time, (one week or more), the film resistance eventually increased until the resistance was too high to measure. When Hall Sample 11 was vented, 26 hours after deposition[4], the resistance decrease process was able to occur at a much faster rate as there are ∼10 orders of magnitude more oxygen available and therefore the large fast resistance decrease is attributed to oxidation.

The re-decrease in resistance of Hall Sample 11 appears to be caused by the presence of water vapour. This was further investigated by venting Hall sample 13 to dry $99\%N_2/1\%O_2$. Figure 5.16(inset bottom) shows that venting to a dry atmosphere with oxygen content only causes the resistance increase; the resistance decrease is not observed until the sample is exposed to air. A variation across samples in the percentage change in resistance was observed during exposure to air.

The variation in ratio of resistance is plotted as a function of the number of

[3]compared to the typical ten second venting time.

[4]Samples 13 and 40 were vented 2 and 1.5 hours after deposition, respectively.

monolayers in Figure 5.17 and shows that when germanium films are exposed to atmosphere, the resistance response depends on film thickness. A larger relative decrease in resistance is observed for thinner films. This is because the thinner films have a larger relative surface area and therefore are more sensitive to adsorption of water vapour. This behaviour is consistent with the humidity sensor sensitivity properties from §5.1.3. These results suggest that germanium clusters films could be utilized as humidity sensors and this is investigated in §5.5.

5.4.1 Carrier Concentration Change in Air

Using the Hall samples described in §5.2.2, the Hall voltage and carrier concentration were able to be determined as a function of ambient (regions 3-7 of Figure 5.10). Figure 5.18 shows the change in current, carrier concentration and Hall voltage in Hall Sample 5 while exposed to different atmospheres. Previous to t=17 minutes Hall Sample 5 was in vacuum. At t=17 minutes the vent valve was opened, exposing the sample to air. The current increased by more than an order of magnitude, consistent with the results from §5.4. A corresponding increase in carrier concentration was simultaneously observed. After a period of ten minutes, the sample was re-exposed to vacuum and a decrease in current and carrier concentration observed. After an additional ten minutes, a vent valve was opened exposing the sample to dry 99% nitrogen with a final pressure of 700 Torr. The current and carrier concentration show an increase but of much smaller magnitude compared to when vented to air; the carrier concentration in nitrogen was $3\times10^{12}\text{cm}^{-3}$ compared to $9\times10^{13}\text{cm}^{-3}$ for air. At t= 78 minutes, the sample is re-exposed to air and the carrier concentration recovers to the previous value observed in air. The data from Figure 5.18 shows that some non-nitrogen/oxygen part(s) of air are causing this decrease in resistance when the pressure is increased.

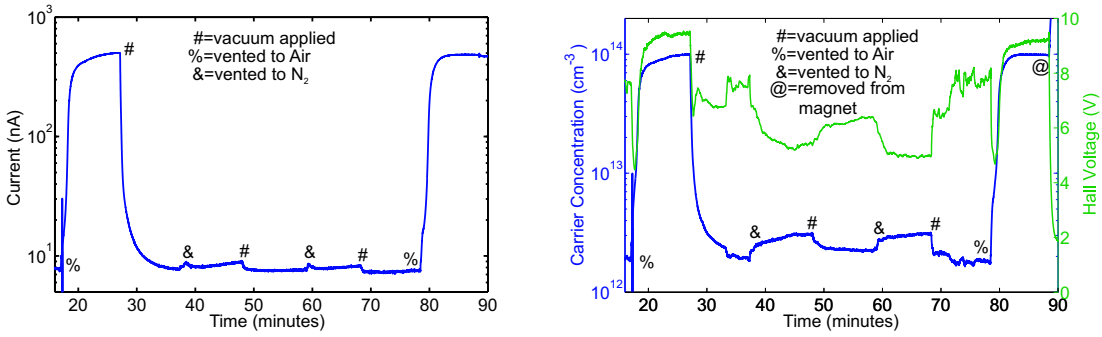

Figure 5.18: Hall Sample 5 exposure to different atmospheres. Every 10 minutes, the system was either pumped down or vented to either $99\%N_2/1\%O_2$ or normal air. Left: Current variation with atmosphere. Right: Variation of carrier concentration and Hall voltage with atmosphere.

5.4.2 Germanium Gate Effect in Air

After the film was exposed to atmosphere the gate runs of §5.3.2 were repeated and gated behaviour observed as shown in Figure 5.19 for Hall Sample 21. The post-venting (region 5 from Figure 5.10) I_{sd}-V_{sd} characteristics display equivalent behaviour as prior to venting. The magnitude of the gate effect has decreased; a comparison of the gate effects at different times is shown in Table 5.2. The smaller magnitude of the gate effect is attributed to a larger carrier concentration (as shown in §5.4.1), and the gate bias can only enhance the carrier concentration by a certain amount, so a smaller percentage increase is expected. Figure 4.6(e)/(f) is used for comparison to show that the size of the gate effect observed in this report is much smaller than when compared to Wang [100]. It is not possible to determine if the 50 V gate bias changes the carrier concentration by a constant amount because although the change in currents are different as listed in Table 5.2, the mobility could also be changing over time.

When Hall Sample 21 was re-exposed to vacuum (region 7 from Figure 5.10), the high resistance of the now fully oxidized film meant the signal-to-noise ratio was too high for any meaningful gate data to be observed. The reappearance of non-linearity in the current-voltage is correlated with the increase in carrier concentration. The cause of the non-linearity for samples with higher carrier concentrations was not determined.

5.5 Germanium Film Response to Humidity

In the previous section germanium clusters films were exposed to air and it was suggested that that ambient humidity was responsible for the observed decrease in resistance. This section demonstrates germanium cluster films as humidity sensors.

In this section the response of films of germanium clusters to different concentra-

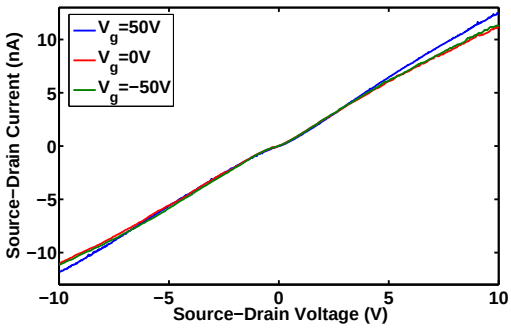

Figure 5.19: Gate bias data of Hall Sample 21 as a function of current-voltage characteristics after venting in region 5.

Elapsed time from deposition	Δi V_g=50 V	ΔR% at V_{sd}=5 V	vented	Figure
9 hours	1 nA	6%	no	5.14(left)
57 hours	0.45 nA	12%	no	5.14(right)
60 hours	0.2 nA	3%	yes	5.19

Table 5.2: Evolution of gate effect of Hall Sample 21 showing increase with oxidation and decrease with venting, change in current is for current-voltage value of 5 V and ΔR% is comparison of 50 V and 0 V gate bias.

tions of water vapour are investigated. Experiments are also carried out to determine how film response varies as a function of film thickness and sample age. Possible mechanisms for the observed change in resistance are then discussed. All humidity measurements were performed at atmospheric pressure (region 5 from Figure 5.10).

5.5.1 Sample Selection and Deposition

A series of percolating film samples (Figure 4.19) was deposited with different thicknesses and fixed source conditions. They were deposited with a source temperature of 1540°C and argon gas flow of 180 sccm. They are labelled GS (Gas Sensor) samples and are equivalent to the percolation style samples from §4.3. The source conditions were kept constant to maintain a consistent cluster diameter. Details of GS samples are shown in Table 5.3.

5.5.2 Gas Rig Setup

The gas rig (detailed in §2.2) had two operational modes: hydrogen sensing and humidity sensing. In the hydrogen sensing mode channel 1 was assigned as dry synthetic air (79% nitrogen/21% oxygen) and channel 2 was assigned to be forming gas (5% hydrogen/95% argon). For humidity sensing mode channel 1 was dry synthetic air and channel 2 was synthetic air that was bubbled through deionized water. The relative humidity was independently determined with a HTF3227LF humidity sensor. In the first hour of every experiment, dry synthetic air was kept at a constant flow rate to determine a baseline resistance. The circuit for detecting resistance was a two-terminal measurement of current with a constant 10 V source-drain offset voltage. Details of the LabView data acquisition and modification of existing gas rig setup for humidity measurements are described elsewhere (§2.2.2).

Sample #	1	2	3	4	5	6	7
Thickness	1.3 ML	3 ML	5.5 ML	1 ML	4.2 ML	6 ML	7.8 ML

Table 5.3: Details of GS samples deposited for gas sensing measurements. ML = monolayers.

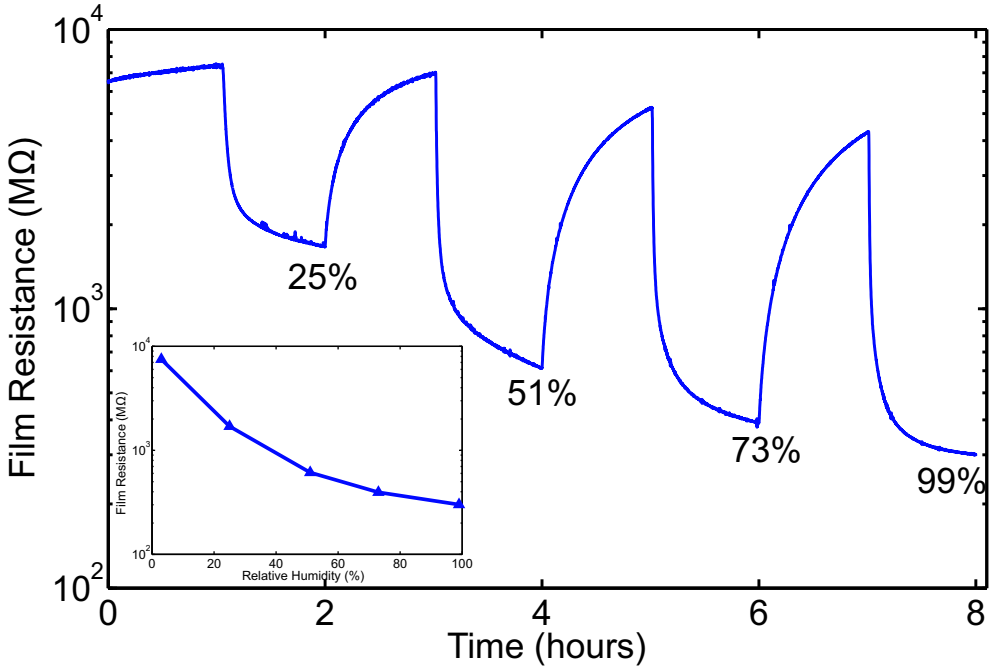

Figure 5.20: Typical response to various levels of relative humidity. Shown is sample GC2, a 3 ML sample deposited with a source temperature of 1540°C and argon gas flow of 180 sccm. Inset: Response of sample GC2 as a function of relative humidity.

Figure 5.20 shows a typical response of a germanium film to various levels of humidity. The resistance of GS sample 2 is shown for relative humidities of 25%, 51%, 73% and 99%. The resistance of GC2 reduces from 7.5 GΩ (at 10 V source-drain offset) to 300 MΩ at 99% humidity. The response is defined as:

$$Response = \frac{Resistance_{final} - Resistance_{initial}}{Resistance_{final}} \tag{5.8}$$

A sharp resistance decrease is initially observed when the flow is changed. The sensitivity of GC2 to water vapour is much greater than previously reported humidity responses for n-type germanium (Figure 5.1). Morrison [148] only observed a 40% change in conductivity, Lasser [176] only 80% (at 88% Relative humidity (RH)) with the typical sensitivity of films in this project being fifty times greater. The greater sensitivity is attributed to the much larger surface-to-volume ratio of the cluster films.

The data is presented in a different way in Figure 5.20(inset) showing a smaller film resistance for increasing relative humidity. When compared to Figure 5.3(left), the change in resistance is three orders of magnitude greater for zinc oxide humidity sensors. This illustrates that response of germanium cluster films is greater than for bulk germanium, but is less sensitive than some other humidity sensors.

When the samples were originally vented to air (§5.4), the humidity of the lab was

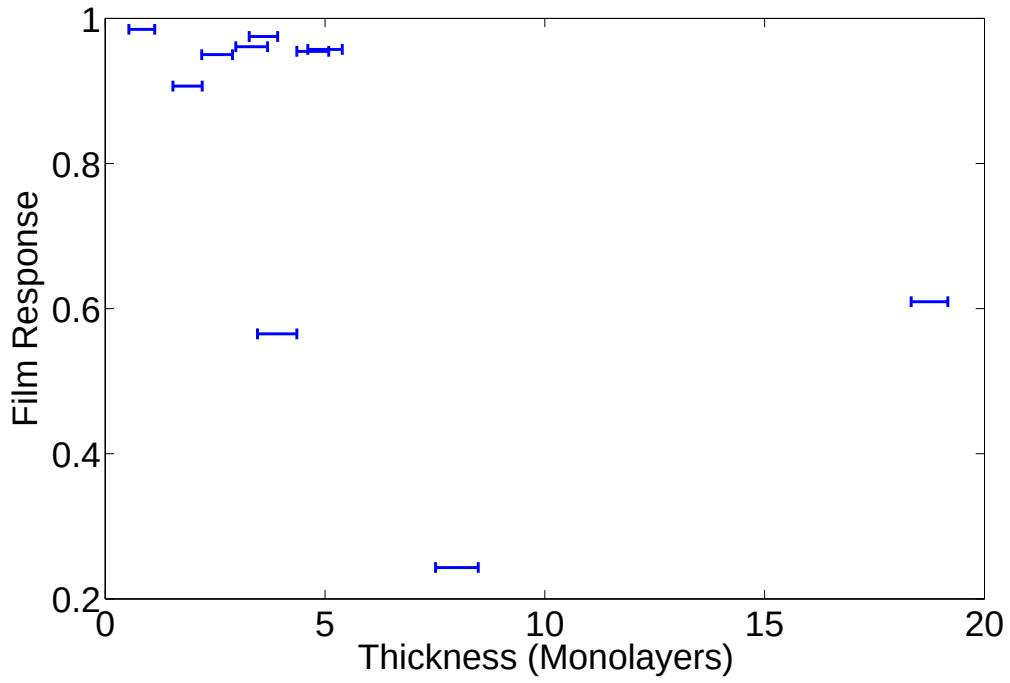

Figure 5.21: Response as a function of film thickness for several films of germanium clusters exposed to 99% relative humidity.

not controlled, but was typically in the range of 20-40%. Hence the 25% humidity response from Figure 5.20 can be compared to the venting data from Figure 5.16(top inset). The response observed in the gas rig is much slower in comparison to samples that were vented to air with a comparable relative humidity. This difference in response time was attributed to the speed at which water vapour was able to access the surface of the film. In the gas rig the change in humidity was reasonably slow as the dry air in the test chamber had to be replaced with humid air, whereas in the case of §5.4 the deposition chamber was changing from 10^{-7} Torr to atmospheric pressure in less than a minute, hence the humidity was also increasing over that time frame.

Figure 5.21 shows the 99% relative humidity response as a function of film thickness for several films of germanium clusters using the same exposure protocol as above. The samples are from Table 5.3 as well as three other sample that were not specifically deposited for gas sensing measurements. There is a slight trend that suggests that thicker films have less sensitivity. However, the trend is not as convincing as the response-thickness trend for previous cluster sensors (Figure 5.7). A clear trend was expected, as was observed for the sensitivity of germanium films exposed to air as a function of film thickness in the venting curve of Figure 5.17.

The film response as a function of sample age is shown in Figure 5.22 and has a clear trend that older samples have a poorer response to water vapour. Many

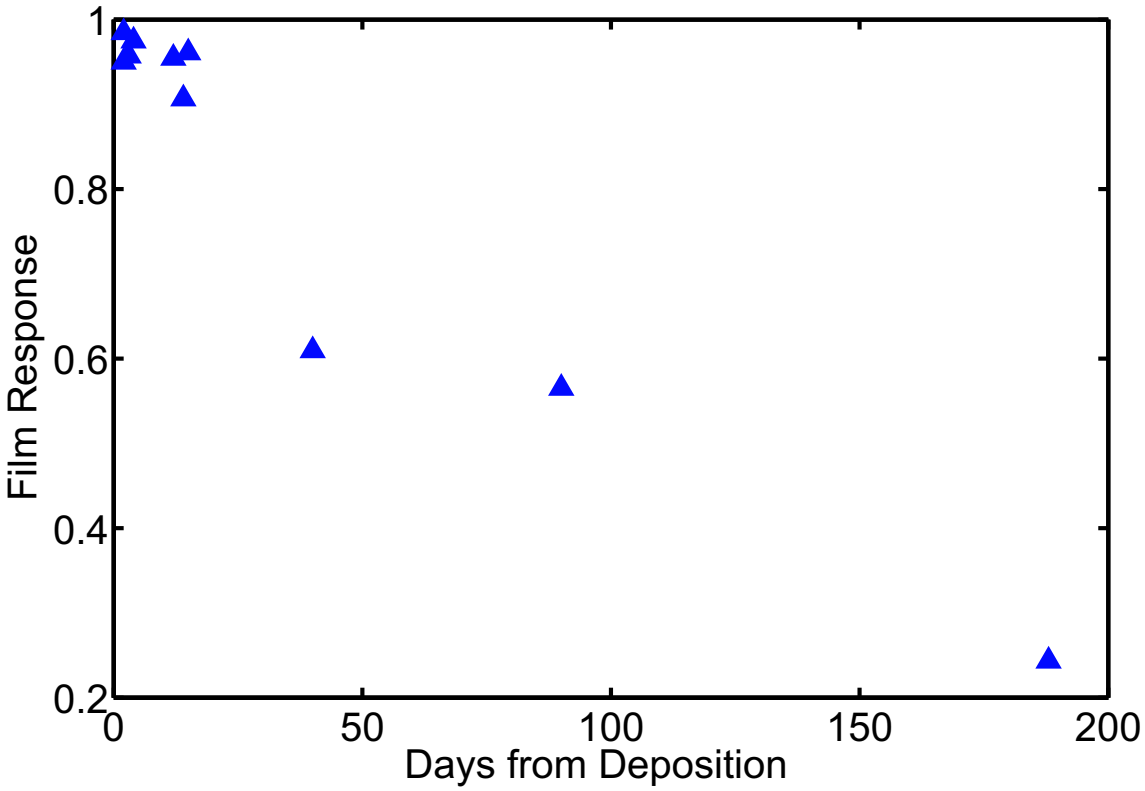

Figure 5.22: Response as a function of time since deposition for several films of germanium clusters exposed to 99% relative humidity.

samples simply "died" over time after venting and no response to humidity or hydrogen was able to be recorded. The cause of death of films is likely to be due to slow oxidative effects and/or additional surface defects that trap carriers resulting in a device resistance that is too high to measure. The reduction in response over time is obviously a major problem in terms of the long-term reliability and would prevent germanium films being used as humidity sensors.

5.5.3 Resistance Change Mechanism for Humidity Sensors

Several resistance change mechanisms are considered. The first possible mechanism is that water molecules align on the surface and the resulting electric field acts as a

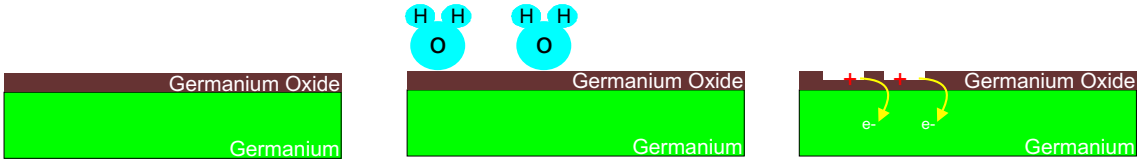

Figure 5.23: Schematic of mechanism of humidity sensor. Water vapour is introduced to the test chamber. The reaction of water vapour creates surface donors and electrons are injected into the film and these electrons are able to contribute to conduction, and an increase in current was observed.

gate bias. A schematic of this effect is shown in Figure 5.4(left). This mechanism appears unlikely to be responsible for the humidity sensing behaviour because the surfaces of the cluster films are rough and there is no physical reason for the water molecules to align in this sensor setup.

Another suggested mechanism is proton surface conduction, described in §5.1.3, which would not require any change in measured resistance of the germanium film itself; the change in resistance would be caused by surface conduction. This mechanism is ruled out because no conduction was observed for blank substrates and samples that had "died" also showed no observed resistance change, even at 99% humidity.

Another suggested mechanism for the decrease in resistance observed in germanium films in a humid atmosphere is a slightly modified version of the standard metal oxide mechanism (§5.1.2). Figure 5.23 shows a schematic of the proposed mechanism. Although this mechanism is similar to that proposed for the change of resistance for metal oxide gas sensors due to reducing gases (Figure 5.2), this process is different as water is not a reducing molecule.

It is well documented (see §5.1.1 for details) that germanium oxide dissolves in water. The reaction of germanium oxide and water potentially creates defects on the surface which can act as donors. The donors can then alter the resistivity of the sensor in the same two ways as the standard metal oxide mechanism: either by drawing electrons into the film using a gate mechanism or by donors supplying electrons into the film directly.

It was not possible to establish if the gate mechanism or the electron donation mechanism are responsible for the resistance change in the germanium humidity sensors. Although the gate effect of germanium cluster films previously observed in air in §5.4.2 was 1000 times smaller than the change in resistance in air due to humidity, the gate mechanism cannot be rejected. This is because the donors are on the oxide surface which is only 2 nm away from the germanium film, compared to the 200 nm nitride thickness for the gate experiments.

5.6 Germanium Film Exposure to Hydrogen

In this section the response of films of germanium clusters exposed to different concentrations of hydrogen is investigated. Films were tested at atmospheric pressure in region 5 from Figure 5.10. §5.6.1 discusses how film response varies as a function of film thickness. Possible mechanisms for the observed change in resistance are discussed §5.6.2.

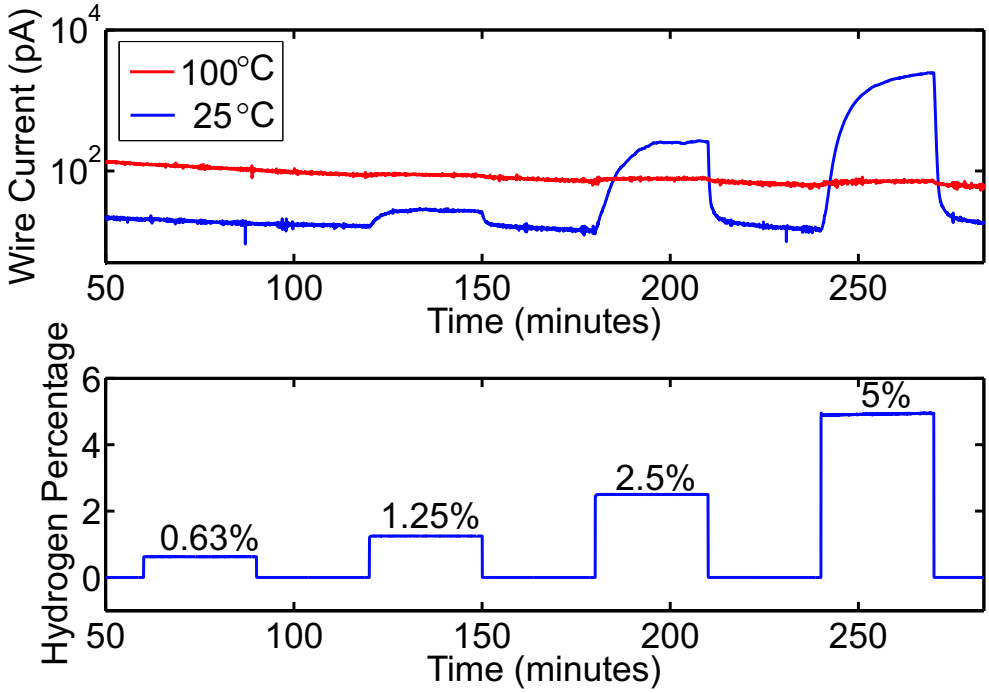

Figure 5.24: Response of germanium sample 45 to various concentrations of dry hydrogen gas for substrate temperatures of 25°C and 100°C. The percentages indicate the concentration of hydrogen, with the remainder of the flow made up of synthetic air.

5.6.1 Germanium Response to Hydrogen

Films of germanium clusters were exposed to controlled concentrations of hydrogen and the variation in current was recorded. To vary the hydrogen concentration, the flow rate of forming gas was increased and the amount of synthetic air decreased so that at all times the total flow rate was 100 sccm.

Figure 5.24 shows Percolation Sample 45, the first sample to be tested for hydrogen sensitivity and it shows a typical response of a germanium film to various concentrations of dry hydrogen gas for substrate temperatures of 25°C and 100°C. At 25°C the current of the film in dry air was very low. A noticeable change in resistance is observed for hydrogen percentages above 1.25%. When the hydrogen flow is the maximum of 5% concentration, the resistance of the device is reduced by approximately two orders of magnitude. However, no change in resistance is observed for any hydrogen concentration when the temperature of the sample is 100°C. The lack of response at 100°C suggests water on the surface of the film is necessary for the device to operate as a hydrogen sensor. The samples used in the section are the same as samples used for humidity detection in the previous section.

The increase in current observed at 100°C is due to the temperature dependent nature of the semiconducting film (see Equation 4.4). The slight decrease in current

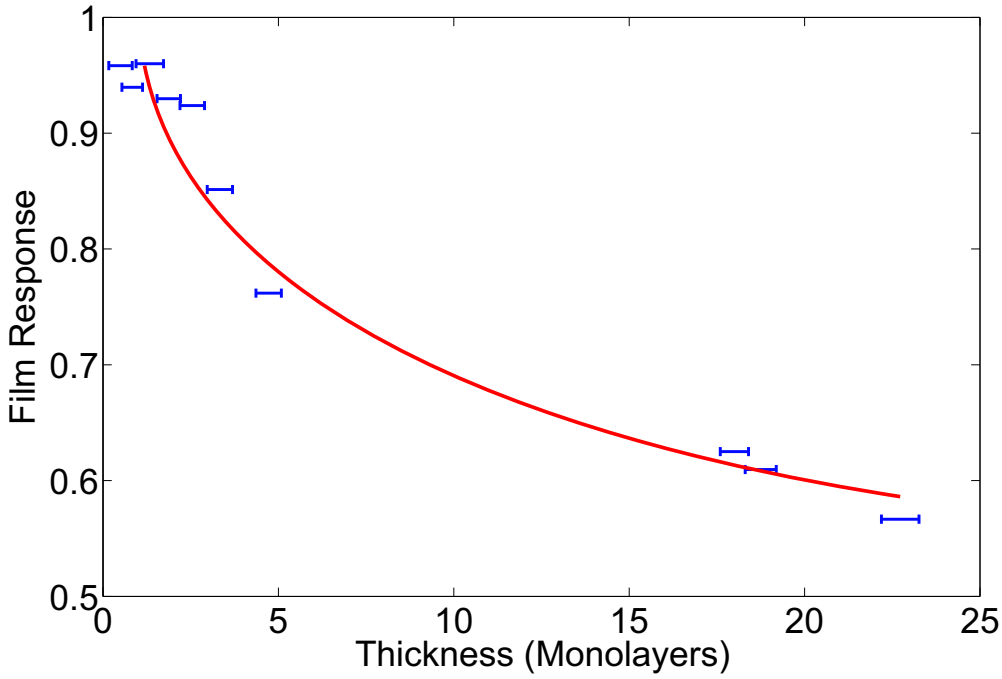

Figure 5.25: Room temperature response of germanium films as a function of film thickness to 5% hydrogen concentration. Samples are the same as in Figure 5.21.

observed over time in the 100°C film is attributed to a slow removal of water vapour from the surface of the film. The subsequent decrease in measured current is consistent with the results from §5.5. When multiple films were tested, a trend appeared based on film thickness. Figure 5.25 shows the room temperature response of germanium films as a function of film thickness for 5% hydrogen concentration. These samples had the same exposure protocols as Figure 5.24, which was the standard hydrogen exposure protocol with the 5% film response recorded at the end of the 30 minute 5% hydrogen period.

A clear trend is observed that thicker films have a smaller response to hydrogen. This behaviour is due to the larger surface-volume ratio of the thinner films which are more sensitive because they have a higher number of released electrons per unit volume. This thickness-response relation is consistent with previous gas sensing behaviour observed in cluster devices [28] and shown in Figure 5.7. Although the germanium films in this section exhibit an excellent response to hydrogen, no response was detected for concentrations under 1%. Tin oxide clusters [25] show a response to hydrogen as low as 10 ppm. This lower sensitivity of the germanium films is probably due to the tin oxide clusters having smaller diameters (3-10 nm diameter) compared to the ∼35 nm for GS samples.

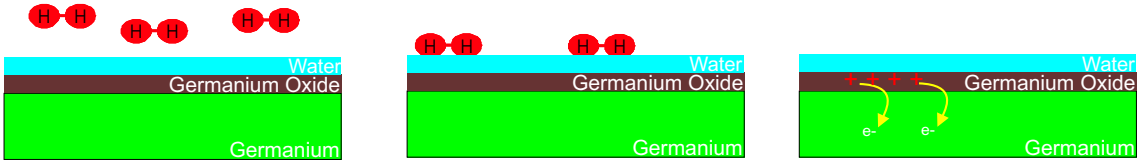

Figure 5.26: Schematic of the interaction of hydrogen with an n-type germanium film. Hydrogen is introduced to the test chamber and interacts with the surface. Reduction occurs at the surface of the film and additional electrons are able to contribute to conduction, and an increase in current is observed.

5.6.2 Resistance Change Mechanism for Hydrogen Sensors

The sensors show a large response to hydrogen at room temperature, but not at 100°C. For a typical semiconducting gas sensor, increasing device temperature improves sensitivity [89]. The lack of response at 100°C suggests that a small amount of surface water is necessary for a change in film resistance. A potential reaction is:

$$2H_2O + H_2 \rightleftharpoons 2H_3O^+ + 2e^- \tag{5.9}$$

which would occur independently of the germanium film and would allow surface conduction from H_3O^+ ions. However, if this was the case, then conduction would be expected in all room temperature devices, and this was not observed.

Another suggested mechanism for the observed change in resistance for germanium films is hydrogen reacting with the surface oxide. This reaction adds electrons into the film which contribute to conduction and is equivalent to the metal oxide gas sensor mechanism of §5.1.2.

In the case of germanium cluster films the standard metal oxide sensor mechanism requires slight modification to allow for hydrogen sensitivity only being observed below 100°C. Figure 5.26 shows a schematic of the adsorption of hydrogen sensor mechanism with a germanium film. Initially, hydrogen is introduced to the gas rig. Before any hydrogen is adsorbed, the existing water vapour will have created a small number of defects (and corresponding electrons in the film (see §5.5.3)). It is proposed that hydrogen enhances the creation of defects. If this is the case, the additional defects created by hydrogen will act as donors and (like §5.5.3) therefore additional electrons will be added to the film either directly from the donors or drawn in from the contacts.

5.7 Conclusion

In this chapter germanium cluster devices have been characterized. Hall measurements were successful in determining the carrier concentration and gated measure-

ments successfully affected the source-drain current in germanium films. When films of germanium clusters were exposed to hydrogen and water vapour, a large reversible decrease in resistance was observed meaning that films were successfully able to be used as gas and humidity sensors.

The carrier concentration of the germanium films was typically $\sim 1\times10^{14}\text{cm}^{-3}$ after onset of conduction, reducing to $\sim 1\times10^{12}\text{cm}^{-3}$ over several days in vacuum. When exposed to non-dry air, the carrier concentration increased to $\sim 1\times10^{14}\text{cm}^{-3}$ due to donors from water vapour. These values suggest that after deposition the carrier concentration is slightly higher than bulk germanium $\sim 2.4\times10^{13}\text{cm}^{-3}$ and this implies the presence of a small amount of impurities.

Immediately after deposition, the gate effect was small and any changes in resistance or carrier concentration were due to oxidation and capacitive effects from ramping the gate bias. As the samples slowly oxidized in vacuum, an increase in the gate effect was observed as a decrease in the overall carrier concentration was observed. Therefore, the gate bias was able to more effectively enhance the current.

The germanium devices in this project show a maximum gate effect when the sample had been able to oxidize for a few days in vacuum, just prior to venting, with a 12% change in resistance observed for a 50 V gate bias. The magnitude of the gate effect increased with time when the sample was in vacuum because the overall carrier concentration was decreasing so the gate bias was able to more effectively enhance the current. The opposite effect was observed when the films were vented to air; the carrier concentration increase resulted in a less effective current enhancement. The gate effect observed in germanium devices was small compared to germanium transistors from the literature, where a 5 V gate bias would affect the source drain current by a factor of 10^5.

A conceivable contributing factor as to why the observed gate effect in germanium cluster films is of such a small magnitude in comparison to germanium transistors from the literature is that the films are made up of clusters (cluster effects are discussed in §3.1.3). It is possible that the gate effect could be enhanced if the germanium films were annealed as the annealing process could remove grain boundaries. This would technically be difficult due to the high melting point of germanium and an annealing stage in this temperature range is not currently available at Canterbury.

When films of germanium clusters were vented to air, the oxide layer increased to the maximum thickness (1-2 nm as determined by HR-TEM analysis in §4.2.4), but the resistance decreased due to adsorption of water vapour. The suggested mechanism for the reversible decrease in resistance is due to water vapour reacting with germanium oxide. The proposed mechanism involves water creating defects on

the surface and the defects acting as donors. It was found that thinner films were more sensitive to the venting process attributed to thinner films having a higher number of injected electrons per unit volume.

In the case of humidity sensors, the film response was greatest for thin films and films which had recently been deposited. The fall-off in response over time is attributed to defects forming on the surface creating traps for electrons. These experiments provided further evidence that the decrease in resistance observed after exposing films to air can be attributed to water vapour.

For the case of hydrogen sensors, the thinnest films were found to be most sensitive. The larger sensitivity was due to the larger surface-to-volume ratio. The hydrogen sensors in this project show less sensitivity than previous cluster hydrogen sensors [24], presumably due to the comparably larger size of the germanium clusters. The proposed mechanism involves a slightly modified metal oxide gas sensing mechanism where surface water is essential for the creation of donors.

It would be possible to use the gated samples to investigate transistor behaviour as a function of exposure to both hydrogen and humidity. These experiments were not attempted due to time constraints. It is also feasible, if a magnet was added to the gas rig, to use Hall measurements to directly observe the change in carrier concentration as a function of gas flow and applied gate bias.

Chapter 6

Conclusion

This final chapter summarizes the main results in this thesis of which there were three main topics of research. Firstly, gated measurements were performed on bismuth cluster devices with sidegates. Fabrication of these nanoscale bismuth cluster devices using the PMMA aperture method was a success. However, the gate effects observed in the bismuth sidegate devices were weak and inconclusive. Secondly, a germanium cluster source was built and characterized. Basic electrical characterization was successfully performed using films of germanium clusters. Thirdly, germanium cluster devices were investigated with successful gated measurements, Hall measurements and gas sensing measurements being performed.

Bismuth Sidegate Devices

Bismuth sidegate devices were successfully fabricated using the PMMA aperture method. Initially, the limit of the PMMA aperture method for bismuth clusters was investigated. Using the PMMA aperture method and bismuth clusters of 30 nm diameter, a nanowire of 80 nm width was achieved. However, if parallel wires were in close proximity then a trench overflowing effect would occur and would result in a connection between parallel wires.

Parallel bismuth nanowires of 300 nm diameter were deposited at a distance of 200 nm apart without any gate-channel connection occurring during cluster deposition. This result proved the fabrication of nanoscale bismuth cluster devices with sidegates using the PMMA aperture method was a success.

The gate effects observed in the sidegate structures were weak and inconclusive. A small gate effect of up to 0.1% was observed in some devices at 11 K, but no gate effect was observed in other devices with the same sample dimensions. It is likely that the sample temperatures, wire dimensions and gate-channel separations were just above the range where a consistent and observable gate effect is possible.

The limitation of the PMMA aperture method to produce bismuth devices with a significant gate effect means it was not possible to produce very thin wires or obtain very small gate-channel separation.

Production of Germanium Clusters

A germanium source was developed and used to consistently produce a high flux of germanium clusters. The high flux enabled the deposition of germanium cluster-based devices. Characterization of the source included size analysis which enables source conditions to be chosen to allow selection of clusters of certain diameters. HR-TEM analysis determined the clusters were single crystal surrounded by a 1-2 nm amorphous oxide shell.

Measuring the electrical characteristics of germanium cluster films was hindered because of the high resistivity of germanium clusters. The onset of conduction and current voltage characteristics were only measurable for films in excess of the percolation threshold. However, thick films of germanium clusters (200-500 nm) were successfully characterized. As well as the high resistivity, a dominant feature of germanium cluster films was an increase in resistance over time, attributed to oxidation. Although films were held at 10^{-7} Torr, a resistance increase (that followed a power law) were always observed.

The high resistance of films at room temperature meant that low temperature electrical characterization was difficult. Data below 200 K was difficult to distinguish from substrate leakage current with typical measured resistances of $\sim$100GΩ.

The room-temperature current-voltage characteristics were typically linear in the $\pm$10 V range, with non-linear characteristics being observed for some thicker films. The non-linearity of I(V) measurements decreased over time as the films oxidized in vacuum.

Hall Samples of Germanium Clusters

Films of germanium clusters were successfully characterized using the Hall effect and by applying a gate bias.

The carrier concentration of the germanium films was typically $\sim 1\times10^{14}\text{cm}^{-3}$ after onset of conduction, reducing to $\sim 1\times10^{12}\text{cm}^{-3}$ over several days in vacuum. When exposed to non-dry air, the carrier concentration increased to $\sim 1\times10^{14}\text{cm}^{-3}$ due to donors from water vapour. These values suggest that after deposition the carrier concentration is slightly higher than bulk germanium $\sim 2.4\times10^{13}\text{cm}^{-3}$ and this implies that a small amount of impurities are present.

Immediately after deposition, the gate effect was small and any changes in resistance or carrier concentration were due to oxidation and capacitive effects from ramping the gate bias. As the samples slowly oxidized in vacuum, an increase in the gate effect was observed as a decrease in the overall carrier concentration was observed. Therefore, the gate bias was able to more effectively enhance the current.

When germanium films were vented to air, the carrier concentration increased and this was attributed to water vapour creating surface defects which act as donors. The additional carrier concentration resulted in a gate effect of smaller magnitude being observed, presumably because the higher number of carriers was more difficult to deplete/enhance.

Germanium Film Sensitivity to Hydrogen and Humidity

When films of germanium clusters were exposed to air, a decrease in resistance was observed that was attributed to the adsorption of water vapour. Thinner films were more sensitive to the air exposure process. The air exposure results were further investigated using a humidity test rig.

A large decrease in resistance was observed when germanium films were exposed to humid air. The proposed mechanism for humidity affecting the resistance of germanium films is water dissolving germanium oxide and in the process creating surface defects. These defects act as donors reducing the measured resistance by either adding electrons to the film or by drawing electrons from the drain into the film. Although the sensitivity of sensors shows a slight decrease with film thickness, a drop off in sensitivity over time was observed. The sensitivity drop off was attributed to defects forming on the surface and creating traps for electrons. The long-term decrease in response of germanium clusters films to humidity would prevent germanium films being used as humidity sensors.

The films of germanium clusters also show sensitivity to hydrogen. Hydrogen sensing behaviour was only observed below 100°C, suggesting that water adsorbed on the surface was necessary for the sensing mechanism. The proposed mechanism for sensing is that hydrogen enhances the creation of defects which in turn creates additional donors which either add electrons to the film or draw electrons from the drain into the film, reducing the measured resistance. Thinner films were more sensitive and this was attributed to thinner films having a higher number of additional electrons per unit volume.

Acknowledgements

Firstly I would like to thank my supervisor, Associate Professor Simon Brown for consistent support, advice, proofreading feedback and allowing me to travel to Australia, Japan and the United States during my thesis. My other supervisors, Dr. Jim Partridge and Dr. Euan Boyd were very helpful in planning and analysis of experiments.

A big thank you to all the technical staff of the physics department who always produced quality work and often were able to manufacture just what was required in a very short time. Specific thanks goes to Stephen Hemmingsen and Graeme Kershaw for making what must have seemed like an endless supply of crucibles and heatshields for the germanium source. Robert Thirkettle and Wayne Smith were very helpful in using the leak detector when required. Bob Flygenring needs a special mention, he does amazing things to make liquid helium and always made sure that I had a steady supply even when I was using 20 litres in a night. Also, the clean room in the electrical engineering department is run by Helen Devereux and Gary Turner who made many of the lithography and EBL processes run much more smoothly.

Thanks for all the support from past and present members of the cluster group, Dr. Rene Reichel, Dr. Ahmad Ayesh, Dr. David McCarthy, Dr. KC Tee, Dr. Euan Boyd, Dr. Pierre Convers, Dr. Pawel Kowalczyk, Dr. Frank Natali, Abdul Sattar, Domagoj Belic, Ojas Mahapatra, Emily Dahlberg, Keri Nichol and Toby Matthewson.

Thank you to Richard Tilley and Sujay Prabakar who performed HR-TEM work at Victoria University and thanks to my proofreaders, Donald Mackenzie, Domagoj Belic and Jennifer Nield.

Special thanks to my father who has supported and encouraged me throughout my university studies to ensure that I am excessively qualified for any job I might apply for.

Finally, I would like to thank the MacDiarmid Institute for Advanced Materials and Nanotechnology for the scholarship they provided to enable this thesis.

Bibliography

[1] T. Appenzeller and R. Feynman. The man who dared to think small. *Science*, 254:1300–01, 1991.

[2] S. M. Sze. *Physics of Semiconductor Devices*. Wiley, 2nd edition, 1981.

[3] G. E. Moore. Cramming more components onto integrated circuits. *Electronics*, 38(8):56–59, 1966.

[4] W. Shockley. A unipolar field effect transistor. *Proceedings of the IRE*, 40(11): 1365–76, 1952.

[5] M. Levenshtein and G. Simin. *Transistors, from crystals to integrated circuits*. World Scientific, 2000.

[6] H. Haberland, B. Issendorff, J. Yufeng, T. Kolar and G. Thanner. Ground state and response properties of mercury clusters. *Atoms, molecules and clusters*, 26:8–12, 1993.

[7] R. Busnai, M. Folkers and O. Cheshnovsky. Direct observation of Band-gap closure in mercury clusters. *Phys. Rev. Letters*, 81(18):3836–39, 1998.

[8] S. L. Lai, J. Y. Guo, V. Petrova, G. Ramanath and L. H. Allen. Size-Dependent Melting Properties of Small Tin Particles: Nanocalorimetric Measurements. *Phys. Rev. Letters*, 77(1):99–102, 1996.

[9] H. Haberland. *Cluster of Atoms and Molecules*. Springer, 1994.

[10] H. Kroto, J. R. Heath, S. C. O'Brien, R. F. Curl and R. E. Smalley. C_{60} Buckminsterfullerene. *Nature*, 318(14):162–63, 1985.

[11] O. Echt, K. Sattler and E. Recknagel. Magic Numbers for Sphere Packings Experimental Verification in Free Xenon Clusters. *Phys. Rev. Letters*, 47(16): 1121–24, 1981.

[12] T. Castro, R. Reifenberger, E. Choi and R. P. Andres. Size-dependent melting temperature of individual nanometer-sized metallic clusters. *Phys. Rev. B.*, 42(13):8548–57, 1990.

[13] G. M. Francis, L. Kuipers, J. R. A. Cleaver and R. E. Palmer. Diffusion controlled growth of metallic nanoclusters at selected surface sites. *J. Appl. Phys.*, 79(6):2942–47, 1996.

[14] K. H. Meiwes-Broer. *Metal Clusters at Surfaces.* Springer, 2000.

[15] L. Bardotti, B. Prevel, M. Treilleux, P. Melinon and A. Perez. Deposition of preformed gold clusters on HOPG and gold substrates: influence of the substrate on the thin film morphology. *Appl. Surf. Sci.*, 164:52–9, 2000.

[16] P. Jensen. Growth of nanostructures by cluster deposition: Experiments and simple models. *Rev. Modern*, 71(5):1695–35, 1999.

[17] D. M. Schaefer, R. Reifenberger, A. Patil and R. P. Andres. Fabrication of two-dimensional arrays of nanometer-size clusters with the atomic force microscope. *Appl. Phys. Lett.*, 66(8):1012–14, 1995.

[18] M. Schulze, S. Gourley, S. A. Brown, A. Dunbar, J. Partridge and R. J. Blaikie. Electrical Measurements of Nanoscale Bismuth Cluster Films. *Eur. Phys. J. D.*, 24:291–95, 2003.

[19] B. Bollobas and Oliver Riordan. *Percolation.* Cambridge University Press, 2006.

[20] R. Weil. *Percolation Structure and Processes.* Hilger, 1983.

[21] G. Parguez, F. Natali and S. A. Brown. Oxidation of bismuth cluster films. *Cur. Appl. Phys.*, 8:287–90, 2008.

[22] A. D. F. Dunbar, J. Partridge, M. Schulze and S. A. Brown. Morphological differences between Bi, Ag and Sb nano-particles and how they affect the percolation of current through nano-particle networks. *Eur. Phys. J. D.*, 39: 415, 2006.

[23] R. Reichel, J. G. Partridge, A. D. F. Dunbar and S. A. Brown. Construction and Application of a UHV Compatible Cluster Deposition System. *Journal of Nanoparticle Research*, 8:405, 2006.

[24] J. van Lith, A. Lassesson, S. A. Brown, M. Schulze, J. G. Partridge and A. Ayesh. 2D tunneling based hydrogen sensors. *Appl. Phys. Lett.*, 91:181910, 2007.

[25] A. Lassesson, M. Schulze, J. van Lith and S. A. Brown. Tin oxide nanocluster hydrogen and ammonia sensors. *Nanotechnology*, 19:015502, 2008.

[26] R. Reichel. *Nano Scale Cluster Devices*. PhD thesis, University of Canterbury, 2007.

[27] K. C. Tee. *Cluster Devices/Interconnects for Nanotechnology*. PhD thesis, University of Canterbury, 2007.

[28] T. Watson. Tin oxide cluster assembled films: Morphology and gas sensors. Master's thesis, University of Canterbury, 2009.

[29] A. Ayesh. *Device Fabrication using Bi nanoclusters*. PhD thesis, University of Canterbury, 2007.

[30] E. J. Boyd and S. A. Brown. Size dependence of SnO_2 atomic cluster nanowire Field Effect Transistors. *In press*, 2009.

[31] T. Matthewson. *Nanocluster devices on templated substrates*. Honours Research Project, 2006.

[32] D. M. A. Mackenzie. *Templates and stencils for the controlled assembly of nanoclusters on contacted substrates*. Honours Research Project, 2005.

[33] S. A. Scott, M. V. Kral and S. A. Brown. Self-assembly of oriented Bi nanorods at highly ordered pyrolitic graphite step-edges. *Phys. Rev. B.*, 72:205423, 2005.

[34] R. Reichel, J. G. Partridge, F. Natali, T. Matthewson, S. A. Brown, A. Lassesson, D. M. A. Mackenzie, A. Ayesh, K. C. Tee, A. Awasthi and S. C. Hendy. From the adhesion of atomic clusters to the fabrication of nanodevices. *Appl. Phys. Lett.*, 89:213105, 2006.

[35] J. Partridge, T. Matthewson, and S. A. Brown. Bi cluster-assembled interconnects produced using SU8 templates. *Nanotechnology*, 18:155607, 2007.

[36] J. G Partridge, S. A. Brown, A. D. F. Dunbar, R. Reichel, M. Kaufmann, C. Siegert, S. Scott and R. J. Blaikie. Templated-assembly of conducting antimony cluster wires. *Nanotechnology*, 15:1382–94, 2004.

[37] J. G. Partridge, S. A. Brown, C. Siegert, A. D. F. Dunbar, R. Nielson, M. Kaufmann and R. J. Blaikie. Templated cluster assembly for production of metallic nanowires in passivated silicon V-grooves. *Microelec. Engr.*, 73-74: 583–87, 2004.

[38] T. M. Adams and R. A. Layton. *Introductory MEMS fabrication and applications*. Springer, 2010.

[39] C. S. Yoo. *Semiconductor manufacturing technology*. World Scientific, 2008.

[40] R. Chang. *Chemistry*. McGraw-Hill, 2002.

[41] A. Goeta and A. B. Focke. Density and Conductivity of Bismuth Single Crystals Grown in Magnetic Fields with Relation to their Mosaic Structure. *Phys. Rev.*, 37:1044–56, 1931.

[42] D. R. Lovett. *Semimetals and Narrow-Bandgap semiconductors*. Pion, 1977.

[43] C. A. Hogarth. *Materials used in Semiconductor Devices*. Wiley, 1965.

[44] N. W. Ashcroft and N. D. Mermin. *Solid State Physics*. Brooks/Cole, 1976.

[45] G. Dresselhaus, M. S. Dresselhaus, Z. Zhang and X. Sun. Modelling thermoelectric behavior in Bi nano-wires. *International Conference on Thermoelectrics*, pages 43–46, 1998.

[46] G. E. Smith, G. A. Baraff and J. M. Rowell. Effective g Factor of Electrons and Holes in Bismuth. *Phys. Rev.*, 135:A1118–24, 1964.

[47] L. Li, Y. Yang, X. Fang, M. Kong, G. Li and L. Zhang. Diameter-dependent electrical transport properties of bismuth nanowire arrays. *Sol. State. Comm.*, 141:492–96, 2007.

[48] C. A. Hoffman, J. R. Meyer, F. J. Bartoli, A. D. Venere, X. J. Yi, C. L. Hou, H. C. Wang and J. B. Ketterson. Semimetal-to-semiconductor transition in bismuth thin film. *Phys. Rev. B.*, 48(15):11431–38, 1993.

[49] N. Garcia, Y. H. Kao and M. Strongin. Galvanomagnetic Studies of Bismuth Films in the Quantum-Size-Effect Region. *Phys. Rev. B*, 6(6):2029–39, 1972.

[50] J. Heremans, C. M. Thrush, M. S. Dresselhaus and J. F. Mansfield. Bismuth nanowire arrays: Synthesis and galvanomagnetic properties. *Phys. Rev. B.*, 61(4):2921–30, 2000.

[51] T. W. Cornelius, M. E. Toimil-Molares, R. Neumann, G. Fahsold, R. Lovrincic, A. Pucci and S. Karim. Quantum size effects manifest in infrared spectra of single bismuth nanowires. *Appl. Phys. Lett.*, 88:103114, 2006.

[52] X. F. Wang, J. Zhang, H. Z. Shi, Y. W. Wang, G. W. Meng, X. S. Peng, L. D. Zhang and J. Fang. Fabrication and temperature dependence of the resistance of single-crystalline Bi nanowires. *J. Appl. Phys.*, 89(7):3847–51, 2001.

[53] J. Reppert, R. Rao, M. Skove, J. He, M. Craps, T. Tritt and A. M. Rao. Laser-assisted synthesis and optical properties of bismuth nanorods. *Chem. Phys. Lett.*, 442:334–38, 2007.

[54] W. Shim, J. Ham, K. Lee, W. Jeung, M. Johnson and W. Lee. On-Film Formation of Bi Nanowires with Extraordinary Electron Mobility. *Nano. Lett.*, 9(1):18–22, 2009.

[55] K. Liu, C. L. Chien and P. C. Searson. Finite-size effects in bismuth nanowires. *Phys. Rev. B.*, 58(22):681–85, 1998.

[56] K. Liu, C. L. Chien, P. C. Searson and K. Y. Zhang. Structural and magnetotransport properties of electrodeposited bismuth nanowires. *Appl. Phys. Lett.*, 73(10):1436–38, 1998.

[57] R. A. Hoffman and D. R. Frankl. Electrical Transport Properties of Thin Bismuth Films. *Phys. Rev. B.*, 3(9):1825–34, 1971.

[58] E. I. Rogacheva, S. N. Grigorov, O. N. Nashchekina, S. Lyubchenko and M. S. Dresselhaus. Quantum-size effects in n-type bismuth thin films. *Appl. Phys. Lett.*, 82(16):2628–30, 2003.

[59] A. V. Butenko, V. Sandomirsky, Y. Schlesinger, D. Shvarts and V. A. Sokol. Characterization of the electrical properties of semimetallic Bi films by electric field effect. *J. Appl. Phys.*, 82(3):1266–73, 1997.

[60] A. Boukai, K. Xu and J. R. Heath. Size-dependent transport and thermoelectric properties of individual polycrystalline bismuth nanowires. *Adv. Materials*, 18:864–69s, 2006.

[61] V. T. Petrashov, V. N. Antonov and B. Bilsson. Electric field effects and screening in mesoscopic bismuth wires. *J. Phys.: Condens. Matter*, 3:9705–11, 1991.

[62] C. A. Mead. Anomalous Capacitance of Thin Dielectric Structures. *Phys. Rev. Lett.*, 6:545–6, 1961.

[63] C. Reale. Field effect in vacuum deposited Bismuth films. *Phys. Lett. A.*, 35 (6):437–8, 1971.

[64] C. S. Walker. *Capacitance, Inductance and Crosstalk Analysis*. Artech House, 1990.

[65] M. Lu, R. J. Zieve, A. van Hulst, H. M. Jaeger, T. F. Rosenbaum and S. Radelaar. Low-temperature electrical-transport properties of single-crystal bismuth films under pressure. *Phys. Rev. B.*, 53(3):1609–1615, 1996.

[66] L. Leontie, M. Caraman, M. Alexe and C. Harnagea. Structural and optical characteristics of bismuth oxide thin films. *Surf. Sci.*, 507-510:480–85, 2002.

[67] E. Puckrin and A. J. Slavin. Comparison of the oxidation of polycrystaline bulk bismuth and thin bismuth films on the Au(111) surface. *Phys. Rev. B.*, 42(2):1168–76, 1990.

[68] T. N. Taylor, C. T. Campbell, J. W. Rogers, W. P. Ellis and J. M. White. The interaction of oxygen with Bi(0001): Kinetic, electronic and structural features. *Surf. Sci.*, 134:529–46, 1983.

[69] R. A. Smith. *Semiconductors*. Cambridge University Press, 2 edition, 1978.

[70] E. J. Boyd and S. A. Brown. The size dependence of tin oxide atomic cluster nanowire field effect transistors. *Nanotechnology*, 20:425201, 2009.

[71] C. Winkler. Mittheilungen über das Germanium. *Journal für Praktische Chemie*, 36(1):177 – 209, 1877.

[72] F. Glocking. *The Chemistry of Germanium*. Academic Press, 1969.

[73] J. Bardeen and W. H. Brattain. The Transistor, A Semi-Conductor Triode. *Phys. Rev.*, 74:230 – 231, 1948.

[74] A. Smakula and V. Sils. Precision Density Determination of Large Single Crystals by Hydrostatic Weighing. *Phys. Rev.*, 99:1744, 1955.

[75] A. Smakula and J. Kalnajs. Precision Determination of Lattice Constants with a Geiger-Counter X-Ray Diffractometer. *Phys. Rev.*, 99:1737 – 1743, 1955.

[76] G. G. Macfarlane, T. P. McLean, J. E. Quarrington and V. Roberts. Fine Structure in the Absorption-Edge Spectrum of Ge. *Phys. Rev.*, 108:1377–83, 1957.

[77] P. B. Allen and M. Cardona. Temperature Dependence on the Direct Bandgap of Si and Ge. *Phys. Rev. B*, 28(8):4760–70, 1983.

[78] J. R. Hook and H. E. Hall. *Solid State Physics*. Wiley, 2nd edition, 2001.

[79] P. Y. Yu and M. Cardona. *Fundamentals of Semiconductors*. Springer, 1996.

[80] M. B. Prince. Drift Mobilities in Semiconductors. *Phys. Rev.*, 92:681 – 687, 1953.

[81] P. K. Schelling, L. Shu and K. E. Goodman. Managing heat for electronics. *Mater. Today*, pages 30–35, 2005.

[82] P. H. Keck and M. J. E. Golay. Crystallization of Silicon from a Floating Liquid Zone. *Phys. Rev.*, 98:1297, 1953.

[83] H. Torrey and C. Whitmer. *Crystal Rectifiers*. McGraw-Hill, 1948.

[84] H. Fritzsche. Impurity Conduction in Transmutation-Doped p-type Germanium. *Phys. Rev.*, 119(4):1239–45, 1960.

[85] E. H. Putley. The electrical conductivity of Germanium. *Proc. Phys. Soc.*, 42 (5):284–92, 1949.

[86] R. Enderlein and N. J. M. Horing. *Fundementals of Semiconductor Physics and devices*. World Scientific, 1997.

[87] D. A. Neamen. *Semiconductor Physics and Devices*. Irwin, 1992.

[88] C. Kittel. *Introduction to Solid State Physics*, volume 2. John Wiley, 1967.

[89] G. Korotcenkov. Metal oxides for solid-state gas sensors: What determines our choice? *Mater. Scien. and Engin. B*, 139:1–23, 2007.

[90] J. A. Dillion, Jr. and H. E. Farnsworth. Work-Function studies of Germanium Crystals Cleaned by Ion Bombardment. *J. Appl. Phys.*, 28(2):174–84, 1957.

[91] J. C. Rivière. The Workfunction of Gold. *Appl. Phys. Lett.*, 8(7):172, 1966.

[92] A. D. Schricker, S. V. Joshi, T. Hanrath, S. K. Banerjee and B. A. Korgel. Temperature Dependence of the Field Effect Mobility of Solution-Grown Germanium Nanowires. *J. Phys. Chem. B*, 110:6816–23, 2006.

[93] G. Gu, M. Burghard, G. T. Kim, G. S. Dusberg, P. W. Chiu, V. Krstic, S. Roth and W. Q. Han. Growth and electrical transport of germanium nanowires. *J. Appl. Phys.*, 90(11):5747–51, 2001.

[94] A. H. Clark. Electrical and Optical Properties of Amorphous Germanium. *Phys. Rev.*, 154(3):750–58, 1967.

[95] K. L. Chopra and S. K. Bahl. Structural, Electrical, and optical properties of amorphous germanium films. *Phys. Rev. B*, 1(6):2345–58, 1970.

[96] D. K. Pandya, A. C. Rastogi and K. L. Chopra. Obliquely deposited amorphous Ge films. I. Growth and structure. *J. Appl. Phys.*, 46(7):2966–75, 1975.

[97] J. J. Hauser and A. Staudinger. Electrical and structural properties of amorphous germanium. *Phys. Rev. B.*, 8(2):607–18, 1973.

[98] B. W. Sloop and C. O. Tiller. Electrical Properties of Epitaxial Ge Films deposited on (111) CaF_2 substrates. *J. Appl. Phys.*, 38(1):140–148, 1967.

[99] A. B. Greytak, L. J. Lauhon, M. S. Gudiksen and C. M. Liebera. Growth and transport properties of complementary germanium nanowire field-effect transistors. *Appl. Phys. Lett.*, 84(21):4176–78, 2004.

[100] D. Wang, Y. Chang, Q. Wang, J. Cao, D. Farmer, R. Gordon and H. Dai. Surface Chemistry and Electrical Properties of Germanium Nanowires. *J. Amer. Chem. Soc.*, 126:11602–11, 2004.

[101] Y. Wu and P. Yang. Germanium Nanowire Growth via Simple Vapor Transport. *Chem. Matter*, 12:605–07, 2000.

[102] C. L. Yuan and P. S. Lee. Enhanced charge storage capability of Ge/GeO_2 core/shell nanostructure. *Nanotechnology*, 19:335206, 2008.

[103] H. Omi and T. Ogino. Self-assembled Ge nanowires grown on Si(113). *Appl. Phys. Lett.*, 71(15):2163–5, 1997.

[104] D. I. Wang and H. Dai. Low-Temperature Synthesis of Single-Crystal Germanium Nanowires by Chemical Vapor Deposition. *Angew. Chem. Int. Ed.*, 41 (24):4783–86, 2002.

[105] X. Lu, D. D. Fanfair, K. P. Johnston and B. A. Korgel. High Yield Solution-Liquid-Solid Synthesis of Germanium Nanowires. *J. Am. Chem. Soc.*, 127: 15718–19, 2005.

[106] T. Hanrath and B. A. Korgel. Germanium nanowire transistors a comparison of electrical contacts patterned by electron beam lithography and beam-assisted chemical vapour deposition. *Proc. IMechE*, 218:25–34, 2005.

[107] B. Yu, X. H. Sun, G. A. Calebotta, G. R. Dholakia and M. Meyyappan. One-dimensional Germanium Nanowires for Future Electronics. *J. Cluster. Sci.*, 17(4):579–97, 2006.

[108] Y. H. Ahn and J. Park. Efficient visible light detection using individual germanium nanowire field effect transistors. *Appl. Phys. Lett.*, 91:162102, 2007.

[109] A. P. Cracknell. *Crystals and their structures.* Pergamon Press, 1969.

[110] F. C. Brown. *The physics of solids.* W. A. Benjamin, 1967.

[111] P. Krasnochtchekov, K. Albe, Y. Ashkenazy and R. S. Averback. Molecular-dynamics study of the density scaling of inert-gas condensation. *J. Chem. Phys.*, 123:154314, 2005.

[112] L. Pizzagalli, G. Galli, J. E. Klepeis and F. Gygi. Structure and stability of germanium nanoparticles. *Phys. Rev. B.*, 63:165324, 2001.

[113] D. Wang, Y. Chang, Z. Liu and H. Dai. Oxidation resistant germanium nanowires: bulk synthesis, long chain alkanethiol functionalization and Langmuir-Blodgett assembly. *J. Amer. Chem. Soc.*, 127(33):11871–75, 2005.

[114] A. Kant and B. H. Strauss. Atomization Energies of the Polymers of Germanium, Ge_2 to Ge_7 . *J. Chem. Phys.*, 45(3):822–26, 1966.

[115] B. R. Taylor and S. M. Kauzlarich. Solution Synthesis of Germanium Nanocrystals Demonstrating Quantum Confinement. *Chem. Matter*, 10:22–24, 1998.

[116] J. P. Wilcoxon, P. P. Provencio and G. A. Samara. Synthesis and optical properties of colloidal germanium nanocrystals. *Phys. Rev. B*, 64:035417, 2001.

[117] O. Keinzle, F. Ernst, M. Ruhle, O. G. Schmidt and K. Eberl. Germanium quantum dots embedded in silicon: Quantitative study of self-alignment and coarsening. *Appl. Phys. Lett.*, 74(2):269–71, 1999.

[118] A. K. Das, J. Kamila and B. N. Dev. Self-assembled Ge nanostructures on polymer-coated silicon: growth and characterization. *Appl. Phys. Lett.*, 77(7): 951–53, 2000.

[119] H. Yang, X. Wang, H. Shi, S. Xie, F. Wang, X. Gu and X. Yao. Photoluminence of Ge nanoparticles embedded in SiO_2 glasses fabricated by a sol-gel method. *Appl. Phys. Lett.*, 81(27):5144–47, 2002.

[120] J. G. Zhu, C. W. White, J. D. Budai, S. P. Withrow and Y. Chen. Growth of Ge, Si, and SiGe nanocrystals in SiO_2 matrices. *J. Appl. Phys.*, 78(7):4386–89, 1995.

[121] J. Jiang, K. Chen, X. Huang, Z. Li and D. Feng. New crystalline structure for nanometer-sized Ge microcrystallites prepared by plasma enhanced chemical vapor deposition. *Appl. Phys. Lett.*, 65(14):1799–1801, 1994.

[122] G. R. Burton, C. Xu, C. C. Arnold and D. M. Nuemark. Photoelectron spectroscopy and zero electron kinetic energy spectroscopy of germanium cluster anions. *J. Chem. Phys.*, 104(8):2757–64, 1996.

[123] S. Yoshida and K. Fuke. Photoionization studies of germanium and tin clusters in the energy region. *J. Chem. Phys.*, 111(9):3880–90, 1999.

[124] S. Sato, S. Nozaki and H. Morisaki. Photo-oxidation of germanium nanostructures deposited by the cluster-beam evaporation technique. *J. Appl. Phys.*, 81 (3):1518–21, 1996.

[125] J. Hecht, J. D. Eversole and H. P. Broida. Production and properties of homogeneously nucleated germanium particles. *J. Appl. Phys.*, 48(4):1503–08, 1977.

[126] Y. Saito. Crystal Structure and habit of Silicon and Germanium Particles grown in argon gas. *J. Crys. Growth*, 47:61–72, 1979.

[127] M. Zacharias, J. Bliising, J. Christen and U. Wendt. Ge nanocrystals with a sharp size distribution: A detailed study of the crystallization of a-$Si_{1-x}O_xGe_y$ alloy films. *J. Non-Crys. Solids*, 198:919–22, 1996.

[128] J. M. Hunter, J. L. Fye, M. F. Jarrold and J. E. Bower. Structural transitions in size-selected germanium cluster ions. *Phys. Rev. Letters*, 73(15):2063–66, 1994.

[129] Y. Maeda, N. Tsukamoto, Y. Yazawa, Y. Kanemitsu and Y. Masumoto. Visible photoluminescence of Ge microcrystals embedded in SiO_2 glassy matrices. *Appl. Phys. Lett.*, 59(24):3168–70, 1991.

[130] J. L. Xu and J. Y. Feng. Growth of Ge films by cluster beam evaporation. *Nucl. Intru. Meth. Phys. Rev.B*, 194:297–301, 2002.

[131] S. Banerjee, S. Nozaki and H. Morisaki. Electron transport in Ge nanocrystalline films deposited using the cluster beam evaporation technique. *J. Appl. Phys.*, 91(7):4307–11, 2002.

[132] Y. Kanemitsu, H. Uto, Y. Masumoto and Y. Maeda. On the origin of visible photoluminescence in nanometer-size Ge crystallites. *Appl. Phys. Lett.*, 61 (18):2187–91, 1992.

[133] S. Banerjee, S. Nozaki and H. Morisaki. Coulomb-blockade effect observed at room temperature in Ge nanocrystalline films deposited by the cluster-beam evaporation technique. *Appl. Phys. Lett.*, 76(4):445–47, 2000.

[134] M. Zacharias and P. M. Fauchet. Blue luminescence in films containing Ge and GeO_2 nanocrystals: The role of defects. *Appl. Phys. Lett.*, 71(3):380–83, 1997.

[135] O. Cheshnovsky, S. H. Yang, C. L. Pettiette, M. J. Craycraft, Y. Liu and R. E. Smalley. Ultraviolet photoelectron spectroscopy of semiconductor clusters: Silicon and germanium. *Chem. Phys. Lett.*, 138:119–124, 1987.

[136] A. A. R. Elshabini and F. D. Barlow. *Thin Film Technology Handbook*. McGraw-Hill, 1997.

[137] P. Y. Convers, D. N. McCarthy, A. Sattar, S. C. Hendy and S. A. Brown. Electrical Signature of Nanoscale Coalescence. *to be published*, pages 1–5, 2009.

[138] H. Fritzsche. Electrical Properties of Germanium Semiconductors at Low Temperatures. *Phys. Rev.*, 99(2):406–19, 1955.

[139] G. Sberveglieri. Recent developments in semiconducting thin-film gas sensors. *Sens. Actuators B.*, 23:103–109, 1995.

[140] Z. Chen and C. Lu. Humidity sensors: A review of materials and mechanisms. *Sensor Letters*, 3:274–295, 205.

[141] W. H. Brattain and J. Bardeen. Surface Properties of Germanium. *Bell. Sys. Tech. Jour.*, 32(1):1–37, 1953.

[142] J. Sldkov. Thin oxide films on germanium. *Czech. J. Phys.*, 18(6):801–5, 1968.

[143] N. N. Greenwood and A. Earnshaw. *Chemistry of the elements.* Pergamon Press, 1984.

[144] A. F. Wells. *Structural inorganic chemistry.* Clarendon Press, 5th edition, 1975.

[145] J. T. Law and P. S. Meigs. Rates of oxidation of germanium. *J. Electrochemical. Soc.*, 104(3):154–59, 1957.

[146] M. N. Khan, M. I. Khan and C. A. Hogarth. Electrical Properties of GeO_2 films. *Phys. Rev. B.*, 22(12):6155–61, 1980.

[147] J. D. Mackenzie. Structure of Liquid Germanium Dioxide. *J. Chem. Phys.*, 29(3):605–07, 1958.

[148] S. R. Morrison. Changes of Surface Conductivity of Germanium with Ambient. *J. Phys. Chem.*, 57:860–63, 1953.

[149] S. Shukla, S. Patil, S .C. Kuiry, Z. Rahman, T. Dua, L. Ludwib, C. Parish and S. Seal. Synthesis and characterization of solgel derived nanocrystalline tin oxide thin film as hydrogen sensor. *Sens. Actuators B.*, 96:343–53, 2003.

[150] H. Yamaura, T. Jinkawa, J. Tamak and Noboru Yamazoe a. Indium oxide-based gas sensor for selective detection of CO. *Sens. Actuators B.*, 35-36: 325–32, 1996.

[151] N. G. Patel, K. K. Makhijaa and C. J. Panchal. Fabrication of carbon dioxide gas sensor and its alarm system using indium tin oxide (ITO) thin films. *Sens. Actuators B.*, 21:193–97, 1994.

[152] A Kolmakov, Y Zhang, G Cheng and M Moskovits. Detection of CO and O_2 using tin oxide nanowire sensors. *Adv. Materials*, 15:997–1000, 2003.

[153] R. Martins, E. Fortunato, P. Nunes, I. Ferreira, A. Marques, M. Bender, N. Katsarakis, V. Cimalla and G. Kiriakidis. Zinc oxide as an ozone sensor. *J. Appl. Phys.*, 96(3):1398–1408, 2004.

[154] G. Eranna, B. C. Joshi, D. P. Runthala and R. P. Gupta. Oxide Materials for Development of Integrated Gas Sensors A Comprehensive Review. *Crit. Rev. Solid State Mater. Sci*, 29:111–80, 2004.

[155] H. Meixner, J. Gerblinger, U. Lampe and M. Fleischer. Thin-film gas sensors based on semiconducting metal oxides. *Sens. Actuators B.*, 23:119–25, 1995.

[156] T. Ishihara, K. Lometani and Y. Takita. Mixed Oxide Capacitor of $BaTiO_3PbO$ as a New Type CO_2 Gas Sensor. *Chem. Letters*, 7:1163–7, 1990.

[157] H. Seh, T. Hyodo and Harry L. Tuller. Bulk acoustic wave resonator as a sensing platform for NOx at high temperatures. *Sens. Actuators B.*, 108: 547–552, 2005.

[158] K.D. Schierbaum, U.K. Kirnera, J.F. Geigera and W. Gopela. Schottky-barrier and conductivity gas sensors based upon Pd/SnO_2 and Pt/TiO_2. *Sens. Actuators B.*, 4:87–94, 1991.

[159] M. Ivanovskaya, P. Bogdanov, G. Faglia and G. Sberveglieri. The features of thin film and ceramic sensors at the detection of CO and NO_2. *Sens. Actuators B.*, 68:34450, 2000.

[160] T. Sahm, A Gurlo, N. Barsan and U. Weimar. Basics of oxygen and tin oxide interaction; work function change and conductivity measurements. *Sens. Actuators B.*, 118:78–83, 2006.

[161] Y. Kato, K. Yoshikawa and M. Kitora. Temperature-dependent dynamic response enables the qualification and quantification of gases by a single sensor. *Sens. Actuators B.*, 40:33–7, 1997.

[162] G. Sakai, N. S. Baik, N. Miura and N. Yamazoe. Gas sensing properties of tin oxide thin films fabricated from hydrothermally treated nanoparticles. *Sens. Actuators B.*, 77:116–21, 2001.

[163] A. Rothschild and Y. Komem. The effect of grain size on the sensitivity of nanocrystalline metal-oxide gas sensors. *J. Appl. Phys.*, 95(11):6374–80, 2004.

[164] N. Barsan and U. Weimar. Conduction model of metal oxide gas sensors. *J. Microceramics*, 7:143–67, 2001.

[165] Y. Zhang, K. Yua, D. Jiangd, Z. Zhua, H. Genge and L. Luo. Zinc oxide nanorod and nanowire for humidity sensor. *Appl. Surf. Sci.*, 242:212–17, 2005.

[166] T. Seiyama, N. Yamazoe and H. Arai. Ceramic humidity sensors. *Sensors and Actuators*, 4:85–9, 1983.

[167] K. Seeger. *Semiconductor Physics*. Springer, 2004.

[168] E. P. O'Reilly and J. Roberson. Theory of defects in vitreous silicon dioxide. *Phys. Rev. B.*, 27(6):3780–95, 1983.

[169] W. E. Hanford and R. M. Joyce. Polytetrafluoroethylene. *J. Am. Chem Soc*, 68:2082–85, 1946.

[170] Y. Awakuni and J. H. Calderwood. Water vapour adsorption and surface conductivity in solids. *J. Phys. D.*, 5:1038–44, 1972.

[171] F. Maier, M. Riedel, B. Mantel, J. Ristein and L. Ley. Origin of Surface Conductivity in Diamond. *Phys. Rev. Lett.*, 85(16):3472–75, 2000.

[172] P. W. Atkins. *Physical Chemistry*. Freeman, 1998.

[173] R. H. Kingston. Water-Vapor-Induced n-type Surface Conductivity on p-type Germanium. *Phys. Rev.*, 98(6):1766–75, 1955.

[174] N. Barsan and U. Weimar. Understanding the fundamental principles of metal oxide based gas sensors; the example of CO sensing with SnO_2 sensors in the presence of humidity. *J. Phys. Condens. Matter*, 15:R813–39, 2003.

[175] B. Yoo and A. Dodabalapura. Germanium nanowire transistors with ethylene glycol treated contacts. *J. Appl. Phys.*, 90:072106, 2007.

[176] C. Wysocki M. Lasser and B. Bernstein. Effects of thick oxide on germanium surface properties. *Phys. Rev.*, 105(2):491–5, 1957.